POLITECNICO DI MILANO

School of Industrial and Information Engineering

Department of Electronics, Information and Bioengineering (DEIB)

Master of Science in Electronics Engineering

Design and Development of a Filterless Spectrofluorometer

Supervisor: Prof. Marco Carminati

Co-Supervisors: Ing. Luca Buonanno

Ing. Davide Di Vita

Master Thesis by:

Chiara Putelli

Matr. 899086

Academic Year 2019 - 2020

Contents

List of Figures

List of Tables

Sommario

La recente crescita delle tecniche di fluorescenza come strumenti di ricerca in biochimica e biofisica ha portato allo sviluppo di sistemi sempre più precisi e sofisticati, così che la fluorescenza sia ora ampiamente utilizzata in vari campi come nel monitoraggio ambientale, in chimica clinica, nel sequenziamento del DNA e anche in saggi immunologici collegati agli enzimi. In particolare, la spettroscopia di fluorescenza è una tecnica spettroscopica con la capacità di caratterizzare completamente quantità molto piccole di campione con un semplice strumento chiamato spettrofluorimetro, generalmente composto da una sorgente di luce, una camera contenente il campione, un fotorilevatore e filtri ottici o monocromatici. Tuttavia, la continua richiesta di strumenti sensibili e performanti, ha dato vita a sistemi complessi e raffinati non sempre utilizzabili in loco; di conseguenza, nuove tecnologie chiamate LoC (Lab on Chip) stanno acquisendo sempre più importanza grazie al loro basso costo e portabilità.

In questa tesi si presenta un primo prototipo di spettrofluorimetro senza filtri, il cui scopo è quello di coniugare l'esigenza di uno strumento ad alta sensibilità con la possibilità di essere portatile, economico ma efficace. L'innovazione sta nella scelta di un fotorilevatore di nuova generazione ad alte prestazioni ed efficienza, il Silicon Photomultiplier (SiPM), e nell' assenza di filtri ottici, i cui effetti di schermatura saranno sostituiti da un circuito di modulazione della tensione di polarizzazione del fotorilevatore.

La progettazione si è concentrata sullo sviluppo hardware del circuito di modulazione della tensione di polarizzazione del SiPM e sulla sincronizzazione dei segnali che ne regolano il funzionamento utilizzando un microcontrollore e delle linee di ritardo programmabili, grazie alle quali è

stato possibile ritardare un segnale rispetto ad un altro anche di un solo nanosecondo.

Sfruttando la funzione d'uscita PWM del ritardo programmabile , è stato anche implementato un circuito LED con impulsi di durata di 10 ns sincronizzato con il modulatore SiPM, in modo che il fronte di discesa dell'impulso fosse posizionato esattamente a 20 ns dal fronte di salita del segnale di accensione del SiPM.

Infine, una parte del lavoro è stata dedicata alla progettazione di un primo prototipo di canale microfluidico utilizzato per misurazioni statiche.

Abstract

The recent growth of fluorescence techniques as research tools in biochemistry and biophysics led to the development of more precise and sophisticated systems, so that fluorescence is now widely used in various fields like environmental monitoring, clinical chemistry, DNA sequencing, and also in enzymelinked immunoassays. In particular, fluorescence spectroscopy is a spectroscopic technique with the ability to fully characterize very small amounts of sample with a simple instrument named spectrofluorometer, generally composed by a light source, a sample chamber, a photodetector and optical filters or monochromators. However, the continuous demand for sensitive and performing tools has given rise to complex and refined systems that cannot always be used on site; as a result, new technologies called LoC (Lab on Chip) are becoming increasingly important due to their low cost and portability.

In this thesis we present a first prototype of a filterless spectrofluorometer, whose purpose is to bring together the need for a high sensitivity instrument with the possibility of being portable, inexpensive but effective. The innovation lies in the choice of a new generation photodetector with high performance and efficiency, the Silicon Photomultiplier (SiPM), and in the absence of optical filters, whose shielding effects will be replaced by a modulation circuit of the photodetector voltage bias.

The design focused on the hardware development of the SiPM bias voltage modulation circuit and on the synchronization of the signals that regulate its operation using a microcontroller and programmable delay lines, thanks to which it was possible to delay one signal with respect to another even only by 1 ns.

Taking advantage of the PWM output function of the programmable delay, a LED pulsing circuit with 10 ns pulses synchronized with the SiPM modulator was also implemented, so that the falling edge of the pulse was positioned exactly at 20 ns from the rising edge of the SiPM turn on signal.

Finally, part of the work was dedicated to the design of a first prototype of a microfluidic channel used for static measurements.

Chapter 1

The LINUS project

This chapter contains a brief introduction to fluorescence techniques and describes their main features. Then the LINUS project with its specifications and objectives is presented. In the final part, the basic principles of fluorescence are summarized.

1.1 Introduction to fluorescence techniques

The number of fluorescence techniques applications has been continuously growing over the last 20 years. While initially projected as an analytical tool for the determination of the presence of specific molecules in solutions, fluorescence is now normally used in biochemistry and biophysics for studying molecular interactions and dynamics; in clinical immunoassays for the determination of the presence of specific antibodies and antigens; in drug discovery; in life sciences for DNA sequencing; in nanotechnology and material sciences for identification and characterization of new materials.

The reasons of the continuing increase in popularity are multiple: on one hand, it is due to the improvements in the sensitivity of the instrumentation that allows now for the observation of single molecules events on a routine basis; on the other hand, the interface of the instrumentation with the personal computer has increased the automation of the data

collection and the sophistication of the data analysis. A third reason for its increased success is due to the introduction in the past thirty years of innumerable and specific chemical probes used as markers for compounds that either do not display fluorescence or only emit a low level of it.

Today, the capabilities of embedded instrumentation coupled with the miniaturization of the computing capabilities brings new challenges to the field, as knowledge and possibilities for further discovery increase with each experiment [1].

Fluorescence spectroscopy is one of the most widely used molecular spectroscopic techniques in the fields of molecular biology, biophysics, and biochemistry. It has been established as an analytical technique for both qualitative and quantitative analysis because of its inherent sensitivity, selectivity, and versatility [2].

The specificity of fluorescence measurements, which make it so appealing in many contexts, can be attributed to the many properties of the assessment that can be changed from case to case. The experiments involve at least two parameters: the excitation wavelength and the emission wavelength. In a conventional fluorescence measurement, the excitation wavelength is set and the emission wavelengths are scanned to infer properties of the emitter. Various analytical methods that employ conventional fluorescence measurements exist for the detection and quantification of single-component analytes.

Fluorescence spectroscopy measures the photoluminescence of a sample, specifically the light it emits when excited by photons. The absorption of radiation by the molecule causes an electron to jump from the ground state to a higher electronic state: as soon as it decays back to its ground state, it releases a photon of a particular energy.

The intensity of light as a function of excitation wavelength (excitation spectrum) or as a function of emission wavelength (emission spectrum) provides information on the nature and concentration of the sample [3].

The great advantage of fluorescence spectroscopy over other spectroscopic techniques, like absorption spectroscopy, is that fluorescence is a background-free technique, therefore very small concentrations of analyte

can be detected. It is also more selective and different analytes can be distinguished by varying the excitation and emission wavelengths [4].

Quantification of fluorescence intensity can be made with a simple filter fluorometer or with a spectrofluorometer: the first one uses filters to isolate the incident light and fluorescent light, while the second one uses a diffraction grating monochromators to isolate the incident light and fluorescent light. Both types have the following scheme:

- light source
- primary filter or monochromator
- sample chamber
- secondary filter or monochromator
- fluorescence detection system

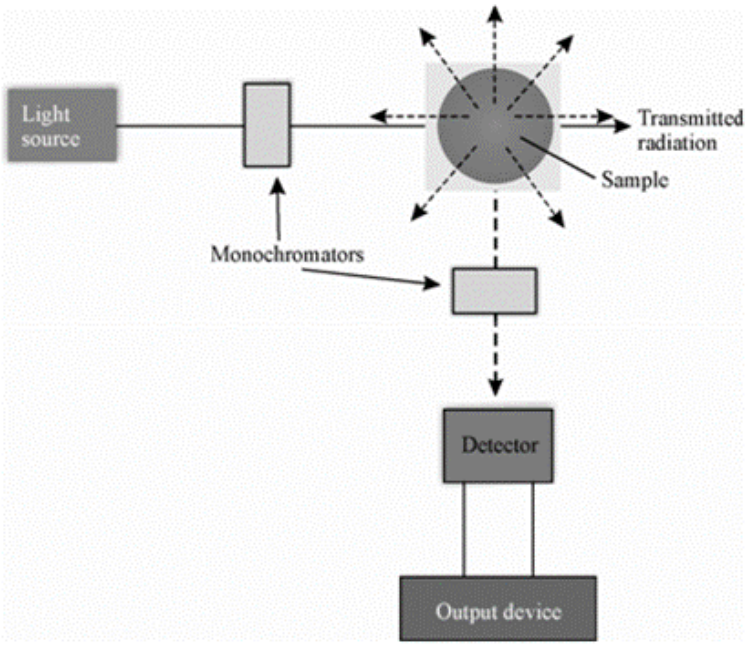

Figure 1.1: *Schematic layout of a fluorometer [5].*

Various light sources may be used as excitation sources, including lasers, LED, and lamps such as xenon arcs and mercury-vapor lamps. A

laser only emits light of high irradiance at a very narrow wavelength interval, typically under 0.01 nm, which makes an excitation monochromator or filter unnecessary. The disadvantage of this method is that the wavelength of a laser cannot be changed by much. A mercury vapor lamp is a line lamp, meaning it emits light near peak wavelengths. By contrast, a xenon arc has a continuous emission spectrum with nearly constant intensity in the range from 300-800nm and a sufficient irradiance for measurements down to just above 200nm.

The detector is placed on an axis at 90° from that of the incident beam. This right-angle geometry permits the incident radiation to pass through the test solution without contaminating the output signal received by the fluorescence detector. However, the detector unavoidably receives some of the incident radiation as a result of the inherent scattering properties of the solutions themselves, or if dust or other solids are present. Filters are used to eliminate this residual scatter. Therefore, while primary filter selects short wavelength radiation capable of causing excitation of the test substance, the secondary filter is normally a sharp cut-off filter that allows the longer wavelength fluorescence to be transmitted and blocks the scattered excited radiation. Most fluorometers use photomultiplier tubes (PMT) as detectors, but many types are available, each one having specific characteristics in order to comply with requirements in terms of spectral region of maximum sensitivity, gain, and electrical noise. The photocurrent signal is then conditioned and shown on a measuring device or recorded.

1.1.1 LIF

Laser Induced Fluorescence (LIF) is an optical spectroscopic technique where a sample is excited with a laser, and the fluorescence emitted by the sample is subsequently captured by a photodetector. LIF can be seen as a class of fluorescence spectroscopy where the usual lamp excitation is replaced by a laser source. Whereas lasers are now routinely used as excitation sources in photoluminescence spectrometers, Laser Induced

Fluorescence was not originally developed for a commercial instrument but as a standalone laser spectroscopy technique.

LIF is a widely used detection method in microfluidics and nanofluidics. In fact, light-emitting diode (LED)-induced fluorescence is also called LIF and widely integrated with microfluidics to obtain the same detection as laser induced fluorescence. In addition, LED exhibited extreme potential in microfluidics coupled with LIF owing to its mini-size, low price, and easily portable integration with microfluidics.

Usually, the wavelength of exciting laser of LIF setup should be settled to match the maximum adsorption wavelength of the target fluorescence molecules, so that the fluorescence molecules could be sufficiently excited to the higher energy level and then the excited fluorescence molecules go back to the ground status and emit fluorescence with shorter wavelengths.

The light sources of LIF can have very different wavelengths, ranging from ultraviolet ray, to visible ray, to infrared ray. Limited by the development of laser technique, current laser at ultraviolet range is usually built up as the pulse laser, which cannot supply the stable output as the continuous-wave (CW) exciting light source for LIF. Certainly, there are several ultraviolet continuous-wave lasers that were commercialized; they have not become the main exciting light source for LIF utilized in microfluidics/nanofluidics.

So far, the mostly utilized light sources for LIF are visible lasers from red ray to blue ray, even purple ray. Since the first red diode laser, its main irradiation wavelength is at 635 nm and was used for the detection of Cy-5-labeled anti-ovalbumin microfluidics capillary electrophoresis (CE). The gas laser, solid-state laser, dye laser, and diode laser have been utilized as exciting light source for LIF integration with microfluidics/nanofluidics for the detection of molecules, particles, as well as cells [6].

It is also possible to classify Laser Induced Fluorescence into continuous wave or time-resolved LIF. Continuous wave (CW) LIF utilises a continuous laser for excitation and is employed when only spectral information is required. In time-resolved LIF, a pulsed laser is used to excite the sample and its emission (either a single wavelength or the full

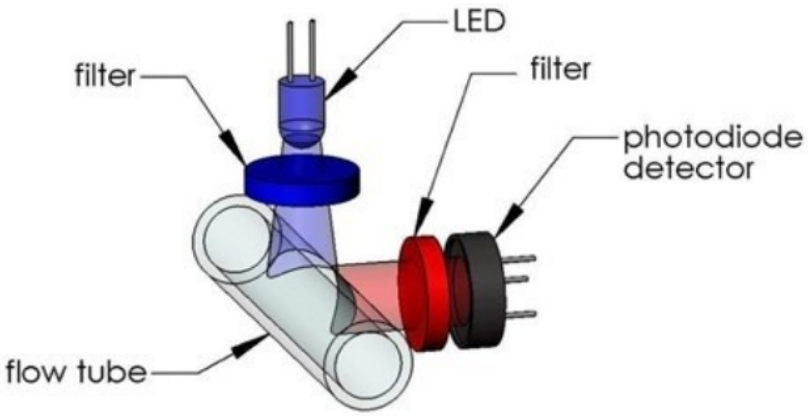

Figure 1.2: *Typical setup of a LIF experiment.*

spectrum) is detected as a function of time. This provides valuable time-resolved information such as the lifetimes of chemical intermediates and their associated time-gated spectral evolution.

LIF spectroscopy was first developed by Richard Zare in 1968 for the detection of atoms and molecules in the gas phase. Its potential as an analytical technique was quickly realised, as the fluorescence intensity is directly proportional to the concentration of the analyte in the linear power and concentration regime.

One of the first applications of LIF spectroscopy was measuring the temperature of gas-phase samples, and today it is widely used for the analysis of flames. The technique soon moved beyond gas samples and into the liquid phase, as it became a detection technique in liquid chromatography and capillary electrophoresis (CE-LIF).

Nowadays, Laser Induced Fluorescence detection can be found in many contexts, from commercial analytical instruments to advanced microscopy experiments, and it is routinely used in biological and environmental research as well as fundamental spectroscopy studies.

1.2 The LINUS Project

The L.I.N. · U.S. project (Lights Inhibition Network for Unfiltered Spectrofluorimetry) belongs to fluorescence spectroscopy techniques for the de-

tection of photons emitted from small light sources, such as fluorophores or fluorescent dyes. Aim of the project is to design a new portable, low cost and sensitive system able to detect concentration of molecules by fluorescence inspection as low as few picomolar.

Classic PMT-based spectrometers are the most employed instruments to excite fluorophore molecules and measure the emitted fluorescence. However, the growing demand for more precise systems and the technological evolution in the field of biosensors led to the emergence of better and extremely sensitive fluorescence techniques.

Measurement sensitivity in fluorometry depends on three factors [7]:

- the capability to minimize the excitation whilst allowing maximal fluorophore emitted light to arrive at the photodetector.
- the minimization of crosstalk interference of the spectral bandwidth of the excitation light with the one of the emission signal.
- photon collection maximization at the photodetector.

LIF spectroscopy assists in factors one and two to a certain extent. Nevertheless, systems will commonly incorporate appropriate optical filters to reduce the amount of excitation light overlapping the fluorescence signals at the photodetector. Unfortunately, filters add cost to the system and reduces the capability for compact design. In addition, depending on the transmission properties of the filter over the emission spectral bandwidth, signal attenuation can result in significant loss in measurement sensitivity.

If different fluorophores are used, a series of optical filters will be needed and increases instrumentation costs even further.

Accordingly, the third factor can be optimized with two expedients: the usage of a filter-less system which relays on a different excitation light discrimination method, and the introduction of a very sensitive detectors, as silicon photomultipliers (SiPM), that exhibit a high quantum efficiency, low operating voltage, high speed, high gain, simple output electronics and single photon sensitivity than the traditionally employed detectors [8] [9].

Following this line of research, Linus project combines LIF spectroscopy with SiPM detectors and a driving circuit capable of modulating the gain of the photodetector, thus avoiding the use of filters to remove the LED scattering light covering the signal.

In addition, the design of the microfluidic channel containing the fluorophore has also been taken care of in detail in order to maximize detection sensitivity, as will be explained in chapter 3.

In this thesis will be presented a first prototype of Linus used to test the actual effectiveness of the combination of the factors described so far and to identify the main problems and strengths that will be useful to improve subsequent designs.

The final goal is to achieve the creation of a lab-on-chip (LoC) spectrometer: portable, inexpensive and with a high sensitivity so that it can be used in medicine, physics and chemistry measurements [10].

1.3 Basic Concepts in Fluorescence

Fluorescence is a type of luminescence process in which sensitive molecules emit light from electronically excited states created by either a physical (absorption of light), mechanical (friction), or chemical mechanism.

When luminescence is generated through excitation of a molecule by ultraviolet or visible light photons, we talk about photoluminescence, which is formally divided into two categories, fluorescence and phosphorescence, depending upon the electronic configuration of the excited state and the emission pathway.

Fluorescence is the property of some atoms and molecules to absorb light at a particular wavelength and to subsequently emit light of longer wavelength after a brief interval, named the fluorescence lifetime.

Phosphorescence is similar to fluorescence, but it shows a much longer excited state lifetime.

Several investigators reported luminescence phenomena during the seventeenth and eighteenth centuries, but it was British scientist Sir George G. Stokes who first described fluorescence in 1852 and was responsible for

creating the term in honour of the blue-white fluorescent mineral fluorite (fluorspar). Stokes also discovered the wavelength shift to longer values in emission spectra that takes his name.

The first fluorescence microscopes were developed between 1911 and 1913 by German physicists Otto Heimstädt and Heinrich Lehmann as a spin-off from the ultraviolet instrument. These microscopes were employed to observe autofluorescence in bacteria, animal, and plant tissues.

Shortly thereafter, Stanislav Von Provazek launched a new era when he used fluorescence microscopy to study dye binding in fixed tissues and living cells. However, it was not until the early 1940s that Albert Coons developed a technique for labelling antibodies with fluorescent dyes, thus giving birth to the field of immunofluorescence. By the turn of the twenty-first century, the field of fluorescence microscopy was responsible for a revolution in cell biology, coupling the power of live cell imaging to highly specific multiple classification of individual organelles and macromolecular complexes with synthetic and genetically encoded fluorescent probes .

The fluorescence process is governed by three important events, all of which occur on timescales that are separated by several orders of magnitude (Table 1.1).

Excitation of a molecule by an incoming photon happens in femtoseconds, while vibrational relaxation of excited state electrons to the lowest energy level is much slower and can be measured in picoseconds. The final process, emission of a longer wavelength photon and return of the molecule to the ground state, occurs in the relatively long time period of nanoseconds [11].

The electronic state of a molecule determines the distribution of negative charge and the overall molecular geometry. For any particular molecule there are different electronic states (illustrated as S_0, S_1, and S_2 in Figure 1.3), depending on the total electron energy and the symmetry of various electron spin states. Each electronic state is further subdivided into a number of vibrational and rotational energy levels associated with the atomic nuclei and bonding orbitals. The ground state for most organic molecules is an electronic singlet in which all electrons are spin-paired

Table 1.1: Timescale range for fluorescence processes [11].

Transition	Process	Timescale [s]
S(0) => S(1) or S(n)	Absorption (Excitation)	10^{-15}
S(n) => S(1)	Internal Conversion	10^{-14} to 10^{-10}
S(1) => S(1)	Vibrational Relaxation	10^{-12} to 10^{-10}
S(1) => S(0)	Fluorescence	10^{-9} to 10^{-7}
S(1) => T(1)	Intersystem Crossing	10^{-10} to 10^{-8}
S(1) => S(0)	Non-Radiative Relaxation Quenching	10^{-7} to 10^{-5}
T(1) => S(0)	Phosphorescence	10^{-3} to 100
T(1) => S(0)	Non-Radiative Relaxation Quenching	10^{3} to 100

(have opposite spins).

The category of molecules capable of undergoing electronic transitions that ultimately result in fluorescence are known as fluorescent probes, fluorochromes, or simply dyes. Fluorochromes that are conjugated to a larger macromolecule (such as a nucleic acid, lipid, enzyme, or protein) through adsorption or covalent bonds are termed fluorophores. In general, fluorophores are divided into two broad classes, named intrinsic and extrinsic. Intrinsic fluorophores, such as aromatic amino acids, neurotransmitters, porphyrins, and green fluorescent protein, are those that occur naturally. Extrinsic fluorophores are synthetic dyes or modified biochemicals that are added to a sample to produce fluorescence with specific spectral properties.

1.3.1 Absorption, excitation and emission

Absorption of energy by fluorochromes happens between the closely spaced vibrational and rotational energy levels of the excited states in different molecular orbitals. The various energy levels involved in the absorption and emission of light by a fluorophore are classically presented by a Jablonski energy diagram (Figure 1.3), named in honour of the Polish physicist Professor Alexander Jablonski. A typical Jablonski diagram illustrates the singlet ground (S_0) state, as well as the first (S_1) and second (S_2) excited singlet states as a stack of horizontal lines. In Figure 1.3, the thicker lines represent electronic energy levels, while the thinner lines denote the

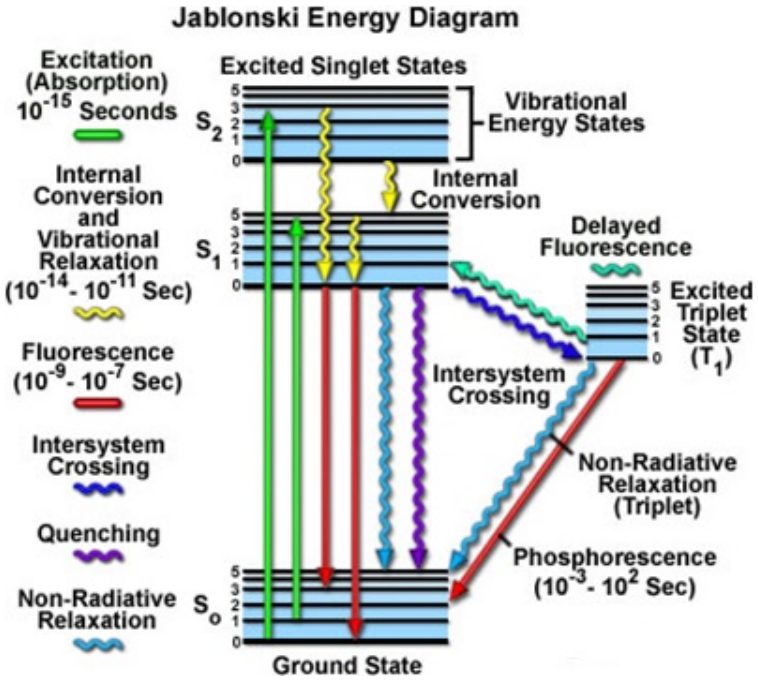

Figure 1.3: *Jablonski Energy Diagram [11].*

various vibrational energy states (rotational energy states are ignored). Transitions between the states are illustrated as straight or wavy arrows, depending upon whether the transition is associated with absorption or emission of a photon (straight arrow) or results from a molecular internal conversion or non-radiative relaxation process (wavy arrows). Vertical upward arrows are used to indicate the instantaneous nature of excitation processes, while the wavy arrows are reserved for those events that occur on a much longer timescale. Absorption of light occurs very quickly (approximately a femtosecond, the time necessary for the photon to travel a single wavelength) in discrete amounts called quanta and corresponds to excitation of the fluorophore from the ground state to an excited state. Likewise, emission of a photon through fluorescence or phosphorescence is also measured in terms of quanta. The energy in a quantum is expressed by the famous Planck's Law:

$$E = hf = h\frac{c}{\lambda} \tag{1.1}$$

where E is the energy, h is Planck's constant, f and λ are the frequency and wavelength of the incoming photon, and c is the speed of light. Planck's Law declares that the radiation energy of an absorbed photon is directly proportional to the frequency and inversely proportional to the wavelength, meaning that shorter incident wavelengths possess a greater quantum of energy. The absorption of a photon of energy by a fluorophore is a phenomenon that can only occur with incident light of specific wavelengths known as absorption bands. If the absorbed photon contains more energy than is necessary for a simple electronic transition, the excess energy is usually converted into vibrational and rotational energy. However, if a collision occurs between a molecule and a photon having insufficient energy to promote a transition, no absorption occurs. In general, fluorescence investigations are conducted with radiation having wavelengths ranging from the ultraviolet to the visible regions of the electromagnetic spectrum (250 to 700 nm). With ultraviolet or visible light, common fluorophores are usually excited to higher vibrational levels of the first (S_1) or second (S_2) singlet energy state [11].

One of the absorption (or excitation) transitions presented in Figure 1.3 (left-hand green arrow) occurs from the lowest vibrational energy level of the ground state to a higher vibrational level in the second excited state (a transition denoted as $S_0 = 0$ to $S_2 = 3$). A second excitation transition is depicted from the second vibrational level of the ground state to the highest vibrational level in the first excited state (denoted as $S_0 = 1$ to $S_1 = 5$). In a typical fluorophore, irradiation with a wide spectrum of wavelengths will generate an entire range of allowed transitions that populate the various vibrational energy levels of the excited states. Some of these transitions will have a much higher degree of probability than others, and when combined, will constitute the absorption spectrum of the molecule. For most fluorophores, the absorption and excitation spectra are distinct, but often overlap and can sometimes become indistinguishable. In other cases (fluorescein, for example) the absorption and excitation spectra are clearly separated.

Directly following absorption of a photon, numerous processes will oc-

cur with varying probabilities, but the most likely will be relaxation to the lowest vibrational energy level of the first excited state ($S_1 = 0$; Figure 1.3). This process is known as internal conversion or vibrational relaxation (loss of energy in the absence of light emission) and generally occurs in a picosecond or less. The excess vibrational energy is converted into heat, which is absorbed by nearby solvent molecules upon colliding with the excited state fluorophore. An excited molecule exists in the lowest excited singlet state (S_1) for periods on the order of nanoseconds before finally relaxing to the ground state. If relaxation from this long-lived state is accompanied by emission of a photon, the process is formally known as fluorescence. The closely spaced vibrational energy levels of the ground state, when coupled with normal thermal motion, produce a wide range of photon energies during emission. As a result, fluorescence is normally observed as emission intensity over a band of wavelengths rather than a sharp line. Most fluorophores can repeat the excitation and emission cycle many hundreds to thousands of times before the highly reactive excited state molecule is photobleached, resulting in the destruction of fluorescence. For example, the well-studied probe fluorescein isothiocyanate (FITC) can undergo excitation and relaxation for approximately 30,000 cycles before the molecule no longer responds to incident illumination.

Several other relaxation pathways that have varying degrees of probability compete with the fluorescence emission process. The excited state energy can be dissipated non-radiatively as heat (illustrated by the cyan wavy arrow in Figure 1.3), the excited fluorophore can collide with another molecule to transfer energy in a second type of non-radiative process (for example, quenching, as indicated by the purple wavy arrow in Figure 1.3), or a phenomenon known as intersystem crossing to the lowest excited triplet state can occur (the blue wavy arrow in Figure 1.3). The latter event is relatively rare, but ultimately results either in emission of a photon through phosphorescence or a transition back to the excited singlet state that yields delayed fluorescence. Transitions from the triplet excited state to the singlet ground state are forbidden, which results in rate constants for triplet emission that are several orders of magnitude lower than

those for fluorescence.

Both of the triplet state transitions are diagrammed on the right-hand side of the Jablonski energy profile illustrated in Figure 1.3. The low probability of intersystem crossing arises from the fact that molecules must first undergo spin conversion to produce unpaired electrons, an unfavourable process. The primary importance of the triplet state is the high degree of chemical reactivity exhibited by molecules in this state, which often results in photobleaching and the production of damaging free radicals.

The probability of a transition occurring from the ground state (S_0) to the excited singlet state (S_1) depends on the degree of similarity between the vibrational and rotational energy states when an electron resides in the ground state versus those present in the excited state, as outlined in Figure 1.4.

The Franck-Condon energy diagram illustrated in Figure 1.4 presents the vibrational energy probability distribution among the various levels in the ground (S_0) and first excited (S_1) states for a hypothetical molecule. Excitation transitions (red lines) from the ground to the excited state occur in such a short timeframe (femtoseconds) that the internuclear distance associated with the bonding orbitals does not have sufficient time to change, and thus the transitions are represented as vertical lines.

This concept is referred to as the Franck-Condon Principle. The wavelength of maximum absorption (red line in the centre) represents the most probable internuclear separation in the ground state to an allowed vibrational level in the excited state. At room temperature, thermal energy is not adequate to significantly populate excited energy states and the most likely state for an electron is the ground state (S_0), which contains a number of distinct vibrational energy states, each with differing energy levels. The most preferred transitions will be the ones where the rotational and vibrational electron density probabilities maximally overlap in both the ground and excited states (see Figure 1.4) [11].

However, incident photons of varying wavelength (and quanta) may have sufficient energy to be absorbed and often produce transitions from other internuclear separation distances and vibrational energy levels. This

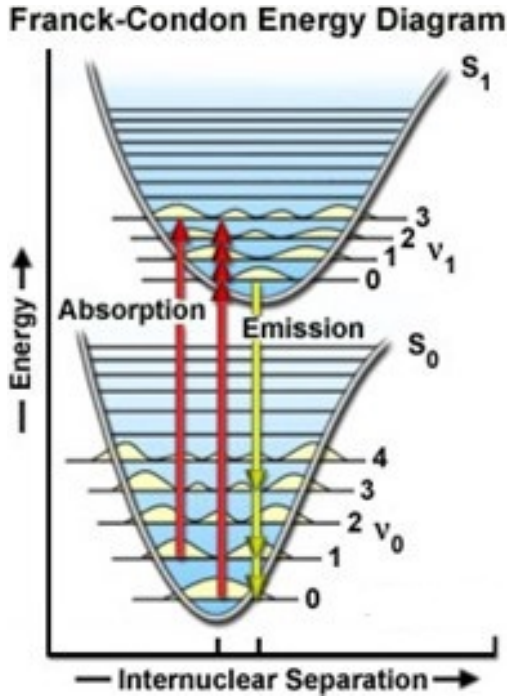

Figure 1.4: *Frank-Condon Energy Diagram [11].*

effect gives rise to an absorption spectrum containing multiple peaks (Figure 1.5). The wide range of photon energies associated with absorption transitions in fluorophores causes the resulting spectra to appear as broad bands rather than discrete lines. The hypothetical absorption spectrum illustrated in Figure 1.5 (blue band) results from several preferential electronic transitions from the ground state to the lowest excited energy state (labelled S_0 and S_1, respectively). Superimposed over the absorption spectrum are vertical lines (yellow) representing the transitions from the lowest vibrational level in the ground state to higher vibrational energy levels in the excited state. Note that transitions to the highest excited vibrational levels are those occurring at higher photon energies (lower wavelength or higher wavenumber). The approximate energies associated with the transitions are denoted in electron-volts (eV) along the upper abscissa of Figure 1.5. Vibrational levels associated with the ground and excited states are also included along the right-hand ordinate.

Scanning through the absorption spectrum of a fluorophore while record-

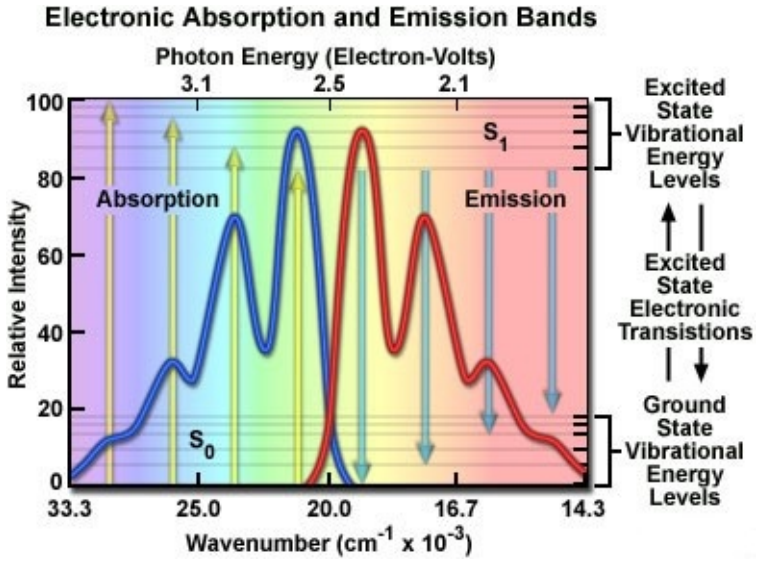

Figure 1.5: *Energy absorption and emission band [11].*

ing the emission intensity at a single wavelength (usually the wavelength of maximum emission intensity) will generate the excitation spectrum. Likewise, exciting the fluorophore at a single wavelength (again, preferably the wavelength of maximum absorption) while scanning through the emission wavelengths will reveal the emission spectral profile. The excitation and emission spectra may be considered as probability distribution functions that a photon of given quantum energy will be absorbed and ultimately enable the fluorophore to emit a second photon in the form of fluorescence radiation [11].

1.3.2 Stokes Shift and the Mirror Image Rule

If the fluorescence emission spectrum of a fluorophore is carefully examined, several important features become immediately evident: the emission spectrum is independent of the excitation energy (wavelength) as a consequence of rapid internal conversion from higher initial excited states to the lowest vibrational energy level of the S_1 excited state. For many of the common fluorophores, the vibrational energy level spacing is similar for the ground and excited states, which results in a fluorescence spectrum

that strongly resembles the mirror image of the absorption spectrum. This is due to the fact that the same transitions are most advantageous for both absorption and emission. Finally, in solution (where fluorophores are generally studied) the detailed vibrational structure is generally lost and the emission spectrum appears as a broad band. Because emission of a photon often leaves the fluorophore in a higher vibrational ground state, the emission spectrum is typically a mirror image of the absorption spectrum resulting from the ground to first excited state transition. In effect, the probability of an electron returning to a particular vibrational energy level in the ground state is similar to the probability of that electron's position in the ground state before excitation. This concept, known as the Mirror Image Rule, is illustrated in Figure 1.5 for the emission transitions (blue lines) from the lowest vibrational energy level of the excited state back to various vibrational levels in ground state. The resulting emission spectrum (red band) is a mirror image of the absorption spectrum displayed by the hypothetical chromophore.

In many cases, excitation by high energy photons leads to the population of higher electronic and vibrational levels (S_2, S_3, etc.), which quickly lose excess energy as the fluorophore relaxes to the lowest vibrational level of the first excited state (see Figure 1.3). Because of this rapid relaxation process, emission spectra are generally independent of the excitation wavelength (some fluorophores emit from higher energy states, but such activity is rare). For this reason, emission is the mirror image of the ground state to lowest excited state transitions, but not of the entire absorption spectrum, which may include transitions to higher energy levels. Presented in Figure 1.6 are the absorption and emission spectra for quinine, the naturally occurring antimalarial agent (and first known fluorophore) whose fluorescent properties were originally described by Sir John Fredrick William Hershel in 1845. Quinine does not follow the mirror image rule as is evident by inspecting the single peak in the emission spectrum (at 460 nm), which does not mirror the two peaks at 310 and 350 nm featured in the bi-modal absorption spectrum. The shorter wavelength ultraviolet absorption peak (310 nm) is due to an excitation

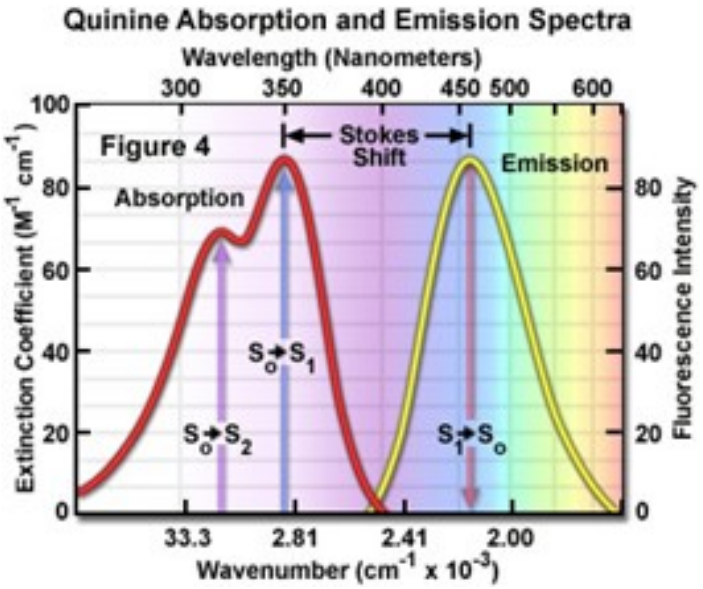

Figure 1.6: *Quinine absorption and emission spectra [11].*

transition to the second excited state (from S_0 to S_2) that quickly relaxes to the lowest excited state (S_1). As a consequence, fluorescence emission occurs exclusively from the lowest excited singlet state (S_1), resulting in a spectrum that mirrors the ground to first excited state transition (350 nm peak) in quinine and not the entire absorption spectrum. Because the energy associated with fluorescence emission transitions (see Figure 1.3 and Figure 1.6) is typically less than that of absorption, the resulting emitted photons have less energy and are shifted to longer wavelengths. This phenomenon is generally known as Stokes Shift and occurs for virtually all fluorophores commonly employed in solution investigations. The primary origin of the Stokes shift is the rapid decay of excited electrons to the lowest vibrational energy level of the S_1 excited state. In addition, fluorescence emission is usually accompanied by transitions to higher vibrational energy levels of the ground state, resulting in further loss of excitation energy to thermal equilibrium of the excess vibrational energy. Other events, such as solvent orientation effects, excited-state reactions, complex formation, and resonance energy transfer can also contribute to longer emission wavelengths. In practice, the Stokes shift is measured as

the difference between the maximum wavelengths in the excitation and emission spectra of a particular fluorochrome or fluorophore. The size of the shift varies with molecular structure but can range from just a few nm to over several hundred nm. For example, the Stokes shift for fluorescein is approximately 20 nm, while the shift for quinine is 110 nm (see Figure 1.6) and that for the porphyrins is over 200 nm. The existence of Stokes shift is critical to the extremely high sensitivity of fluorescence imaging measurements. The red emission shift enables the use of precision bandwidth optical filters to effectively block excitation light from reaching the detector so the relatively faint fluorescence signal (having a low number of emitted photons) can be observed against a low-noise background [11].

1.3.3 Quenching and Photobleaching

The consequences of quenching and photobleaching are an effective reduction in the amount of emission and should be of primary consideration when designing and executing fluorescence investigations. The two phenomena are distinct: quenching is often reversible whereas photobleaching is not.

Quenching arises from a variety of competing processes that induce non-radiative relaxation (without photon emission) of excited state electrons to the ground state, which may be either intramolecular or intermolecular in nature. Because non-radiative transition pathways compete with the fluorescence relaxation, they usually dramatically lower or, in some cases, completely eliminate emission. Most quenching processes act to reduce the excited state lifetime and the quantum yield of the affected fluorophore.

A common example of quenching is observed with the collision of an excited state fluorophore and another (non-fluorescent) molecule in solution, resulting in deactivation of the fluorophore and return to the ground state. In most cases, neither of the molecules is chemically altered in the collision quenching process. A wide variety of simple elements and compounds behave as collision quenching agents, including oxygen, halogens,

amines, and many electron-deficient organic molecules. Collision quenching can reveal the presence of localized quencher molecules or moieties, which via diffusion or conformational change, may collide with the fluorophore during the excited state lifetime. The mechanisms for collision quenching include electron transfer, spin-orbit coupling, and intersystem crossing to the excited triplet state.

A second type of quenching mechanism, called static or complex quenching, arises from non-fluorescent complexes formed between the quencher and fluorophore that serve to limit absorption by reducing the population of active, excitable molecules. This effect occurs when the fluorescent species forms a reversible complex with the quencher molecule in the ground state and does not rely on diffusion or molecular collisions. In static quenching, fluorescence emission is reduced without altering the excited state lifetime. A fluorophore in the excited state can also be quenched by a dipolar resonance energy transfer mechanism when in close proximity with an acceptor molecule to which the excited state energy can be transferred non-radiatively. In some cases, quenching can occur through non-molecular mechanisms, such as attenuation of incident light by an absorbing species (including the chromophore itself).

In contrast to quenching, photobleaching (also termed fading) occurs when a fluorophore permanently loses the ability to emit fluorescence due to photon-induced chemical damage and covalent modification. Upon transition from an excited singlet state to the excited triplet state, fluorophores may interact with another molecule to produce irreversible covalent modifications. The triplet state is relatively long-lived with respect to the singlet state, thus allowing excited molecules a much longer timeframe to undergo chemical reactions with components in the environment. The average number of excitation and emission cycles that occur for a particular fluorophore before photobleaching is dependent upon the molecular structure and the local environment. Some fluorophores fade quickly after emitting only a few photons, while others that are more robust can undergo thousands or millions of cycles before bleaching (example in Figure 1.7). An important class of photobleaching events are photodynamic,

meaning they involve the interaction of the fluorophore with a combination of light and oxygen. Reactions between fluorophores and molecular oxygen permanently destroy fluorescence and yield a free radical singlet oxygen species that can chemically modify other molecules in living cells. The amount of photobleaching due to photodynamic events is a function of the molecular oxygen concentration and the proximal distance between the fluorophore, oxygen molecules, and other cellular components. Photobleaching can be reduced by limiting the exposure time of fluorophores to illumination or by lowering the excitation energy. However, these techniques also reduce the measurable fluorescence signal. In many cases, solutions of fluorophores or cell suspensions can be deoxygenated, but this is not feasible for living cells and tissues. Perhaps the best protection against photobleaching is to limit exposure of the fluorochrome to intense illumination (using neutral density filters) coupled with the careful use of commercially available antifade reagents that can be added to the mounting solution or cell culture medium.

Under certain circumstances, the photobleaching effect can also be utilized to obtain specific information that would not otherwise be available. For example, in fluorescence recovery after photobleaching (FRAP) experiments, fluorophores within a target region are intentionally bleached with excessive levels of irradiation. As new fluorophore molecules diffuse into the bleached region of the specimen (recovery), the fluorescence emission intensity is monitored to determine the lateral diffusion rates of the target fluorophore. In this manner, the translational mobility of fluorescently labelled molecules can be established within a very small (2 to 5 μm) region of a single cell or section of living tissue [11].

1.3.4 Solvent Effects on Fluorescence Emission

A variety of environmental factors affect fluorescence emission, including interactions between the fluorophore and surrounding solvent molecules (dictated by solvent polarity), other dissolved inorganic and organic compounds, temperature, pH, and the localized concentration of the fluo-

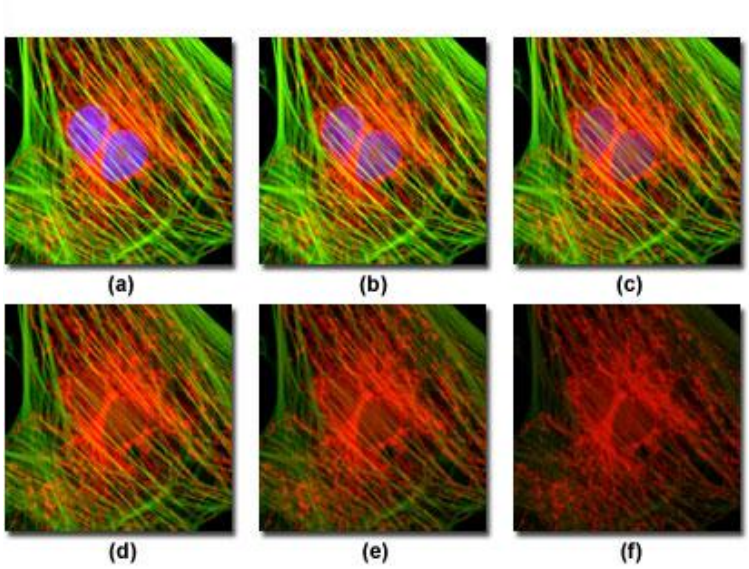

Figure 1.7: *Photobleaching observed in a series of digital images captured at different times relative to a culture of cells. The nuclei were stained with DAPI (blue fluorescence) and the actin cytoskeleton and mitochondria, respectively, were stained with MitoTracker Red (red fluorescence) and Alexa Fluor 488 (green fluorescence). The photos were taken at intervals of two minutes with a combination of fluorescence filters with bandwidths selected to excite the three fluorophores simultaneously (tri-band filters). Note that all three fluorophores have a relatively high intensity under (a), but the relative intensity in DAPI (blue) starts to drop rapidly at two minutes and is almost completely sold out in six minutes. The mitochondrial and actin stains are more resistant to photobleaching, but the intensity of both diminishes greatly over the timeline (10 minutes) [11].*

rescent species. The effects of these parameters vary widely from one fluorophore to another, but the absorption and emission spectra, as well as quantum yields, can be heavily influenced by environmental variables. In fact, the high degree of sensitivity in fluorescence is primarily due to interactions that occur in the local environment during the excited state lifetime. A fluorophore can be considered an entirely different molecule in the excited state (than in the ground state), and thus will display an alternate set of properties in regard to interactions with the environment in the excited state relative to the ground state.

In solution, solvent molecules surrounding the ground state fluorophore

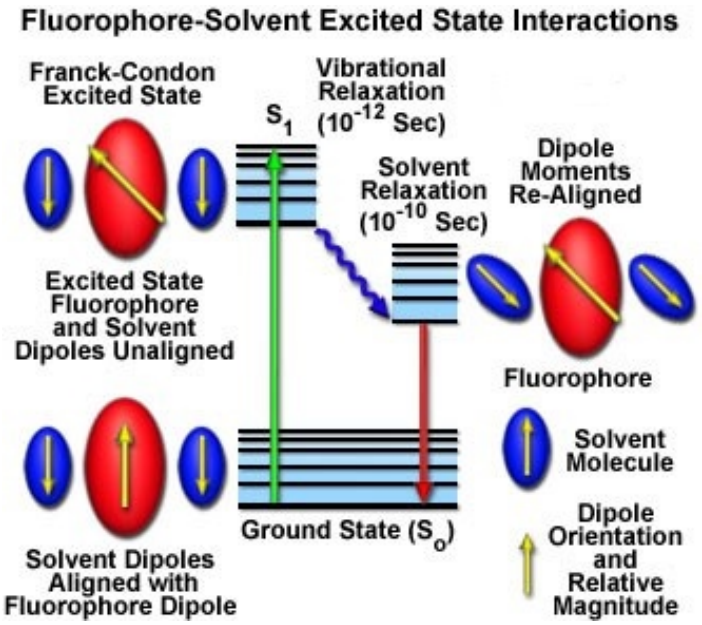

Figure 1.8: *Fluorophore solvent [11].*

also have dipole moments that can interact with the dipole moment of the fluorophore to yield an ordered distribution of solvent molecules around the fluorophore. Energy level differences between the ground and excited states in the fluorophore produce a change in the molecular dipole moment, which ultimately induces a rearrangement of surrounding solvent molecules. However, the Franck-Condon principle decrees that, upon excitation of a fluorophore, the molecule is excited to a higher electronic energy level in a far shorter timeframe than it takes for the fluorophore and solvent molecules to re-orient themselves within the solvent-solute interactive environment. As a result, there is a time delay between the excitation event and the re-ordering of solvent molecules around the solvated fluorophore (as illustrated in Figure 1.8), which generally has a much larger dipole moment in the excited state than in the ground state. After the fluorophore has been excited to higher vibrational levels of the first excited singlet state (S_1)), excess vibrational energy is rapidly lost to surrounding solvent molecules as the fluorophore slowly relaxes to the lowest vibrational energy level (occurring in the picosecond time scale). Solvent

molecules assist in stabilizing and further lowering the energy level of the excited state by re-orienting (termed solvent relaxation) around the excited fluorophore in a slower process that requires between 10 and 100 ps. This has the effect of reducing the energy separation between the ground and excited states, which results in a red shift (to longer wavelengths) of the fluorescence emission. Increasing the solvent polarity produces a correspondingly larger reduction in the energy level of the excited state, while decreasing the solvent polarity reduces the solvent effect on the excited state energy level. The polarity of the fluorophore also determines the sensitivity of the excited state to solvent effects. Polar and charged fluorophores exhibit a far stronger effect than non-polar fluorophores.

Solvent relaxation effects on fluorescence can result in a dramatic effect on the size of Stokes shifts. For example, the heterocyclic indole moiety of the amino acid tryptophan normally resides on the hydrophobic interior of proteins where the relative polarity of the surrounding medium is low. Upon denaturation of a typical host protein with heat or a chemical agent, the environment of the tryptophan residue is changed from non-polar to highly polar as the indole ring emerges into the surrounding aqueous solution. Fluorescence emission is increased in wavelength from approximately 330 to 365 nm, a 35 nanometers shift due to solvent effects. Thus, the emission spectra of both intrinsic and extrinsic fluorescent probes can be employed to probe solvent polarity effects, molecular associations, and complex formation with polar and non-polar small molecules and macromolecules.

Quantitative fluorescence investigations should be constantly monitored to scan for potential shifts in emission profiles, even when they are not intended nor expected. In simple systems where a homogeneous concentration can be established, a progressive emission intensity increase should be observed as a function of increasing fluorophore concentration, and vice versa. However, in complex biological systems, fluorescent probe concentration may vary locally over a wide range, and intensity fluctuations or spectral shifts are often the result of changes in pH, calcium ion concentration, energy transfer, or the presence of a quenching agent rather

than fluorophore stoichiometry. The possibility of unexpected solvent or other environmental effects should always be considered in evaluating the results of experimental procedures [11].

1.3.5 Resonance Energy Transfer

A fluorophore in the excited state can, as discussed above, lose excitation energy by converting it into light (fluorescence), through thermal equilibrium (vibrational relaxation), or by transfer to another molecule through collision or complex formation (non-radiative dissipation and quenching).

In forming a complex or colliding with a solvent molecule, energy is transferred by the coupling of electronic orbitals between the fluorophore and a second molecule. There is also yet another process, termed resonance energy transfer (RET or FRET), by which a fluorophore in the excited state (termed the donor) may transfer its excitation energy to a neighbouring chromophore (the acceptor) non-radiatively through long range dipole-dipole interactions over distances measured in nanometers. The basic theory of resonance energy transfer assumes the donor fluo-

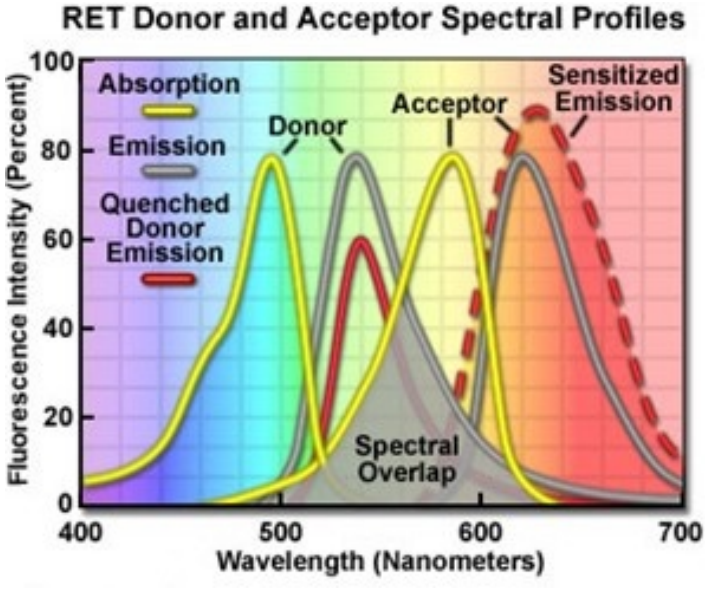

Figure 1.9: *FRET [11].*

rophore can be treated as an oscillating dipole that can transfer energy

to a similar dipole at a particular resonance frequency in a manner analogous to the behaviour of coupled oscillators, such as a pair of tuning forks vibrating at the same frequency. Resonance energy transfer is potentially possible whenever the emission spectrum of the donor fluorophore overlaps the absorption spectrum of the acceptor, which by itself is not necessarily fluorescent. An important concept in understanding this mechanism of energy transfer is that the process does not involve emission of light from the donor followed by subsequent absorption of the emitted photons by the acceptor. In other words, there is no intermediate photon involved in the mechanism of resonance energy transfer. The transfer of energy is manifested by both quenching of the donor fluorescence emission in the presence of the acceptor and increased (sensitized) emission of acceptor fluorescence.

Presented in Figure 1.9 are changes to the emission intensities of the spectral profiles from a coupled donor and acceptor molecule undergoing resonance energy transfer. Overlap (gray area) between the donor emission (central gray curve) and acceptor absorption spectra (central yellow curve) is required for the process to occur. When this overlap is present, and the donor and acceptor are separated by less than 10 nm, donor excitation energy can be transferred non-radiatively to the acceptor. The net result is quenching of the donor fluorescence emission (red curve) and an increase in the emission intensity of the acceptor (sensitized emission, red dashed curve).

The efficiency of resonance energy transfer varies with the degree of spectral overlap, but most importantly as the inverse of the sixth power of the distance (radius, r) separating the donor and acceptor chromophores. Energy transfer to the acceptor requires the distance between the chromophores to be relatively close, within the limiting boundaries of 1 to 10 nm. The phenomenon can be detected by exciting a labelled specimen with illumination wavelengths corresponding to the absorption (excitation) maximum of the donor and detecting fluorescence emission in the peak emission wavelength region of the acceptor. Alternatively, the fluorescence lifetime of the donor can be measured in the presence and absence

of the acceptor. The dependence of energy transfer efficiency on the separation distance between the donor and acceptor provides the basis for the utility of resonance energy transfer in the study of cell biology. This aspect of resonance energy transfer enables the technique to be used as a spectroscopic ruler to study and quantify interactions between cellular components, as well as conformational changes within individual macromolecules, at the molecular level [11].

Chapter 2

Fluorophores and SiPMs

This chapter presents a complete description of the most used fluorophores with their main characteristics. Then there is a section focused on Pyrene, the sample fluorophore chosen for this project. Finally, the basic working principle of Silicon Photomultiplier(SiPM) photodetectors is submitted.

2.1 Types of fluorophores and main features

Fluorescence probes represent the most important area of fluorescence spectroscopy. The wavelength and time resolution required of the instruments is determined by the spectral properties of the fluorophores. They can be generally divided into two main classes: intrinsic and extrinsic. Intrinsic fluorophores are those that occur naturally. These include the aromatic amino acids, NADH (Nicotinamide adenine dinucleotide in reduced form), flavins, derivatives of pyridoxyl, and chlorophyll. Extrinsic fluorophores are added to the sample to provide fluorescence when none exists, or to change the spectral properties of the sample. Examples are dansyl, fluorescein, rhodamine, and numerous other substances.

A diversity of molecules displays fluorescence and numerous interactions and processes can alter the spectral properties. Fluorophores can be covalently attached to macromolecules or designed to interact with specific ions. Emission can occur from the UV to the NIR, and probes

are available with short (ns) and long (μs to ms) lifetimes. The technology of probe chemistry is rapidly changing, and new probes are allowing previously impossible experiments to be performed [3].

2.1.1 Extinction Coefficient, Quantum Yield, and Fluorescence Lifetime

Three fundamental parameters commonly used in describing and comparing fluorophores are the extinction coefficient (e), quantum yield (F), and fluorescence lifetime (t). Molar extinction coefficients are widely employed in the fields of spectroscopy, microscopy, and fluorescence in order to convert units of absorbance into units of molar concentration for a variety of chemical substances. The extinction coefficient is determined by measuring the absorbance at a reference wavelength (characteristic of the absorbing molecule) for a one molar (M) concentration (one mole per liter) of the target chemical in a cuvette having a one-centimeter path length. The reference wavelength is usually the wavelength of maximum absorption in the ultraviolet or visible light spectrum. Extinction coefficients are a direct measure of the ability of a fluorophore to absorb light, and those chromophores having a high extinction coefficient also have a high probability of fluorescence emission. Also, because the intrinsic lifetime (discussed below) of a fluorophore is inversely proportional to the extinction coefficient, molecules exhibiting a high extinction coefficient have an excited state with a short intrinsic lifetime [11].

Quantum yield is an indicator for measuring the efficiency of fluorescence emission relative to all of the possible pathways for relaxation and is generally expressed as the (dimensionless) ratio of photons emitted to the number of photons absorbed. In other words, the quantum yield represents the probability that a given excited fluorochrome will produce an emitted photon (fluorescence). Quantum yields typically range between a value of zero and one, and fluorescent molecules commonly employed as probes in microscopy have quantum yields ranging from very low (0.05 or less) to almost unity (the brightest fluorophores). In general, a high

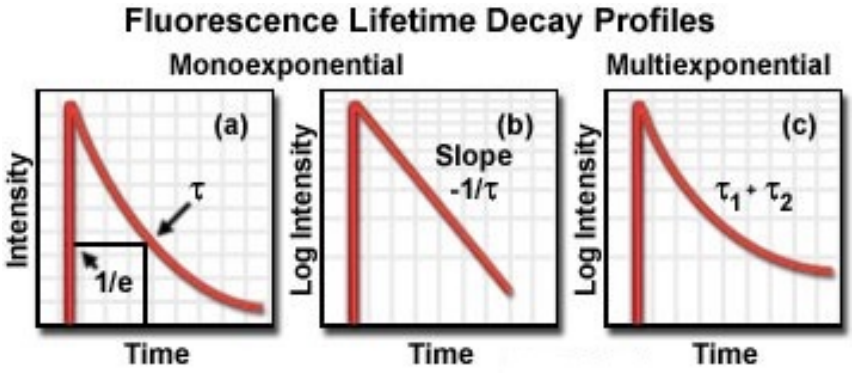

Figure 2.1: *Typical exponential fluorescence decay [11].*

quantum yield is desirable in most imaging applications. The quantum yield of a given fluorophore varies, sometimes to large extremes, with environmental factors such as pH, concentration, and solvent polarity. The fluorescence lifetime is the characteristic time that a molecule remains in an excited state prior to returning to the ground state and is an indicator of the time available for information to be gathered from the emission profile. During the excited state lifetime, a fluorophore can undergo conformational changes as well as interact with other molecules and diffuse through the local environment. The decay of fluorescence intensity as a function of time in a uniform population of molecules excited with a brief pulse of light is described by an exponential function:

$$I(t) = I_0 e^{(-\frac{t}{\tau})} \tag{2.1}$$

where I(t) is the fluorescence intensity measured at time t, I_0 is the initial intensity observed immediately after excitation, and τ is the fluorescence lifetime. Formally, the fluorescence lifetime is defined as the time in which the initial fluorescence intensity of a fluorophore decays to 1/e (approximately 37 percent) of the initial intensity. This quantity is the reciprocal of the rate constant for fluorescence decay from the excited state to the ground state. Because the level of fluorescence is directly proportional to the number of molecules in the excited singlet state, lifetime measurements

can be conducted by measuring fluorescence decay after a brief pulse of excitation. In a uniform solvent, fluorescence decay is usually a monoexponentially function. More complex systems, such as viable tissues and living cells, contain a mixed set of environments that often yield multiexponential values (Figure 2.1) when fluorescence decay is measured. In addition, several other processes can compete with fluorescence emission for return of excited state electrons to the ground state, including internal conversion, phosphorescence (intersystem crossing), and quenching. Aside from fluorescence and phosphorescence, non-radiative processes are the primary mechanism responsible for relaxation of excited state electrons.

All non-fluorescent processes that compete for deactivation of excited state electrons can be conveniently combined into a single rate constant, termed the non-radiative rate constant and denoted by the variable k_{nr}. The non-radiative rate constant usually ignores any contribution from vibrational relaxation because the rapid speeds (picoseconds) of these conversions are several orders of magnitude faster than slower deactivation (nanoseconds) transitions. Thus, the quantum yield can now be expressed in terms of rate constants:

$$F = \frac{k_f}{k_f + k_{nr}} = \frac{t_f}{t_0} \tag{2.2}$$

where k_f is the rate constant for fluorescence decay. The reciprocal of the decay rate constant equals the intrinsic lifetime (t_0), which is defined as the lifetime of the excited state in the absence of all processes that compete for excited state deactivation. In practice, the fluorescence excited state lifetime is shortened by non-radiative processes, resulting in a measured lifetime (t_f) that is a combination of the intrinsic lifetime and competing non-fluorescent relaxation mechanisms. Because the measured lifetime is always less than the intrinsic lifetime, the quantum yield never exceeds a value of unity.

Many of the common probes employed in optical microscopy have fluorescence lifetimes measured in nanoseconds, but these can vary over a wide range depending on molecular structure, the solvent, and environmental

conditions. Quantitative fluorescence lifetime measurements enable investigators to distinguish between fluorophores that have similar spectral characteristics but different lifetimes and can also yield clues to the local environment. Specifically, the pH and concentration of ions in the vicinity of the probe can be determined without knowing the localized fluorophore concentration, which is of significant benefit when used with living cells and tissues where the probe concentration may not be uniform. In addition, lifetime measurements are less sensitive to photobleaching artifacts than are intensity measurements [11].

2.1.2 Intrinsic fluorophores

Amino acids

Intrinsic protein fluorescence originates with the aromatic amino acids tryptophan (trp), tyrosine (tyr), and phenylalanine (phe). The indole groups of tryptophan residues are the dominant source of UV absorbance and emission in proteins. Tyrosine has a quantum yield similar to tryptophan (Table 3.1), but its emission spectrum is more narrowly distributed on the wavelength scale (Figure 2.2). The emission of tryptophan is highly sensitive to its local environment and is thus often used as a reporter group for protein conformational changes. Spectral shifts of protein emission have been observed as a result of several phenomena, including binding of ligands, protein–protein association, and protein unfolding. The emission maxima of proteins reflect the average exposure of their tryptophan residues to the aqueous phase. Fluorescence lifetimes of tryptophan residues range from 1 to 6 ns [3].

Table 2.1: Fluorescence parameters of aromatic amino acids in water at neutral pH [3].

Species	λ_{ex}(nm)	λ_{em}(nm)	BandWidth(nm)	Quantum Yield	Lifetime(s)
Phenylalanine	260	282	-	0.02	6.8
Tyrosine	275	304	34	0.14	3.6
Tryptophan	295	353	60	0.13	3.1

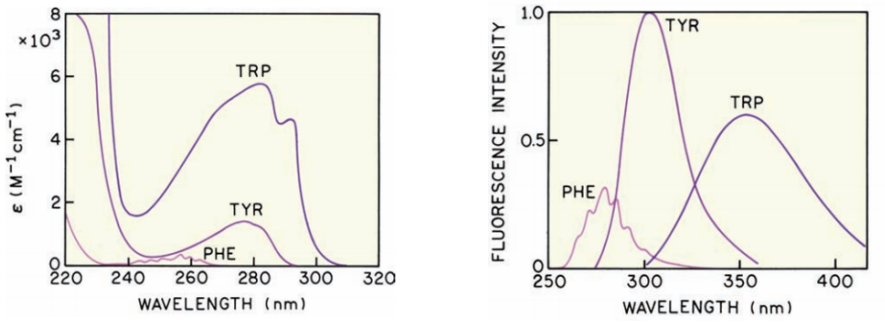

Figure 2.2: *Absorption and emission spectra of the fluorescent amino acids in water of pH 7.0 [3].*

Fluorescence Enzyme Cofactors

Enzyme cofactors are frequently fluorescent. NADH is highly fluorescent, with absorption and emission maxima at 340 and 460 nm, respectively (Figure 2.3). The lifetime of NADH in aqueous buffer is near 0.4 ns. In solution its fluorescence is partially quenched by collisions or stacking with the adenine moiety. Upon binding of NADH to proteins, the quantum yield of the NADH generally increases fourfold and the lifetime increases to about 1.2 ns. However, depending on the protein, NADH fluorescence can increase or decrease upon protein binding. The lifetimes of protein-bound NADH are typically different in the presence and absence of bound enzyme substrate. The cofactor pyridoxyl phosphate is also fluorescent. Its absorption and emission spectra are dependent on its chemical structure in the protein, where pyridoxyl groups are often coupled to lysine residues by the aldehyde groups. The emission spectrum of pyridoxamine is at shorter wavelengths than that of pyridoxyl phosphate. The emission spectrum of pyridoxamine is dependent on pH and the emission spectrum of the pyridoxyl group depends on its interaction with proteins.

Riboflavin, FMN (Flavin mononucleotide), and FAD (Flavin adenine dinucleotide) absorb light in the visible range (450 nm) and emit around 525 nm (Figure 2.3). In contrast to NADH, the oxidized forms of flavins are fluorescent, not the reduced forms. Typical lifetimes for FMN and FAD are 4.7 ns and 2.3 ns, respectively. As for NADH, the flavin fluorescence

is quenched by the adenine.

In contrast to NADH, which is highly fluorescent when bound to proteins, flavoproteins are generally weakly fluorescent or nonfluorescent, but exceptions exist. Intensity decays of protein-bound flavins are typically complex, with multi-exponential decay times ranging from 0.1 to 5 ns, and mean decay times from 0.3 to 1 ns.

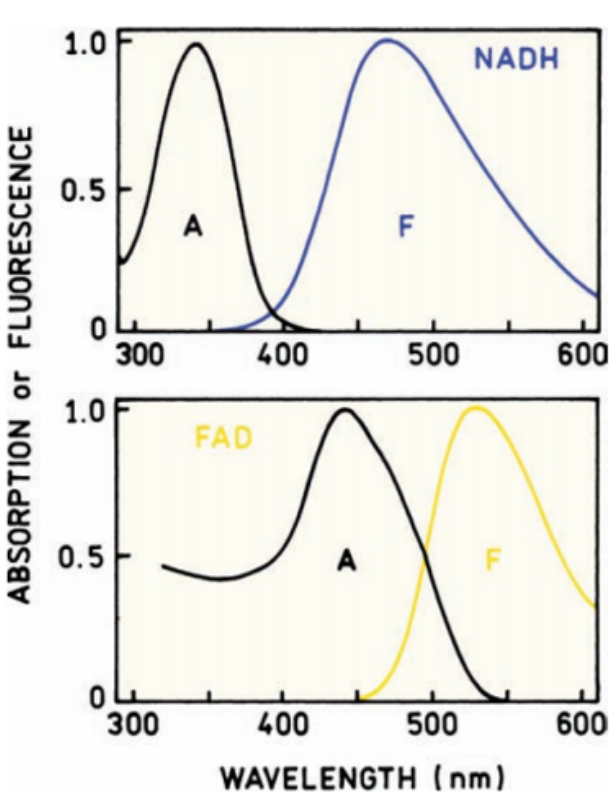

Figure 2.3: *Absorption and emission spectra of the enzyme cofactors NADH and FAD [3].*

Nucleotides and nucleic acids are generally non-fluorescent, however, some exceptions exist. Yeast tRNAPHE contains a highly fluorescent base, known as the Y-base, which has an emission maximum near 470 nm and a lifetime near 6 ns. The molecules described above represent the dominant fluorophores in animal tissues.

There is presently interest in the emission from intrinsic fluorophores

from tissues, from fluorophores that are not enzyme cofactors. Much of the fluorescence from cells is due to NADH and flavins. Other fluorophores are seen in intact tissues, such as collagen, elastin lipo-pigments and porphyrins (Figure 2.4). In these cases, the emission is not due to a single molecular species but represents all the emitting structures present in a particular tissue. The emitting species are thought to be due to crosslinks between oxidized lysine residues that ultimately result in hydroxypyridinium groups. Different emission spectra are observed with different excitation wavelengths. Much of the work is intrinsic tissue fluorescence, to identify spectral features that can be used to identify normal versus cancerous tissues, and other disease states.

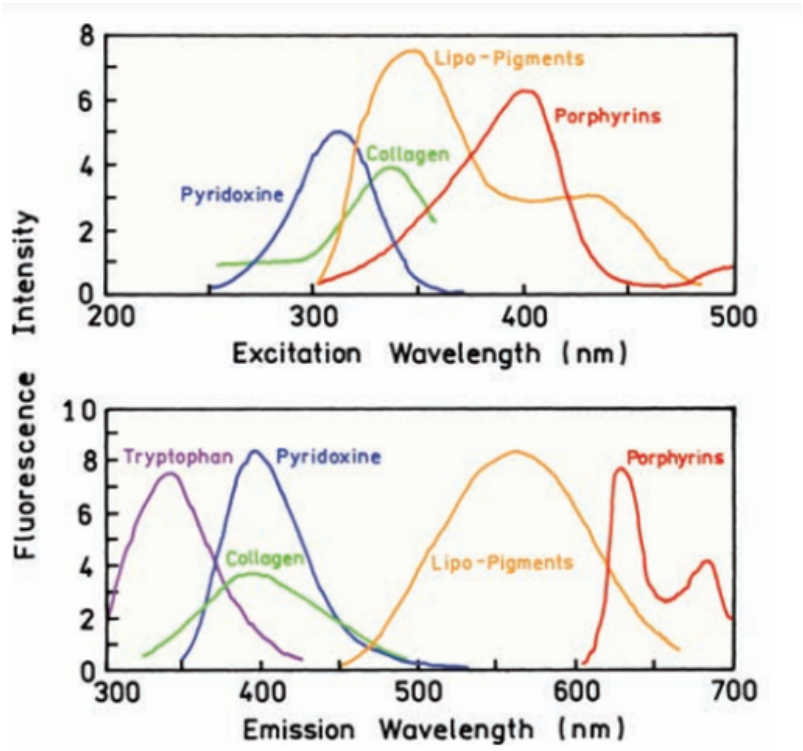

Figure 2.4: *Emission spectra from intrinsic tissue fluorophores [3].*

2.1.3 Extrinsic fluorophores

Frequently the molecules of interest are non-fluorescent, or the intrinsic fluorescence is not adequate for the desired experiment. For instance, DNA and lipids are essentially devoid of intrinsic fluorescence, so in these cases useful fluorescence is obtained by labelling the molecule with extrinsic probes. For proteins it is frequently desirable to label them with chromophores with longer excitation and emission wavelengths than the aromatic amino acids. Then the labelled protein can be studied in the presence of other unlabelled proteins [3].

Protein-Labelling Reagents

Numerous fluorophores are available for covalent and non-covalent labelling of proteins. The covalent probes can have a variety of reactive groups, for coupling with amines and sulfhydryl or histidine side chains in proteins.

Dansyl chloride (DNS-Cl) is widely used to label proteins, especially where polarization measurements are anticipated. This wide use is a result of its early introduction in the literature and its favourable lifetime (10 ns). Dansyl groups can be excited at 350 nm, where proteins do not absorb. Since dansyl groups absorb near 350 nm they can serve as acceptors of protein fluorescence. The emission spectrum of the dansyl moiety is also highly sensitive to solvent polarity and the emission maxima are typically near 520 nm (Figure 2.5).

Fluoresceins and rhodamines are also widely used as extrinsic labels (Figure 2.6). These dyes have favourably long absorption maxima near 480 and 600 nm and emission wavelengths from 510 to 615 nm, respectively. In contrast to the dansyl group, rhodamines and fluoresceins are not sensitive to solvent polarity. An additional reason for their widespread use is the high molar extinction coefficients near 80,000 $M^{-1}\ cm^{-1}$. A wide variety of reactive derivatives are available, including iodoacetamides, isothiocyanates, and maleimides.

The BODIPY dyes have been introduced as replacements for fluo-

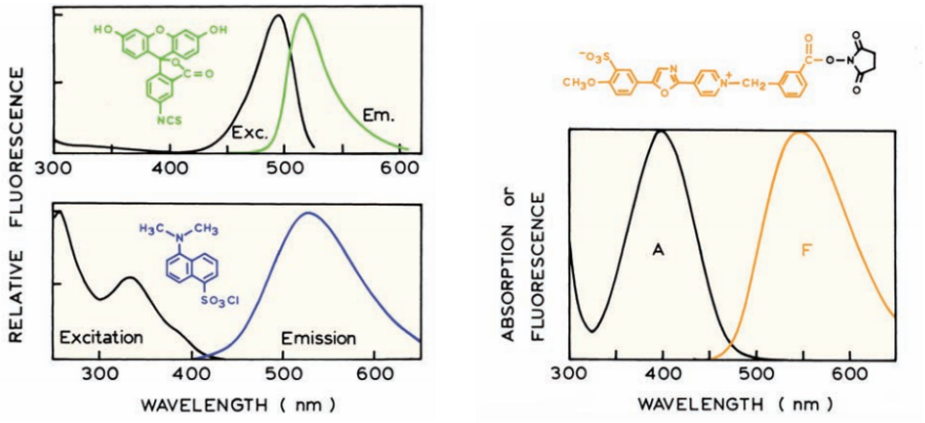

Figure 2.5: *excitation and emission spectra of FITC (top left) and DNS-CI (bottom lef) and Cascade Yellow (right) [3].*

rescein and rhodamines. These dyes are based on an unusual boron-containing fluorophore (Figure 2.7). Depending on the precise structure, a wide range of emission wavelengths can be obtained, from 510 to 675 nm. The BODIPY dyes have the additional advantage of displaying high quantum yields approaching unity, extinction coefficients near 80,000 M^{-1} cm^{-1}, and insensitivity to solvent polarity and pH.

The emission spectra are narrower than those of fluorescein and rhodamines, so that more of the light is emitted at the peak wavelength, possibly allowing more individual dyes to be resolved. A disadvantage of the BODIPY dyes is a very small Stokes shift. As a result the dyes transfer to each other with a Förster distance near 57 Å [3].

One problem with fluoresceins and rhodamines is their tendency to self-quench. It is well known that the brightness of fluorescein-labelled proteins does not increase linearly with the extent of labelling. In fact, the intensity can decrease as the extent of labelling increases. This effect can be understood by examination of the excitation and emission spectra (Figure 2.5). Fluorescein displays a small Stokes shift: when more than a single fluorescein group is bound to a protein there can be energy transfer between these groups. This can be understood by realizing that two fluorescein groups attached to the same protein are likely to be within 40

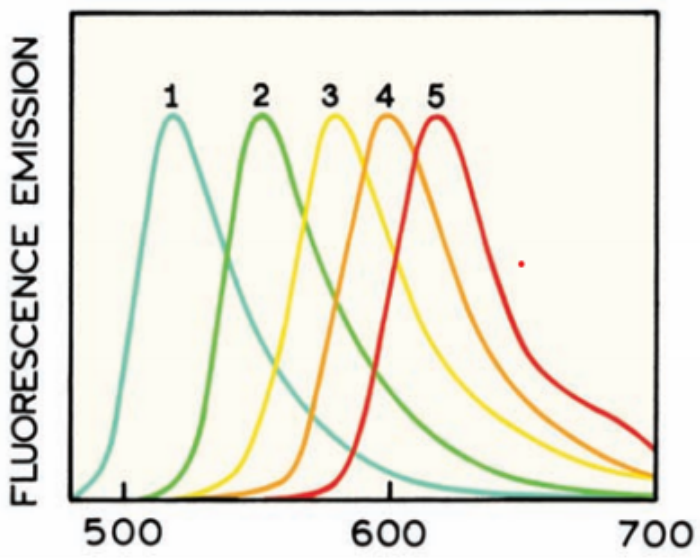

Figure 2.6: *Structure and normalized fluorescence emission spectra of goat anti-mouse IgG conjugates of (1) fluorescin, (2) rhodamine 6G, (3) tetramethylrhodamine, (4) Lissamine rhodamine B and (5) Texas Red dyes [3].*

Å of each other, which is within the Förster distance for fluorescein-to-fluorescein transfer.

The BODIPY dyes have a small Stokes shift and usually display self-quenching. New dyes are being developed that show both a large Stokes shift and good water solubility. One such dye is Cascade Yellow, which displays excitation and emission maximum near 409 and 558 nm, respectively (Figure 2.5).

In contrast to fluorescein, rhodamines, and BODIPYs, there are fluorophores that display high sensitivity to the polarity of the local environment. One example is Prodan35, which is available in the reactive form—called acrylodan. In the excited state there is a charge separation from the amino to the carbonyl groups. When bound to membranes, Prodan and its derivatives display large spectral shifts at the membrane phase-transition temperature.

Another important property of a probe is its photostability. Almost all fluorophores are photobleached upon continuous illumination, especially in

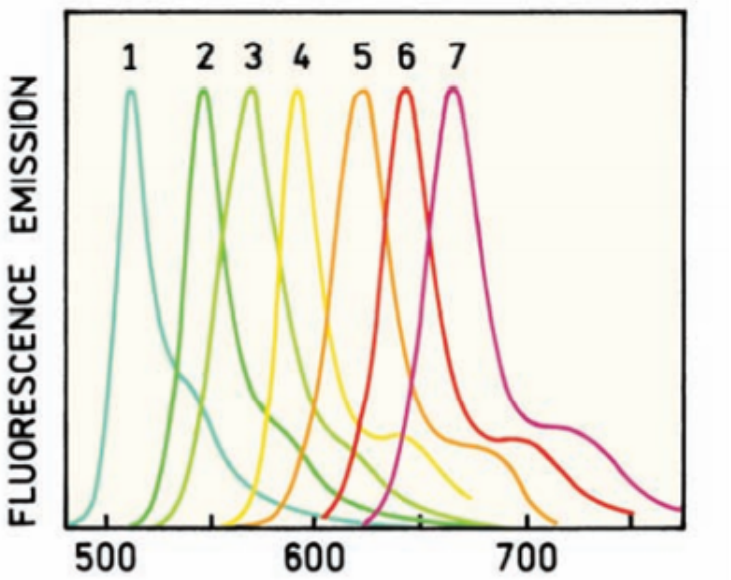

Figure 2.7: *Normalized fluorescence emission spectra of BODIPY fluorophores in methanol [3].*

fluorescence microscopy where the light intensities are high. Fluorescein is one of the least photostable dyes. The photostability of a dye can be affected by its local environment. In some cases, photostability is increased by removal of oxygen, and in other cases oxygen has no effect. There appears to be no general principles that can be used to predict photostability.

Finally, there are a number of dyes that can be used to non-covalently label proteins. These are typically naphthylamine sulfonic acids, of which 1-anilinonaphthalene-6-sulfonic acid (ANS) and 2-(p-toluidinyl)naphthalene-6-sulfonic acid (TNS) are most commonly used. Dyes of this class are frequently weakly or non-fluorescent in water, but fluoresce strongly when bound to proteins or membranes. Figure 2.8 shows the emission spectra of BSA excited at 280 nm as the sample is titrated with ANS. In the absence of BSA the emission from the ANS dissolved in buffer would be insignificant.

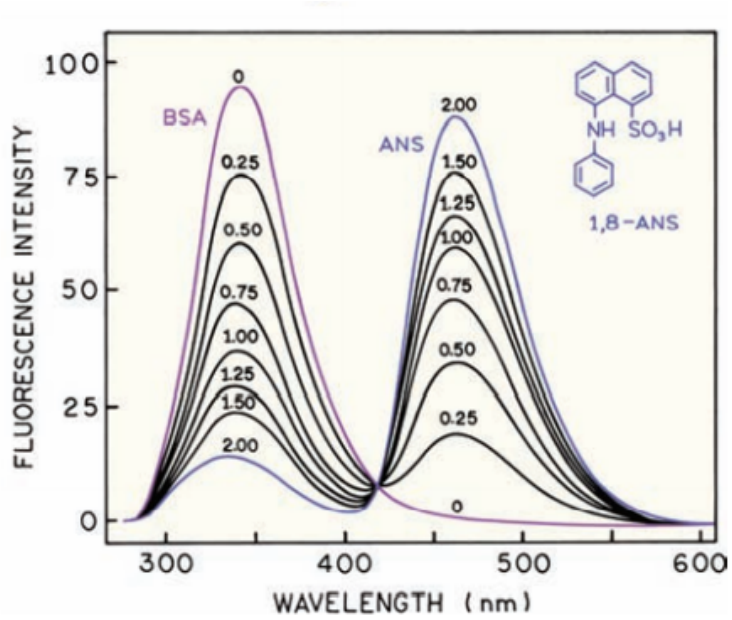

Figure 2.8: *Fluorescence emission spectra of bovine serum albumin(BSA) in the presence of increasing ANS concentration. The numbers indicate the average number of ANS molecules bound per BSA molecule. Excitation at 280 nm. The structure shows the crystal structure of HSA modified to contain two tryptophanes [3].*

Red and Near-Infrared (NIR) Dyes

Long-wavelength probes are of current interest for several reasons. The sensitivity of fluorescence detection is often limited by the autofluorescence of biological samples. As the excitation wavelength becomes longer, the autofluorescence decreases, and hence visibility over background increases. Long-wavelength dyes can be excited with laser diodes. The most familiar long-wavelength dyes are the cyanine dyes, such as the Cy-3, Cy-5 and Cy-7 in Figure 2.9. Such dyes have absorption and emission wavelengths above 550 nm. The cyanine dyes typically display small Stokes shift, with the absorption maxima about 30 nm blue shifted from the emission maxima, as shown for Cy3.

Additional long-wavelength dyes can be discussed: some rhodamine derivatives display long absorption and emission spectra, like Rhodamine 800, or extended conjugated systems result in long absorption and emis-

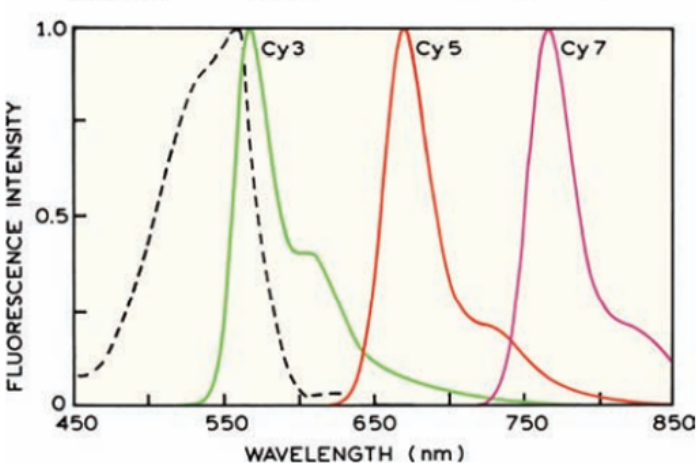

Figure 2.9: *Chemically reactive cynine dyes. The dashed line shows the absorption spectrum of Cy3 [3].*

sion wavelengths, as for IR-125 and thiazole orange. Dyes of this class have been extensively characterized for use as long-wavelength probes and in DNA sequencing. The dye thiazole orange can be excited at 735 nm and binds strongly to DNA. Dyes of this type are also used for staining DNA restriction fragments during capillary electrophoresis (CE).

DNA Probes

While very weak intrinsic emission has been observed from unlabelled DNA, this emission is too weak and too far in the UV for practical applications. Fortunately, there are numerous probes that spontaneously bind to DNA and display enhanced emission. One of the most widely used dyes is ethidium bromide (EB). EB is weakly fluorescent in water, and its intensity increases about 30-fold upon binding to DNA. The lifetime of ethidium bromide is about 1.7 ns in water and increases to about 20 ns upon binding to double-helical DNA.

In recent years improved DNA dyes have been developed that bind to DNA with high affinity. Typical high-affinity dyes are dimers of known DNA probes, such as the ethidium homodimer and elongated positively charged dyes like TOTO-1. Such dyes remain bound to DNA during gel

electrophoresis and allow DNA detection with high sensitivity [3].

Green Fluorescent Proteins

An important addition to the library of probes has been the green fluorescent protein (GFP) from the bioluminescent jellyfish Aequorea victoria.

GFP contains a highly fluorescent group within a highly constrained and protected region of the protein. The remarkable feature of the GFP is that the chromophore forms spontaneously on folding of the polypeptide chain without the need for enzymatic synthesis. As a result, it is possible to express the gene for GFP into cells and to obtain proteins which are synthesized with attached GFP. GFPs with different spectral properties have been created by introducing mutations into the amino-acid sequence. Mutants are known that display longer absorption and emission wavelengths and have higher photostability. In general, GFPs have good photostability and display high quantum yields. The fluorophores in GFPs are formed autocatalytically, and it is not necessary to add a fluorophore or enzymes to synthesize the fluorophore. All that is needed is the gene or mRNA that codes for the amino-acid sequence. As a result, organisms that contain the gene or mRNA can express the fluorescent protein [3].

Long Lifetime Probes

The probes described above were organic fluorophores with a wide variety of spectral properties, reactivities, and environmental sensitivities. While there are numerous organic fluorophores, almost all display lifetimes from 1 to 10 ns, which limit the dynamic information content of fluorescence. There are several exceptions to the short lifetimes of organic fluorophores. Pyrene displays a lifetime near 400 ns in degassed organic solvents. Pyrene has been derivatized by adding fatty acid chains, which typically results in decay times near 100 ns. In labelled macromolecules the intensity decays of Pyrene and its derivatives are usually multi-exponential.

Another long-lived organic fluorophore is coronene, which displays a

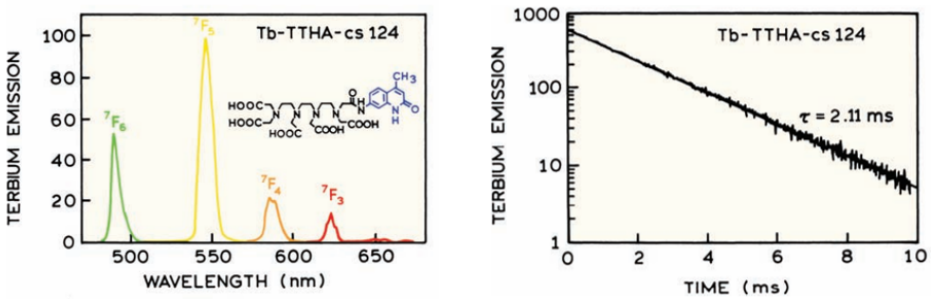

Figure 2.10: *emission Spectrum (left) and intensity decay (right) of the Lanthanide terbium. [3].*

lifetime near 200 ns. In membranes the intensity decay of coronene is multi-exponential. Coronene has also been conjugated to lipids.

Furthermore, there are two types of organometallic fluorophores which display long lifetimes and other unique features which allow new types of experiments: the lanthanides and the transition metal complexes.

The lanthanides are uniquely fluorescent metals that display emission in aqueous solution and decay times of 0.5 ms to 3 ms. Emission results from transitions involving 4f orbitals, which are forbidden transitions. As a result, the absorption coefficients are very low, less than 10 $M^{\breve{}1}$ $cm^{\breve{}1}$, and the emissive rates are slow, resulting in long lifetimes. Because of the weak absorption, lanthanides are usually not directly excited, but rather excited through chelated organic ligands. Hence, the excitation spectrum of the complex shown in Figure 2.10 reflects the absorption spectrum of the ligand and not the lanthanide itself.

Lanthanides possess some favourable properties as biochemical probes. Their decay times when bound to proteins can be used to calculate the number of bound water molecules in a calcium binding site.

Lanthanides have found widespread use in high sensitivity detection, particularly for immunoassays. The basic idea is shown in Figure 2.11. All biological samples display autofluorescence, which is usually the limiting factor in high sensitivity detection. The autofluorescence usually decays on the nanosecond timescale, as do most fluorophores. Because of their long decay times, the lanthanides continue to emit following dis-

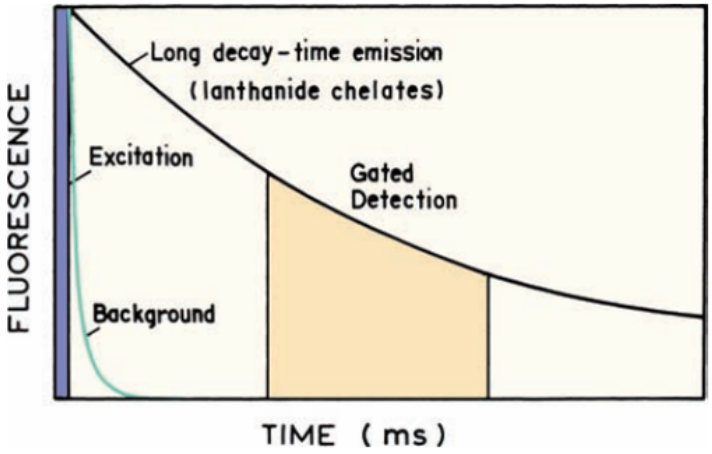

Figure 2.11: *Principle of Time resolved detection in lanthanide immunoassays. [3].*

appearance of the autofluorescence. The detector is turned on after the excitation flash to integrate the intensity from the lanthanide. These time-gated immunoassays are essentially steady-state intensity measurements in which the intensity is measured over a period of time following pulsed excitation.

However, the lanthanides do suffer several limitations. One is the need to chelate the lanthanide in order to obtain significant excitation: the requirement often results in multi-step assays, the last step being addition of the chelator. Another difficulty is the absence of polarized emission, so that the lanthanides cannot be used for anisotropy measurements.

The other class of probes with long lifetimes are the transition metal complexes. These are typically complexes of ruthenium (Ru II), rhenium (Re I), or osmium (Os II) with one or more diimine ligands (Figure 2.12). In contrast to the lanthanides, these compounds display molecular fluorescence from a metal-to-ligand charge-transfer state. The transition is partially forbidden, so that the decay times are long. These complexes are highly stable, like covalent bonds, so there is no significant dissociation of the metal and ligands. Transition metal complexes display lifetimes ranging from 10 ns to 10 μs. For example, Ru(bpy)2(mcbpy) in Figure 2.12

displayed a decay time near 400 ns when conjugated to proteins and lipids. The MLC probes are highly photostable, and display large Stokes shifts,

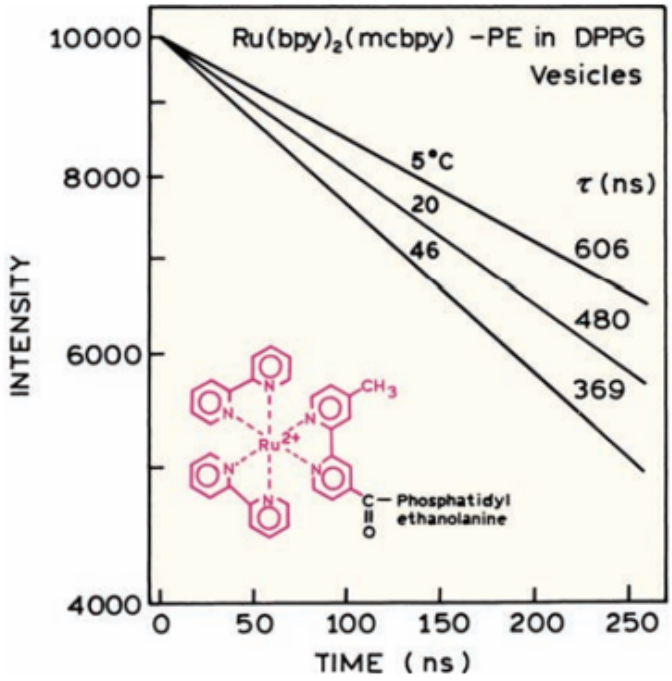

Figure 2.12: *Intensity decay of Ru(bpy)2(mcbpy)-PE in DPPG vesicles. [3]*

so that probe–probe interactions are not expected. These molecules are known to display polarized emission and are thus useful for measurement of dynamic processes on the microsecond timescale [3].

2.2 Pyrene

In LINUS project we chose to use Pyrene as fluorescent probe for the first tests with the experimental setup. There are multiple reasons for this selection, depending principally by its physical properties and general costs:

- Pyrene displays long lifetime (>100 ns), that is strictly necessary for our system to work properly (this point will be explained in detail in chapter 3).

- Its emission spectrum has maximum values between the wavelengths of 370 nm and 400 nm, which has a perfect matching with the sensitive region of detection of the SiPM.

- It presents reasonable costs in respect to other long-lifetime probes (like lanthanides) and it is easy to find on the market.

Pyrene is one of the most well-studied polycyclic aromatic hydrocarbons (PAHs) because of its characteristic photophysical properties, such as prominent absorption bands and a fluorescence emission. These properties can be tailored to meet specific requirements through modifications of its chemical structure; therefore, Pyrene derivatives are recognized as promising materials for organic light-emitting devices.

Pyrene is also well known for the formation of an excimer. An aromatic excimer is a dimeric complex of the same aromatic molecules that is formed in the excited state. The fluorescence emission of an excimer was firstly observed for a Pyrene solution by Förster and Kasper in 1954. The excimer fluorescence emission band is significantly red-shifted, broad, and structureless, so that it is clearly distinguishable from that of the monomer. Given the substantial distinction between monomer and excimer emissions, as well as their sensitivity to the surrounding environments, Pyrene is used to study the molecular structural properties of polymers and macromolecules, such as proteins and DNA.

Pyrene fluorescence emission spectrum is very sensitive to solvent polarity, so Pyrene has been used as a probe to determine solvent environments. This is due to its excited state having a different, non-planar structure than the ground state. Certain emission bands are unaffected, but others vary in intensity due to the strength of interaction with a solvent [12]. The vibrational structure of the emission spectrum of Pyrene is constituted by five fine peaks, named I_1, I_2, I_3, I_4, and I_5 (Figure 2.13). An increase of the intensity of peak I_1 is observed in polar solvents, while I_3 is solvent insensitive. Thus, the evolution of the ratio of intensities I_1/I_3 gives information on the evolution of the polarity of the environment close to molecular Pyrene.

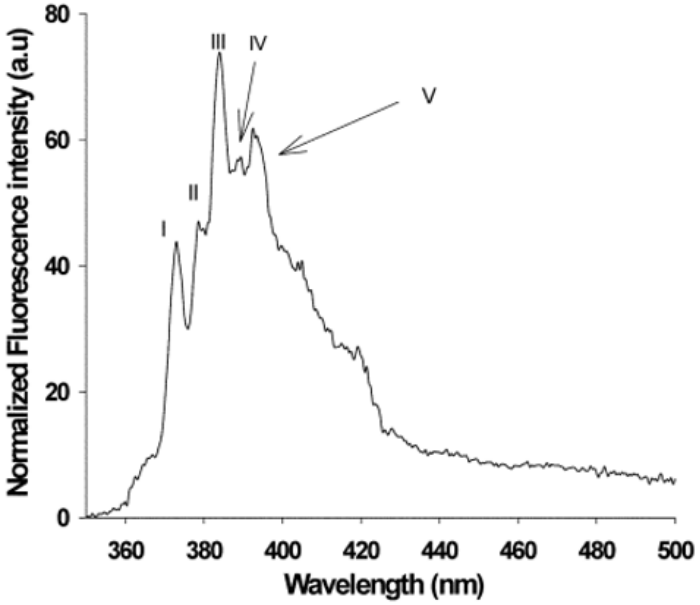

Figure 2.13: *Resolved fluorescence spectrum of Pyrene in cyclohexane solution showing the assignment of peaks I to V [13].*

Table 2.2: Chemical and physical properties of Pyrene

Chemical formula	$C_{16}\ H_{10}$
Molar mass	202.256 $gmol^{-1}$
Density	1.271 $\frac{g}{mol^{-1}}$
Melting point	145 to 148 °C
Boiling point	404 °C
Solubility in water	0.135 $\frac{mg}{L}$

2.2.1 Fluorescent properties

As we say before, among the fluorescent probes, pyrene has been widely used because from its emission characteristics (in particular the ratio of the first and third vibronic peaks; I_1/I_3) we can estimate the polarity level of its environment [14]. The absorption and emission spectra of Pyrene (2 μM) in water, methanol and hexane are illustrated in Figures 2.14a and 2.14b. The absorption spectra have evidenced eight peaks strong (s) and weak (w) at 232w, 242s, 252w, 260w, 272s, 308w, 320s and 336s nm as depicted in Figure 2.14a

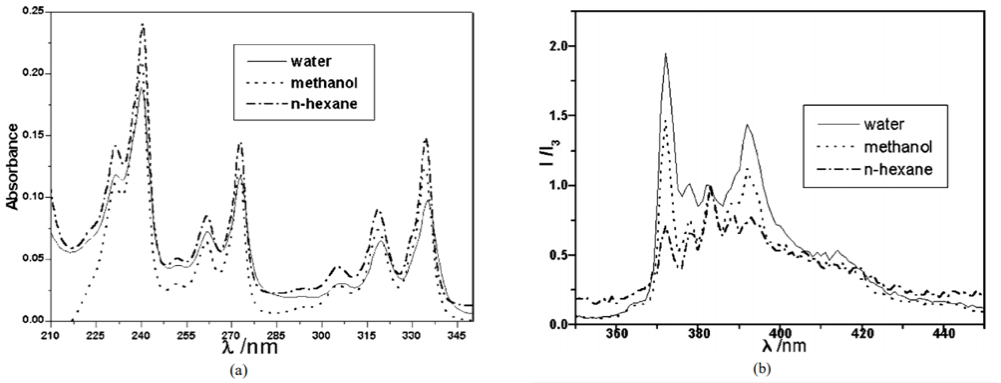

Figure 2.14: *Pyrene spectrum in water, methanol and hexane [14].*

The spectra have shown solvent dependence. At 242 nm, the trend of absorption was n-hexane > methanol > water, which changed to n-hexane < water < methanol up to 315 nm; thereafter, the trend of absorbance became water < methanol < n-hexane. The solvent dependent intensities of the effective part of the emission spectra between 370 and 410 nm followed the order water > methanol > n-hexane i.e. in order of decreasing solvent polarity. There were five emission peaks at 373, 379, 383, 389 and 393 nm for pyrene. In Figure 2.14b , the fluorescence intensities normalized against the intensity of the third peak are plotted against the wavelengths. Other experiment in different solvents show significantly changes in Pyrene emission spectrum depending on the polarity [14].

For our test, we are interested in Pyrene properties in water. From the Figure 2.15a and Figure 2.16, we learnt that the main wavelengths of absorbance are 240 nm, 275 nm and 320 nm, while the emission peaks are at 375 nm and 395 nm. This information will be important for the choice of the LED, based on the wavelength of absorbance, and the type of SiPM, based on the wavelength of emission. The extinction coefficient at 240 nm is about 3.5, while at 275 nm is circa 1.

Regarding the quantum yield, we know that it expresses the number of photons that are absorbed by the fluorophore in respect to all photons emitted by the source light. In literature, it is reported that Pyrene quantum yield in water is around 0.7 (similar to the value in ethanol). Finally,

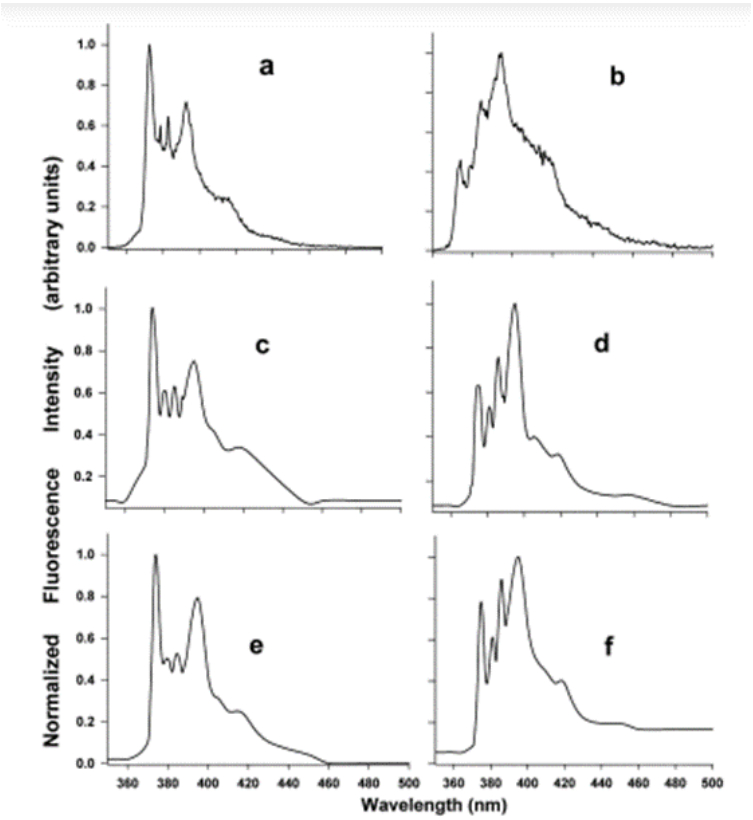

Figure 2.15: *Pyrene emission spectra measured (a) in pure water, (b) in pure hexanoic acid, (c) at the air-water interface, (d) at the air-hexanoic acid interface; haxanoic acid-coated air-water interfaces with (e) sub-monolayer; and (f) multilayer coverages of hexanoic acid [13].*

it has been demonstrated that the environment can also change the lifetime of Pyrene [15]. As usual we pay attention to the value in water, that is around 200 ns. For our tests and design the values of interest are summarized in Table 2.3.

2.3 SiPM photodetectors

Silicon Photomultipliers (SiPMs) have been firstly developed in 1997 [16] (at first they were called Metal-Resistive layer-Semiconductor APDs, or MRS-APDs) and, thanks to their substantial advantages compared with Photomultiplier Tubes (PMTs), they attracted the attention of researchers,

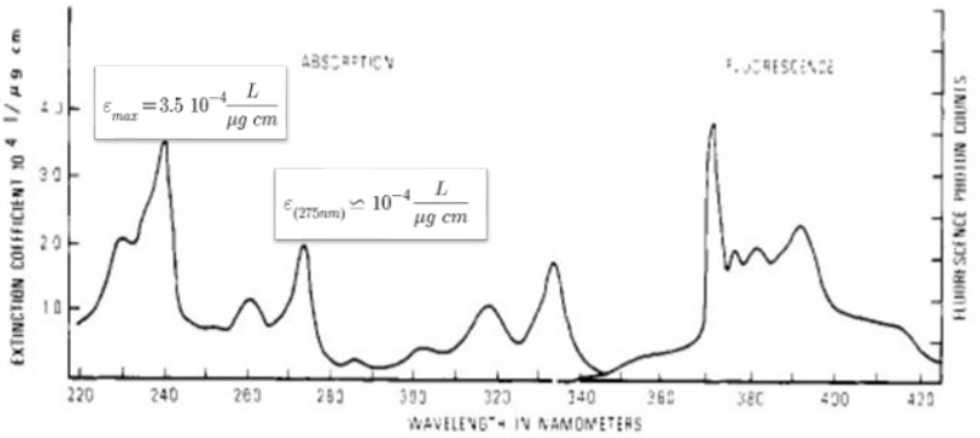

Figure 2.16: *Absorption and emission spectrum of Pyrene in water of 165μg/L [15].*

Table 2.3: Pyrene in water, values of interest.

Absorption spectrum (main peaks)	242 nm; 272 nm; 320 nm; 336 nm
Emission spectrum (main peaks)	373 nm; 379 nm; 383 nm; 389 nm; 393 nm
Fluorescence lifetime	200 ns
Quantum Yield	0.7
Extinction coefficient	3.5 10^{-4} $L/(\mu gcm)$ at 242 nm
	1 10^{-4} $L/(\mu gcm)$ at 272 nm

especially for nuclear and medical applications, leading to significant advances in their technology. The major benefits of SiPMs compared to PMTs can be summarized as follows:

- High internal gain, comparable to that of PMTs, that strongly reduces the impact of the electronics noise from the analog front-end.
- Bias voltage ranging from 25 V and 80 V, depending on the breakdown voltage of the photodetector itself, instead of the thousands of volts required to bias a photomultiplier tube.
- Magnetic compatibility, which opens a wide range of possibilities in medical application in which PMT could not be used.
- Fast response, which makes SiPMs well suited for highly demanding

timing applications.

- Mechanical robustness and compact size allow to design much more compact and tough modules.
- High degree of fabrication uniformity offered by technological development of modern semiconductor facilities.

2.3.1 SiPM structure

A Silicon Photomultiplier is constituted by a parallel array of photon counting micro-cells (figure 2.17).

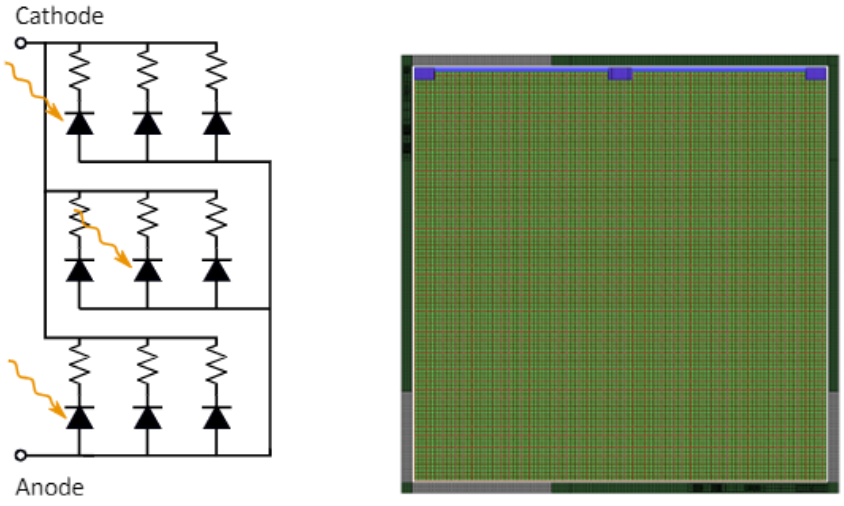

Figure 2.17: *SiPM equivalent circuit and picture of a 4mm×4mm SiPM from FBK with cell area of 40μm×40μm.*

Each microcell consists of a Geiger Mode Avalanche Photodiode(GM-APD) (also called Single Photon Avalanche Diode (SPAD)) with an integrated quenching element[17].

SPADs are devices operated above the breakdown voltage: an electron-hole pair can be generated in the depleted region through the absorption of a photon, and these free carriers, accelerated by a strong electric field,

originate a self-sustaining current by means of impact ionization. In order to stop the avalanche, in silicon photomultipliers is implemented in series to the avalanche diode a passive quenching resistor, that produces a voltage proportional to the avalanche current and reduces the voltage across the junction below the breakdown voltage, quenching the avalanche. As no more current flows, the diode depletion capacitance is recharged to the bias voltage, and a new avalanche can be triggered.

Each microcell features a bi-stable behaviour, as the avalanche itself is not proportional to the number of generating events, since the cell is no more sensitive till the bias voltage has been restored on the photodetector depletion capacitance, and no further events will generate signals. The avalanche breakdown is originated by an Electron-Hole Pair (EHP): in semiconductors, the EHP can be originated by the absorption of a photon, thermal agitation and tunnelling effect. All these effects are indistinguishable from each other and since the thermal agitation and tunnelling effect are undesired and unavoidable, they are treated as noise sources and called dark count events. The typical response of a silicon photomultiplier is shown in figure 2.18, together with the distribution of the acquired signal amplitudes. The signal is clearly quantized, and the contributions of single photons are clearly visible.

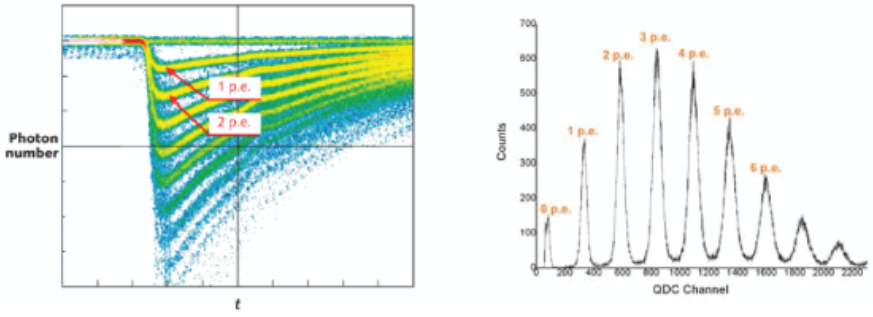

Figure 2.18: *SiPM typical response acquired with oscilloscope along with the acquired signal spectrum.*

2.3.2 Electrical model for SiPM

In order to understand the electrical behaviour of the photodetector a very simple model, represented in figure, can be used to estimate with reasonable accuracy the response of the SiPM, and to characterize the current pulses provided by the photodetector. In the figure, R_S is the photode-

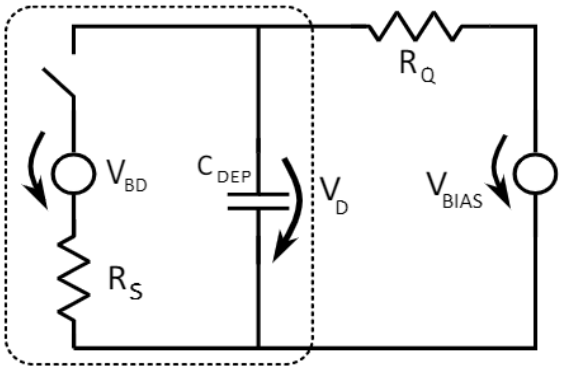

Figure 2.19: *SiPM equivalent circuit: when the avalanche is triggered the switch isconsidered closed, open otherwise.*

tector series resistance, $C_{DEP}$is the photodetector depletion capacitance, in the order of tens of fF [18], V_{BD} is the breakdown voltage, R_Q is the quenching resistance, typically in the order of hundreds of $k\Omega$ to some $M\Omega$ [19], and V_{BIAS} is the bias voltage, higher than V_{BD}, that generates the high electric field that sustains the avalanche. When no avalanche is triggered, the switch is considered open: in this condition the voltage across the depletion capacitance of the photodetector C_{DEP} is equal to V_{BIAS}, and no current flows. As soon as the avalanche is triggered, the switch closes and a current $I_{DET,peak}$ is reached, where:

$$I_{DET,peak} = \frac{V_{BIAS} - V_{BD}}{R_S + R_Q} \tag{2.3}$$

The quantity $V_{BIAS} - V_{BD}$ is commonly referred to as Over Voltage (V_{OV}). As it is typically verified, $R_Q >> R_S$, and so the junction voltage V_D results almost equal to V_{BD}. The voltage V_D drops with the same time constant as the photodetector current I_{DET} rises, and can be estimated

as:

$$\tau_{rise} = C_{DEP} \times R_S \tag{2.4}$$

As the electric field across the junction decrease, due to the voltage drop on R_Q that reduces V_D, the avalanche extinguishes and no more current flows. This behaviour is modelled by opening the switch, and the voltage V_D is reset to V_{BIAS} with the slower time constant:

$$\tau_{reset} = C_{DEP} \times R_Q \tag{2.5}$$

Only when V_D reaches V_{BIAS} the microcell is ready to trigger another avalanche. The current pulse supplied by the photodetector, according to the model, is represented in figure

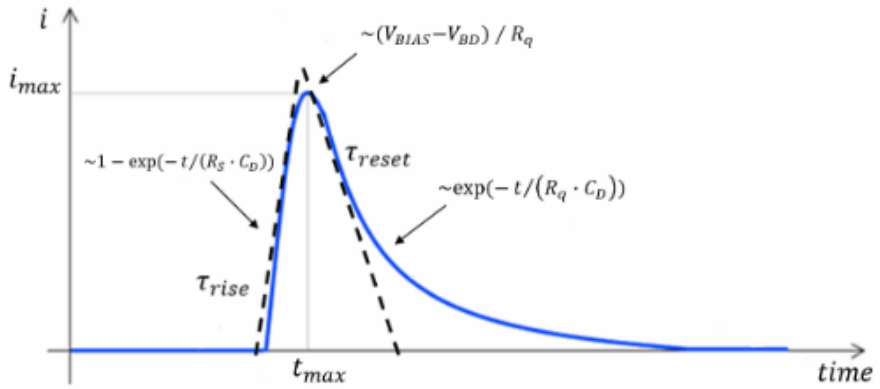

Figure 2.20: *SiPM output current signal shape according to the proposed model.*

Despite the simplicity and utility of the proposed model, it also features some limitations, arising from the fact the loading effects of all the other microcells have been completely neglected. More complete models, less handy but more accurate, can be considered to account second order effects [17].

2.3.3 Main Figures of Merit of SiPMs

Photon Detection Efficiency

The Photon Detection Efficiency (PDE) is defined as the probability foran impinging photon to develop an electrical signal. It is intuitive toexpress this quantity as the joint probability for a photon to be impingingon the active area of the photodetector, to be absorbed in silicon, and toeffectively trigger the avalanche, leading to the following expression:

$$PDE = QE \times FF \times P_{trigger}(V) \tag{2.6}$$

where FF represent the Fill Factor, QE(λ)the Quantum Efficiency and $P_{trigger}$(V) the avalanche triggering probability.

The Fill Factor is a geometrical parameter dependent on the layout of the microcell, defined as the ratio between the active area and the overall area of a microcell. The dead area is mainly attributable to the quenching resistor and guard rings.However, increasing the size of the cell, for the same quenching resistor the fill factor improves, as the relative weight of the dead area reduces, but a larger active area lead to a larger depletion capacitance, thus to as lower response of the device. Moreover, for SiPM of the same overall size, larger cells lead to a lower total number of cells, thus decreasing the dynamic range of the photodetector. The trade-off must be considered during design, in order to obtain the best performances for the target application.

The Quantum Efficiency, is the probability for a photon impinging on the active area to be absorbed generating an electron-hole pair in themedium. This quantity is related to the promotion of valence electrons in conduction band and therefore is a function of the wavelength of the impinging photon and the absorption material (Silicon in this case). The quantum efficiency can reach values as high as 98 % by means of proper anti-reflecting coating layers deposited over the SiPM active area.

Triggering probability depends on how likely is for a carrier to trigger

an avalanche and it can be expressed as:

$$P_{trigger} = P_e + P_h - P_e \times P_h \tag{2.7}$$

where P_e and P_h are the probability to trigger an avalanche for an electron and a hole respectively. Being related to the electric field in the depletion region, this quantity is a function of the SiPM bias voltage.

Dynamic Range and Linearity

SiPMs are constituted by an array of elementary microcells. The maximum signal that can be provided by a SiPM photodetector corresponds to the case in which every cell has been triggered, while the minimum signal consist in the output signal of a single cell. However the detection of photons is a statistical process, based on the probability of detecting a certain number of photons by a limited number of sensitive microcells. For this reason, the output signal of a SiPM is influenced by the statistical fluctuations that two or more photons hit the same cell. The average number of firing microcells N_{fired} as a function of the number of impinging photons N_{ph}, given a certain number of cells N_{cell} and PDE can be computed as:

$$N_{fired} = N_{cell} \times (1 - e^{\frac{PDE \times N_{ph}}{N_{cell}}}) \tag{2.8}$$

According to this formula, it is evident that the output signal of a photodetector is proportional to the number of impinging photons only as far as $N_{ph} << N_{cell}$. Saturation effects are explained from the fact that for a large number of photons, comparable to the number of the microcells, the probability of multiple photons hitting the same cell becomes significant [17].

Gain

The gain of a SiPM sensor is defined as the number of carriers involved in the avalanche current for a single microcell. SiPMs generate a highly uniform number of carriers each time an avalanche event happens. The

average gain can be computed as the charge delivered from the photodetector with respect to the elementary electron charge, according to:

$$G = \frac{C_{cell} \times (V_{BIAS} - VBD)}{q} \tag{2.9}$$

Clearly the gain of a SiPM can be increased by increasing the over voltage or using large microcell photodetectors, that feature larger depletion capacitance. Typical available gain values from commercial SiPMs are larger than 1×10^6, even larger than that of some high quality Photomultiplier Tube. Usually gain is in trade-off with response speed and noise performances, as increasing the the photodetector depletion capacitance will cause a slower response, and increasing the over voltage leads to a higher Dark Count Rate, as will be discussed in the dedicated section. The dependence on cell size (capacitance) at different over voltages is shown in figure 2.21.

Dark count

In parallel with photon absorption, also thermal agitation and tunnelling effect can generate free carriers by promoting carriers from valence to conduction band, that, accelerated by the electric field, can eventually trigger the avalanche. All the processes cause the same output signals and hence they are not distinguishable. Thermal promotion and field-assisted charge generation by tunneling are distributed in time following the Poisson statistic, and are independent on the irradiation condition of the photodetector. Usually, datasheets refer to these effects as Dark Count Rate (DCR), which is the mean frequency at which avalanches are randomly triggered without light sources, and it is quoted in kHz/mm^2 [17].

The two effects depend respectively on temperature and to the Over Voltage applied to the photodetector, as it can be seen from figure 2.22.

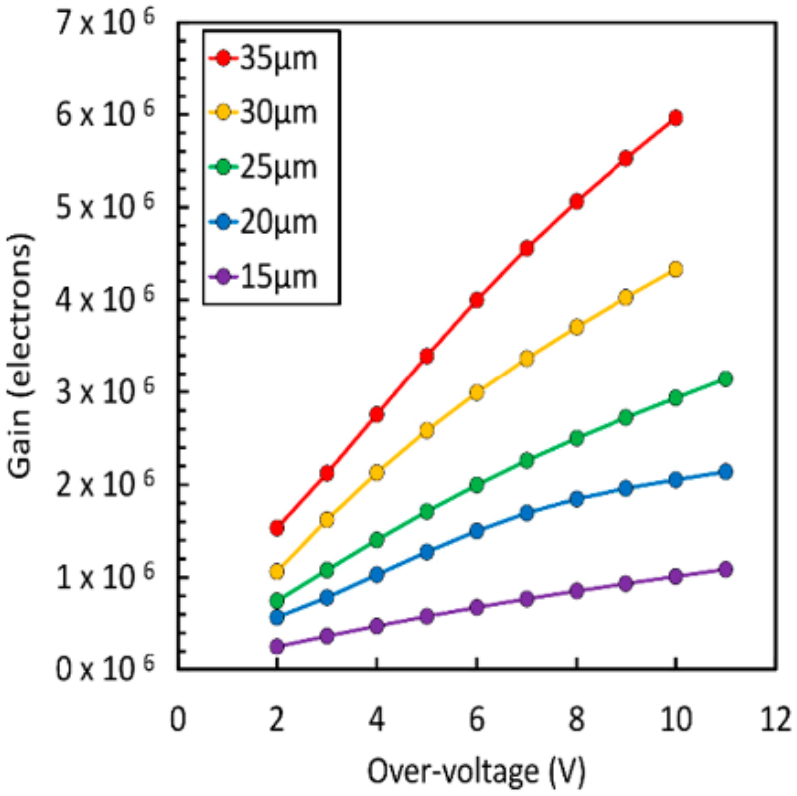

Figure 2.21: *Dependence of NUV-HD SiPM gain on cell size at different overvoltages.*

Correlated Noise

Along with dark count, optical crosstalk and after pulses are phenomena contributing to the overall noise of SiPMs. They are referred to as correlated noise since they happen with a certain probability when a photon is absorbed in silicon, and so, they are correlated with the signal. In particular, optical crosstalk is caused by the finite probability of photon emission during the avalanche breakdown, and can take place through two different mechanism: Direct Crosstalk (DiCT) and Delayed Crosstalk (DeCT).

The former happens when the generated photon moves directly towards the depletion region of an adjacent microcell and triggers new avalanches, almost simultaneously to the signal generated one, thus a sin-

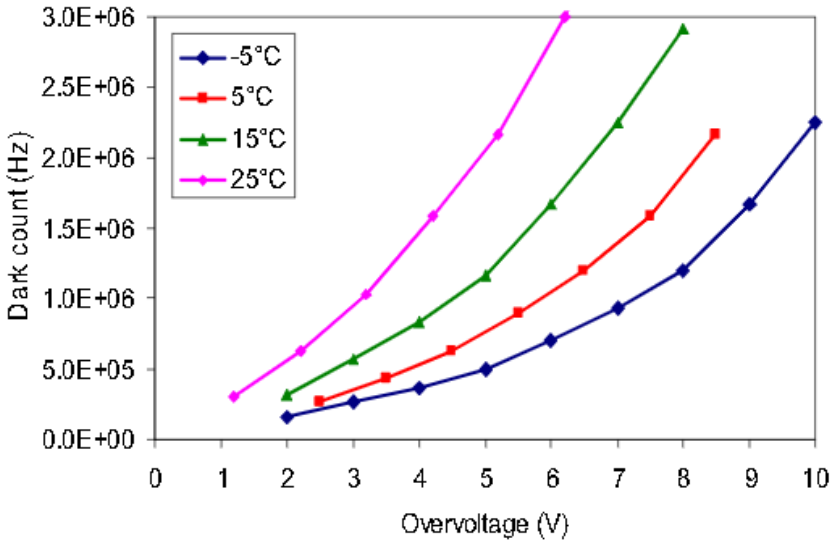

Figure 2.22: *Dark Count Rate as function of the overvoltage at different temperatures in a FBK SiPM.*

gle photon can lead to an erroneous output signal, equivalent to a number of photons greater than one. Delayed crosstalk happens, instead,when the generated photon creates an electron-hole pair outside the depletion region (the substrate for example) of an adjacent microcell. This electron-hole pair can trigger an avalanche only if it reaches the active region of the cell by diffusion; therefore delayed crosstalk leads to the appearance of a succession delayed pulses, randomly distributed in time. Optical crosstalk can be reduced increasing the distance between microcells (but at the cost of reducing the Fill Factor) or inserting optical insulators between them (trenches).

A third source of correlated noise are afterpulses. Afterpulses are caused by impurities in the lattice that introduce trapping states corresponding to energy level close to the valence and conduction band, so that free carrier can be trapped in these states and released after a certain time proportional to the state energy. These carriers can then trigger other avalanches and thus, afterpulses. They can also occur as a consequence of the generation of an electron-hole pair in the substrate by a

photon emitted during the avalanche that diffuses toward the substrate: if the generated carrier reaches the same microcellactive region by diffusion, a new avalanche is triggered and an afterpulse is produced (in DeCT, instead, the avalanche is produced in a different cell). This phenomenon is referred to as Diffusive Afterpulsing. The delay of afterpulse generation is usually less than 100 ns and the amplitude is always lower than the one of the primary pulse due to the fact that cell has not yet fully recharged [17].

Excess Noise Factor

In photodetectors with internal multiplication, like APDs and PMTs,the internal gain is obtained by a multiplication mechanism, which is a statistical process: it is characterized by a mean value, i.e. the nominal gain, and a variance. Gain fluctuations enhances the noise on the overall measurement as they add uncertainty in the measure, and the Excess Noise Factor (ENF) parameter is used to account for a fluctuation in the charge of the output signal. Silicon Photomultipliers, despite having an internal multiplication process, provide a highly uniform and quantized amount of charge in response to the absorption of a photon leading to ENF very close to unity and mainly limited by optical crosstalk and afterpulses.

2.3.4 NUV-HD SiPMs

On the market are available Silicon Photomultiplier from different manufacturers, including Hamamatsu and On Semiconductor (formerly SensL). However, the photodetectors that best fits the specifications of LINUS project are Near Ultraviolet High-Density (NUV-HD) SiPMs from Fondazione Bruno Kessler (FBK), located in Trento, Italy. In the current section will be described the main parameters and technological advantages offered by the aforementioned devices [18].

The first parameter to be considered in the choice of a Silicon Photomultiplier is the detection efficiency at the wavelength of interest. As LINUS project requires the readout of Pyrene fluorescence spectrum, char-

acterized peak emission wavelength of 375 nm, the coupled photodetector should be sensitive to photons with the same wavelength. In this way the signal is maximized, as on average a larger number of photons are effectively absorbed in the photodetector, as a result of a high PDE. Fondazione Bruno Kessler provides Near-Ultraviolet (NUV) SiPMs with a PDE peaking around 400 nm, reaching values as high as 40 % with V_{OV} = 6 V. Recently, the performances of NUV SiPMs have been improved thanks to the High Density (HD) technology, that allows the scaling of the microcells without losing detection efficiency because of are reduced fill factor. The interest in smaller microcells is due to significant performances enhancement that can be summarized as faster response, due to reduced depletion capacitance, higher dynamic range, since the number of microcell for a given area increase, and lower correlated noise [17].

In figure 2.23 is represented a $6mm \times 6mm$ NUV-HD SiPM with $30\mu m \times 30\mu m$ cell size, featuring a PDE of more than 50 % around 375 nm. The Breakdown Voltage (V_{BD}) for these SiPMs has been measured to be 26,6 V at room temperature (figure 2.24)

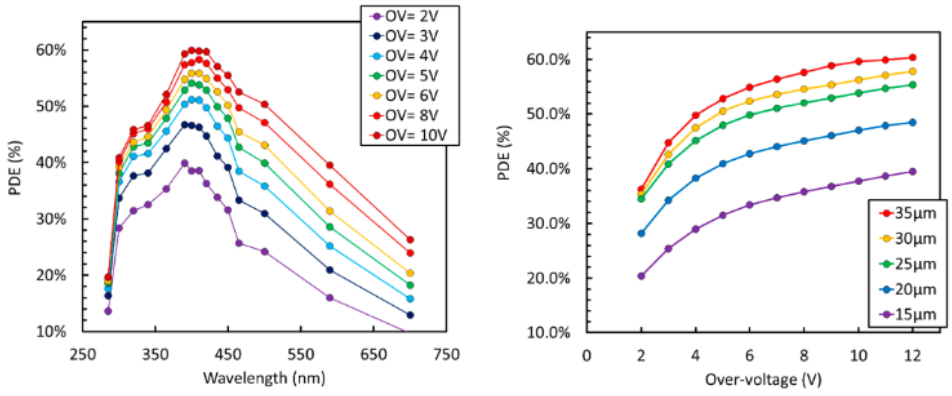

(a) PDE vs wavelength at different over-voltages

(b) PDE vs V_{OV} measured on different cell sizes

Figure 2.23: *Photon Detection Efficiency for the NUV-HD SiPMs.*

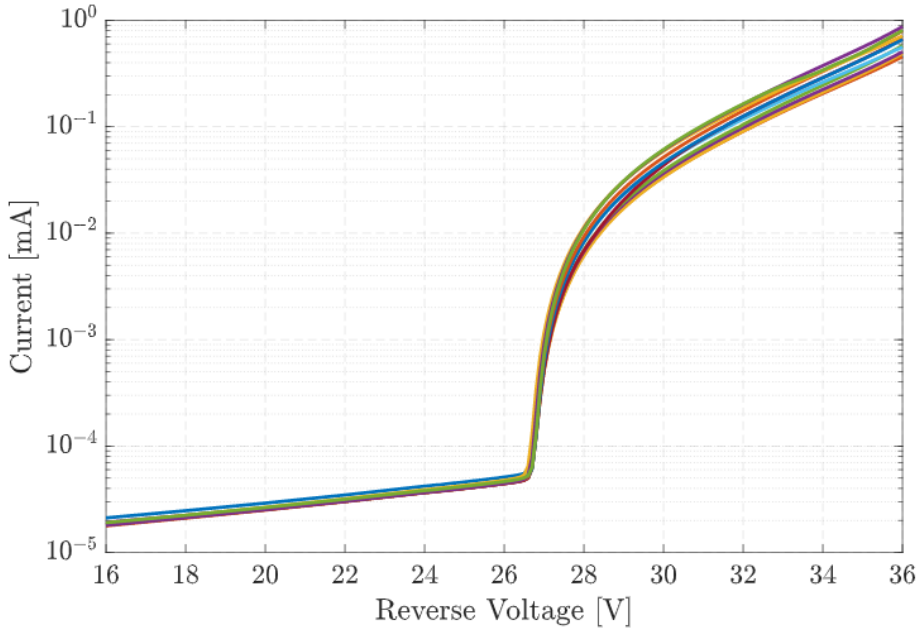

Figure 2.24: *I-V characteristic of a 4×4 NUV-HD SiPM tile.*

Chapter 3

System Architecture

This chapter presents the detection system structure, composed by a microfluidic channel prototype, one SiPM and one LED connected to Printed Circuit Board (PCB) where their driving circuits are placed. At the beginning, the SiPM voltage bias modulation circuit and LED pulsing circuit will be presented, subsequently the acquisition chain will be described along with a description of the microcontroller firmware required to manage the system. Final sections are devoted to power management and the channel design.

3.1 System Overview

The system, object of this thesis work, is a new prototype of spectrofluorometer, focused on the readout of small fluorescence signals coming from a fluorophore. Pyrene is chosen as sample analyte because its emission spectrum matches perfectly with the maximum detection efficiency region of NUV-HD SiPMs: in this way the signal is maximized, as on average a larger number of photons are effectively absorbed in the photodetector, as a result of a high PDE.

Water-diluted Pyrene molecules are contained in a microfluidic channel specially designed to increase the detection efficiency. The sample is illuminated by fast LED pulses and the fluorescence light is collected by the

SiPM. As mentioned in Chapter 1, in a standard spectrofluorometer the detector is placed 90° with respect to the source so that it is not directly affected by the light beam. This precaution is used to avoid the photodetector from being blinded by the photons incoming from the source and no longer being able to detect the weak light of the sample fluorescence. However, scattering due to solvent molecules may deviate some light rays towards the photodetector. Hence the need to place optical filters that allow only the wavelengths of the fluorophore to reach the sensor and cutoff the scattered light of the source.

In our design we use a LED to excite the sample, thus avoiding a primary filter needed to select the proper wavelength of excitation. Instead to remove the secondary filter before the photodetector, we need to create a system that performs the same cutting function on the wavelengths of the source. For this reason, we designed a circuit capable in modulating the SiPM voltage bias, so that the sensor is turned off while the source irradiates and it is turned on when the fluorophore emits light. In this way the shielding action, previously performed by the optical filter, is now realized by the sensor itself. Once the SiPM is fully turned on, it is ready to receive the fluorescence light. Each photon generates a small current that is processed by an electronic readout chain already tested and used in Gamma Spectroscopy project [17] [20].

The full system (Figure 3.1) features several components that can be grouped in three major building blocks that will be discussed in detail in the following sections:

- **SiPM voltage bias modulator**: this is the innovative part of the spectrofluorometer. Relatively, it is a simple circuit driven by a microcontroller which, through carefully designed delay lines, turns the detector on and off.

- **LED pulsing circuit**: this circuit is designed to drive a LED so that its pulses are perfectly synchronized with the SiPM modulator. The LED should turn off when the SiPM turns on. To achieve this synchronization, the pulsing circuit is also equipped with a delay

line controlled by the microcontroller.

- **Electronics readout chain and DAQ**: the first is a single GAMMA-8-channel ASIC that performs the charge-to-voltage conversion of the SiPMs signal current pulse, while the DAQ stage is performed by a 12-bit ADC embedded in the microcontroller.

- **Power management**: in this first Linus prototype, power comes from a bench power supply and through linear regulators all the useful voltages in the circuit are generated.

- **Micro-channel design**: the channel is made of resin with windows on all sides where to place LEDs and SiPM at 90 °. The windows are closed with PVC or PMMA slides which can transmit UV light.

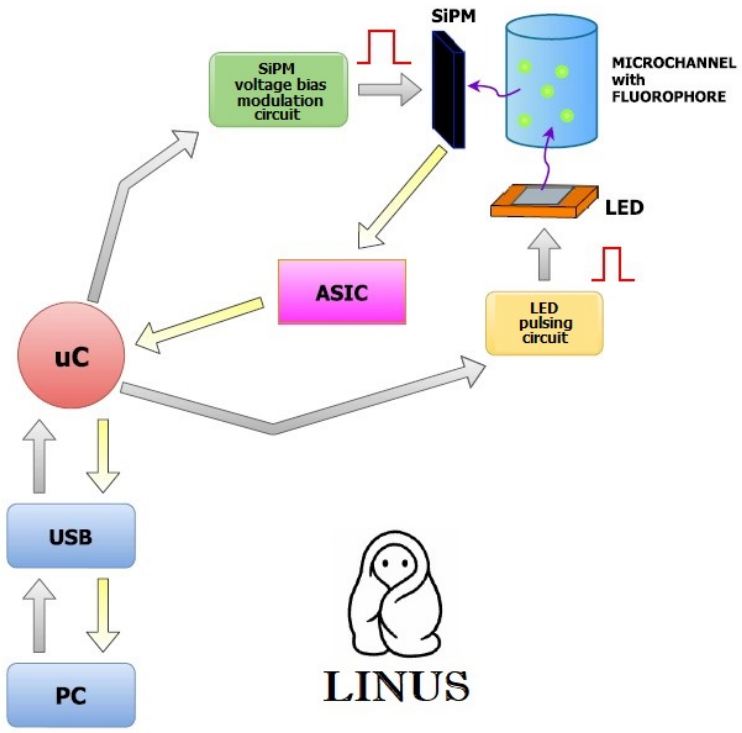

Figure 3.1: *Block scheme of LINUS system.*

3.2 SiPM voltage bias modulator

3.2.1 Theoretical design

In chapter 2 we see that the SiPM activates the avalanche effect after the breakdown voltage. Therefore, to perform the shielding effect, we can simply keep the SiPM bias voltage less than the breakdown voltage until the LED is on and then, when the light source drops, we increase the voltage instantly to activate the avalanche effect on the arrival of the fluorophore signal.

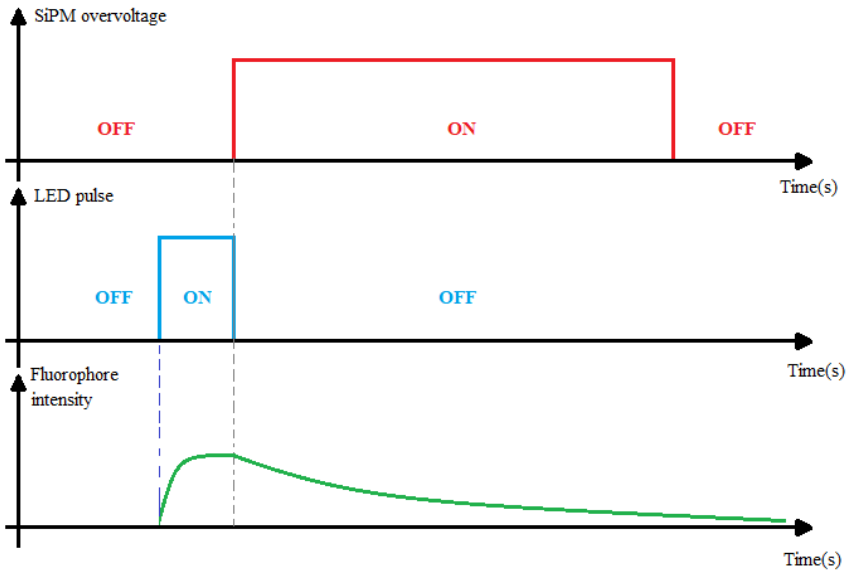

Figure 3.2: *Pictorical graph of SiPM modulation principle.*

The main problem with this implementation is the bias current required by the sensor to turn on and off. In fact, the SiPM needs a certain amount of current to be able to charge till the defined over voltage: if we think the detector as a capacitor, the amount of current depends on the value of its capacitance (generally between 0.6 nF and 3 nF depending on the SiPM size [18], [19]) and on the voltage difference to be applied in order to reach the desired gain. Considering the technology in use (shown in figure 3.4 and table 3.1), we can estimate a bias current in the order of hundreds of mA. This quantity is too high and cannot follow the same

path of the signal current generate by the fluorescence sample for two reason:

- The current generated by a photon on the SiPM is in the order of a few μA and it would be impossible to distinguish it above the bias current.
- The electronic readout circuit directly connected to the SiPM cannot support high current pulses.

Ideally the solution to this problematic is a double switching circuit (Figure 3.3).

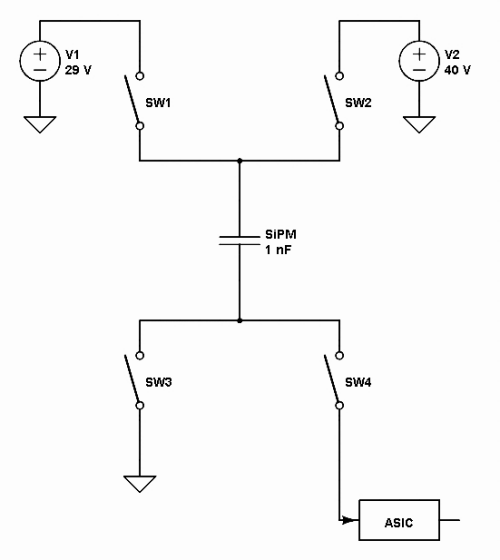

Figure 3.3: *Ideal switching circuit for SiPM modulation.*

To explain this concept, let's consider FBK NUV-HD SiPMs with High Fill Factor which will be use in the experimental phase. As shown in figure 3.4 and table 3.1, with an over voltage of 8 V (from 32 V, that is the breakdown voltage, to 40 V) the gain is high enough to guarantee a good PDE. Therefore, we choose for our starting design a bias voltage of 29 V (to be sure not to activate the avalanche) and an over voltage of 11 V, as to reach 40 V.

Table 3.1: NUV-HD-LF 15µm - HIGH FILL FACTOR

Voltage[V]	OV[V]	PDE	GAIN	ENF
34,0	2,0	0,205	2,99 10^5	1,22
35,0	3,0	0,274	4,13 10^5	1,13
36,0	4,0	0,322	5,19 10^5	1,15
37,0	5,0	0,348	6,23 10^5	1,15
38,0	6,0	0,377	7,14 10^5	1,14
39,0	7,0	0,380	8,20 10^5	1,17
40,0	8,0	0,411	9,11 10^5	1,19
41,0	9,0	0,414	1,00 10^6	1,29
42,0	10,0	0,424	1,10 10^6	1,26
43,0	11,0	0,438	1,20 10^6	1,31
44,0	12,0	0,447	1,28 10^6	1,33

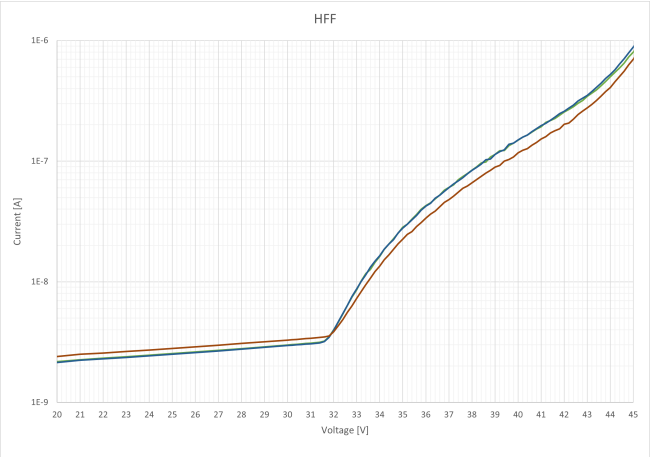

Figure 3.4: *Typical FBK NUV-HV SiPM with High Fill Factor, current vs over voltage graph [18].*

Following figure 3.5: in phase 0 the SiPM (simply model as a capacitor of 1nF) has a voltage bias less than the breakdown voltage because SW1 is closed to a voltage supply of 29 V and its cathode is closed to ground (SW2 closed). In this phase the LED is pulsing, while the SiPM is off (we are performing the shielding effect). When the LED pulse drops, the SiPM enters in phase 1 where SW1 opens and SW3 closes to a voltage supply of 40 V, thus the SiPM gets an over voltage of 11 V (in respect to 29 V) and starts the avalanche effect. SW2 is still closed (SW4 open) because the bias current must not flow in the ASIC channel. Finally in

phase 2, when the bias current is almost discharge to ground, the SiPM can acquire the fluorescence light and its current signal is addressed to ASIC thought SW4 closing (SW3 open).

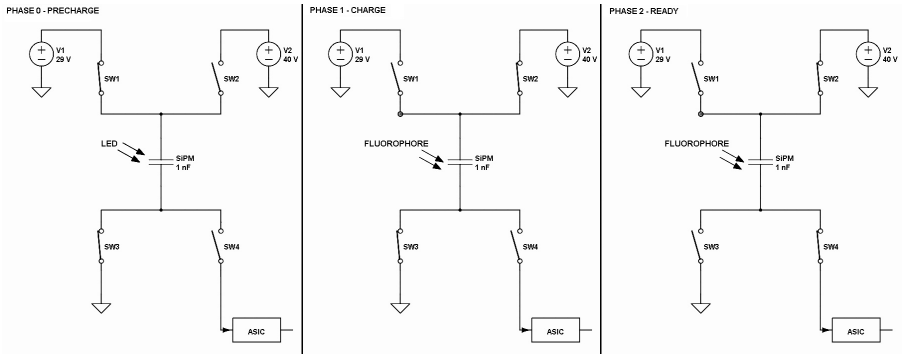

Figure 3.5: *Three switching phases in SiPM modulation.*

This is the reason why Pyrene is chosen as sample analyte: since we have to wait the activation of the last switch (SW4) to start collecting fluorescence current, we need a fluorophore with a long life time to still be bright when the acquisition takes place. Using other fluorophores with a life time of few nanoseconds, we would not be able to see the fluorescence, as the current generated in those first moments would be mixed with the bias current of the SiPM.

3.2.2 Real Circuit Design

In real applications switches are implemented by Mosfets. However, the bias switching (SW1 and SW2) can be easily performed using an AC coupling, thus avoiding major area occupation and costs (figure 3.6). Instead the switching between ground channel and ASIC channel is accomplished using two NMOS acting in antiphase. When the ground NMOS is on the ASIC NMOS is off and vice-versa, essentially performing a current steering.

However, after this first ideal design, we have to face the main problem: how to drive Mosfet gates and SiPM bias switching to be synchronous. The gate driving function is performed by an integrated circuit, named

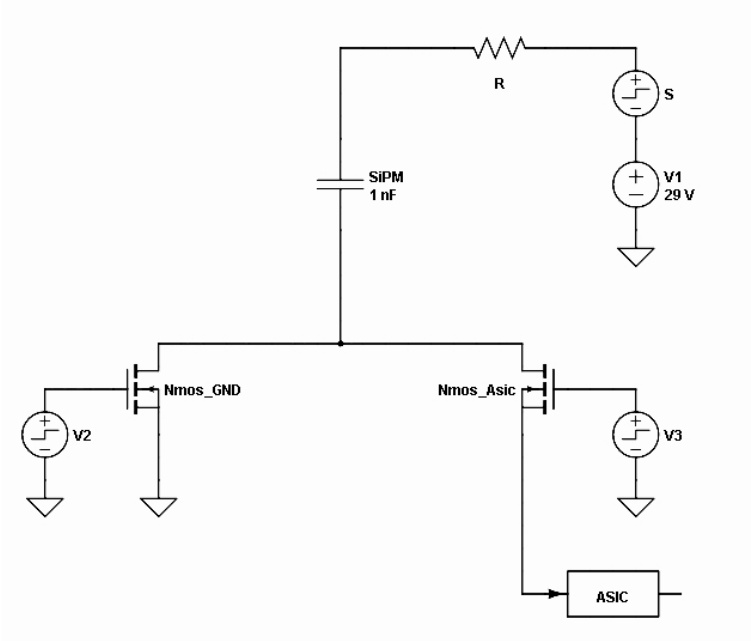

Figure 3.6: *Scheme current steering.*

gate driver, capable to switch rapidly from low voltage to high voltage. Its function consists in charging and discharging the gate capacitance to turn on and off Mosfets. As we see before, timing is fundamental in this application since we want fast switching to collect fluorescence light as much as possible. For this reason we choose the device from Texas Instrument "LM5134 Single 7.6 A Peak Current Low-Side Gate Driver With a PILOT Output" that presents 7.6 A and 4.5 A peak sink and source drive current for main output, 4 V to 12.6 V single power supply and switching times in the order of few nanoseconds [21]. At rest conditions, LM5134 output pin is fixed to low voltage (high voltage if we use the inverting output); when the input pin is pulled up (or down) by a signal, the device pulls up (or down) also the output pin till the voltage power supply, thanks to hysteresis. Therefore there are two benefits: first the output signal has very sharp edges (it is almost a rectangular pulse), secondly the device can provide a voltage amplification of the signal and high current (4.5 A and 7.6 A peak current) if needed to charge the gate capacitance. In conclusion, we can use a signal generated by a microcontroller (that has a

maximum voltage range of 3.3 V) as input signal for the LM5134 and at the output we will have an amplified signal to drive the gate capacitance.

NMOS threshold voltages are generally between 0.5 V and 1 V, so we set the power supply of the LM5134 at 5 V as high voltage (Mosfet on) and Ground as low voltage (Mosfet off). From the datasheet of the LM5134 we can estimate that, for a differential potential of 5V and load capacitance of 1 nF, the rise time and the fall time of the gate driving signals are around 5 ns. In figure 3.7 there is a schematic representation of the process described so far. Obviously, to exploit hysteresis effects, the voltage supply (or the signal dynamic range) has to be chosen accurately taking in to account logic input margins described in the datasheet.

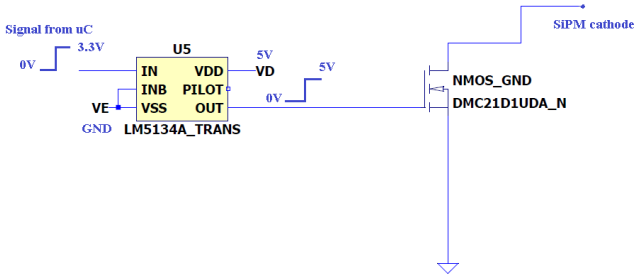

Figure 3.7: *PMIC and NMOS.*

This type of device, that from now on we will simply call PMIC (Power Management Integrated Circuit), is used also to implement the bias switching, instead of an AC coupling. As usual, if we think the SiPM as a capacitor, the principle is the same as before: we need high current and high voltage swing to perform the switching between the two bias references. If we send a signal from a microcontroller to an RC network (as represented in Figure 3.6), we don't have enough voltage range and current to turn on the SiPM. For this reason, we use the PMIC as voltage and current amplifier. The maximum power supply recommended in the datasheet is 12.6 V, so we can implement 11 V of over voltage putting 29 V as low power supply and 40 V as high power supply.

However, as we say before, we have to set properly the voltage signal range in respect to power supplies to exploit hysteresis. The input signal

coming from the microcontroller has to be shifted and amplified before entering the PMIC. To do that we use an CR network to shift the voltage range from 0 V - 3.3 V to 33 V - 36.3 V and than a voltage buffer with hysteresis to amplify the signal range up to 32 V - 37 V. Now the logic input margins of the PMIC are satisfied and the output signal swings from 29 V to 40 V (see Figure 3.8)

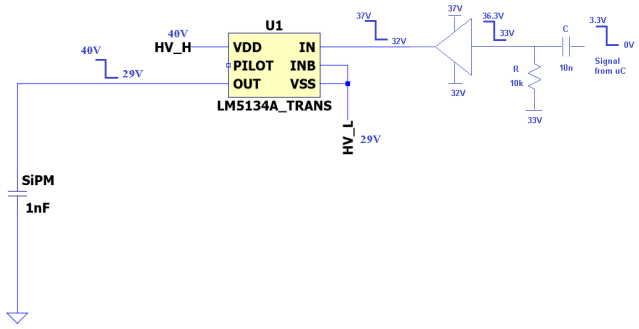

Figure 3.8: *PMIC and SiPM.*

Synchronisation is the most interesting challenge in the design. Figure 3.9 shows how NMOS gates and SiPM should be driven: when the SiPM turn on we need the NMOS of the ground channel still active to discharge the bias current to ground. Few nanoseconds after SiPM activation, the NMOS of ASIC channel must be turn on to acquire fluorescence signal and consequently the NMOS of ground channel must be turn off. There is a region of overlapping where both NMOS are active.

It is clear that signal windows have different time length and starting/stopping points. About this, there are two problems to deal with:

- Microcontrollers can switch pins between set and reset condition (1 or 0) at the clock frequency, i.e. the minimum rectangular signal has a duration of about 100 ns. This means that we cannot create directly from the microcontroller time window signals shorter then 100 ns.

- Since in microcontrollers instructions are executed every clock cycle, two signals can be delayed one in respect to the other only by 100 ns

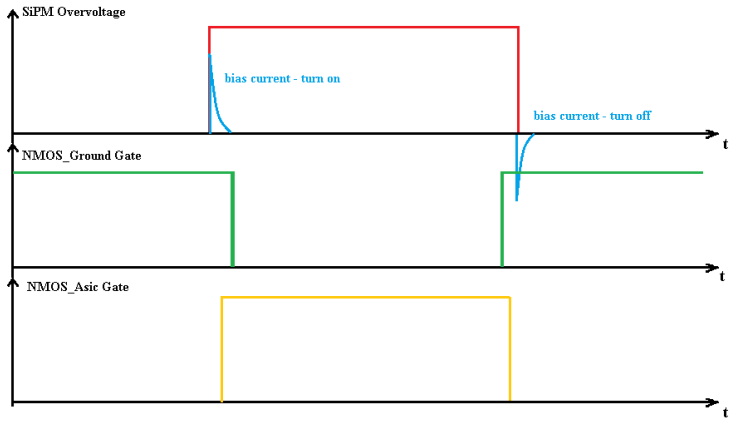

Figure 3.9: *SiPM and NMOS signals waveform.*

or more. This limitation make impossible to generate signals with few nanoseconds delay.

To summarize, using only a microcontroller it is not possible to synchronize signals driving the SiPM and NMOS gates as we want, since we may need delays in the order of dozens nanoseconds.

The solution to these issues is the introduction of logic gates and programmable delays. As represented in Figure 3.10, for the Boolean logic in AND gate the output is 1 only when both inputs are 1, while in NAND gate it is exactly the opposite, the output is 0 only when both inputs are 1.

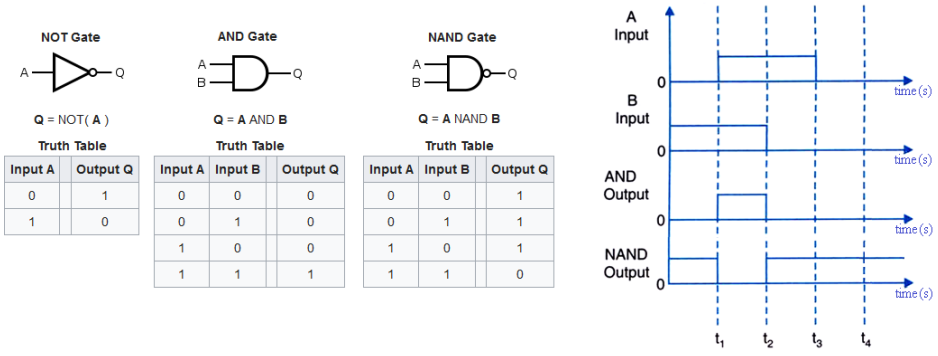

Figure 3.10: *AND and NAND logic gates.*

Following this logic, if we need to shift in time a signal by some mi-

croseconds in respect to a reference signal, we can use AND gate where the first input receives a signal started with the reference one, instead the second input receives a signal delayed by the time of the shift needed. On the contrary if we use a NAND gate with the same signals above, we obtain at the output a signal following the reference one till the second delayed signal arrives at the input. We can see an example in Figure 3.10, where input B follows an hypothetical reference (not represented in figure), while input A is delayed.

In this way it is possible to create time windows of any duration. In our case, if we want the same signals as in Figure 3.9, we just need two AND gates to implement signals driving SiPM voltage bias and NMOS gamma channel, while it is necessary a NAND gate to drive in the opposite way NMOS ground channel. In Figure 3.11 it is represented the combination of signals and logic gates.

Finally, we have also the advantage that a time window can be shifted or increased/reduced only changing the delay value, as reported in the example in Figure 3.12.

Obviously logic gates alone cannot solve the problem of the microcontroller maximum frequency: the minimum delay that we can generate is about 100 ns that is too long for our application where windows need to be delayed by few nanoseconds in respect to each other. That is the reason why we introduce a programmable delay line.

Programmable delays are devices used to slow down a signal by a time interval in an electrical network. There are two basic delay line technologies: passive and active. Passive delay lines or analog delay lines (ADL) are built with analog components and can delay both analog and digital signals; they attenuate the signal from input to output and use components such as capacitors and inductors. Active delay lines or digital delay lines (DDL) are built with digital components and are used to delay only digital signals. These lines do not attenuate the signal from input to output, but are characterized by a specific logic family: common logic families include transistor-transistor logic (TTL), complementary metal-oxide semiconductor (CMOS), and emitter-coupled logic (ECL). Specifications

for delay lines include delay line type, time delay, and rise time. Rise time is the time required for the pulse amplitude from one specified level to another. Time delay is the maximum delay in units of time that a delay line can provide. Finally, there are two basic delay line types: fixed and variable. Fixed delay lines can delay signals by a time interval set by the manufacturer. For fixed delay lines, the delay time is the only delay time that can be set. Variable delay lines can delay signals between two values in a specified range. Generally, the low end of the range is zero. For variable delay lines, the delay time is the upper value of a tapped or programmable delay range.

For our project we need a delay that can be adjust by different value and mostly it is necessary an high granularity between delay steps. Therefore we choose the programmable delay "DS1023" from Dallas Semiconductor [22] that is a programmable 8-Bit silicon delay line consists of an 8-bit, user-programmable CMOS silicon integrated circuit. Delay values, programmed using either the 3-wire serial port or the 8-bit parallel port, can be varied over 256 equal steps. The fastest model (DS1023-25) offers a maximum delay of 63.75 ns with an incremental delay of 0.25 ns, while the slowest model (DS1023-500) has a maximum delay of 1275 ns with an incremental delay of 5 ns. All models have an inherent (step-zero) delay of 15 ns. After the user-determined delay, the input logic state is reproduced at the output without inversion. For our application it is used "DS1023-100", with maximum delay of 255 ns and 1 ns of step size.

In conclusion, it is possible to generate all signals at the same time from the microcontroller and combine and delay them with logic gates and programmable delays. Next figure 3.13 is an example of the complete signal generation chain from the microcontroller to both NMOS gates.

Delay setting and signal synchronization will be explained in section 3.4.

3.3 LED pulsing circuit

Considering Pyrene excitation spectrum between 240 nm and 290 nm, we choose a "Deep UV LED CA3535 series (CUD7GF1B)" with peak emission wavelengths from 270 nm to 280 nm (figure 3.14).

LED driving circuit is designed so that a rapid pulse is generated with a falling edge coinciding with the rising edge of the SiPM over voltage. Fast pulses are necessary as first illuminated molecules do not waste all fluorescence light while the LED is still active. Considering that Pyrene has a life time of 200 ns, it is convenient to set pulses maximum duration to 50 ns.

Synchronization between signal edges can be achieved by using a delay line again. In this regard, it is decided to exploit the PWM mode of the programmable delay DS1023, capable of generating pulses with a minimum duration of 5 ns up to a maximum equal to the maximum value of the delay.

We have to place two programmable delays in cascade, the first with the function of delaying the signal, the second instead in PWM mode. As reported in DS1023 datasheet, PWM is an output triggered by the rising edge of the input waveform. After a time interval approximately equal to the Step Zero delay of the device (15 ns) the PWM output will go high and it will return to a low level after a time interval determined by the programmed values (example in figure 3.15).

This is an easy way to control the LED pulse falling edge and making it matched with the SiPM over voltage rising edge only by changing the delay value of the first programmable delay. It is also possible to adapt the pulse size by changing the value of the delay in the PWM mode.

3.4 Electronics readout chain and DAQ

3.4.1 ASIC

A custom 8-channel ASIC, namely "GAMMAv2" has been developed for Gamma Spectroscopy project [20] and used also for Linus project. Its main features are:

- **Current mode input stage** to deliver to the filter and to the trigger circuit a properly scaled current pulse.
- **Gated integrator filter** to integrate the current pulse coming from the current conveyor into a voltage signal, maximizing charge collection.
- **Automatically adjusted gain** thanks to double time threshold mechanism.
- **8 parallel output channels**.
- **Performance in target with the application requirements**: 84dB Dynamic Range and 3 nC Full Scale Range.

The overall ASIC block scheme is depicted in figure 3.16

Input stage

The input stage of the ASIC is based on 4-transistor Temes current buffer as shown in figure 3.17. It is a current mode input stage with positive feedback, which provides a low input impedance and allows large area detectors to be coupled to the ASIC without affecting circuit stability. The aim of this stage is to provide a fixed voltage bias for the input node, effectively read the current pulses, and deliver scaled replicas of the incoming pulses to the trigger circuit and to the filter through a current mirror. The stage is denoted as Current Conveyor. The incoming current pulse is scaled down with a scale factor programmable to 100 or 50, since, to integrate up to 33,6 mA of peak current, the required integration capacitance would be too large in terms of area constraints [17].

Adaptive Gain Integrator Filter

Aim of this stage is to integrate the attenuated current pulse coming from the Current Conveyor to produce an output voltage proportional to the input charge. The output voltage, for an exponential current pulse starting from t = 0 will be described by the relation:

$$V_{out} = \frac{Q}{C_f} = \frac{1}{C_f} \cdot \int_0^{\infty} i_{int}(t)dt = \frac{I_{in} \cdot \tau \cdot G_{cc}}{C_f} \tag{3.1}$$

For GAMMA ASIC a Gated Integrator structure has been chosen,represented in figure 3.18. This strategy has the advantage of not requiring a peak stretcher circuit, as the filter output voltage does not change up to the feedback capacitance reset.

The integration phase can be set in a wide range from 100 ns to 16 μs in order to integrate properly signals provided by fluorescence light. Considering a de-gain factor of the Current Conveyor of 100, the integration capacitance can be sized to 12 pF to fit the maximum current within the maximum voltage allowed by the integrator dynamic. However, such a capacitance will produce a voltage signal lower than 600 μV for a single photon signal, which could not be detected, being buried by the noise. In order to overcome these difficulties, an automatic gain control has been implemented. In this way it is possible to use a small feedback capacitance, that produce a significant voltage signal even in case of single photon signals, to which larger capacitances can be connected in parallel, reducing the gain in case of large incoming current pulses to avoid saturation effects and charge losses [17].

Adaptive Gain Control

An automatic gain control can be simply implemented as a threshold-based logic: the output voltage of the filter should be compared with a threshold and, as soon as the threshold is overcome, an additional capacitance can be connected in parallel by closing a switch to increase the amount of charge that can be integrated. Although this approach is very

simple and requires very little logic, it does not allow the exploitation of the full dynamic of the integrator, since the delay from the threshold crossing to the capacitance connection can cause the stage saturation in case the threshold is set too close to the supply voltage.GAMMA ASIC instead features an innovative predictive gain control that allows a better exploitation of the available voltage dynamic. The idea is to check the initial rise time of the filter output voltage, being proportional to the input current pulse peak. In case of very short rise time, peculiar of large input pulses, the largest available capacitance is connected, while in case of slow rise time, no capacitance will be added. The predictive gain control logic is represented in figure 3.19 [17].

3.4.2 Microcontroller

The microcontroller has to manage the ASIC programming, delay setting, SiPM and LED time windows synchronization and it has to perform the acquisition of the signals when a valid event is processed by the ASIC; to maintain a compact system it was also decided to convert the signals through the integrated ADC of the microcontroller. The acquired data need then to be sent via UART protocol the host PC. Taken into account these specification, the choice fell on a STM32F413RG microcontroller by STMicroelectronics based on the high-performance Arm®Cortex®-M4 32-bit RISC core operating at a frequency of up to100 MHz, in a LQFP64 (10 mm×10 mm) package and its main features are:

- 1,7 V to3,6 V power supply
- Up to 1,5MB of Flash memory
- 2x 12-bit Digital to Analog Converter (DAC)
- 1x 12-bit,2,4 MSPS ADC up to 16 channels
- General-purpose DMA
- 32-bit and 16-bit timers up to100 MHz

- Up to 24 communication interfaces including 5 SPI and 10 UART/USART

The microcontroller is operated at 72 MHz clock, which is not the maximum available clock frequency,but it is the choice that maximizes the ADC sampling frequency. Its programming and debugging is performed via ST-LINK/V2 debugger/programmer thanks to a dedicated 4-pin2, 54 mm header soldered on the board. The integrated ADC is a 12-bit Successive Approximation Register(SAR) ADC with an Effective Number of Bits (ENOB) of 10, 8 bit with 16 multiplexed external channels, performing conversions in the single-shot or scan mode and it can be operated at a frequency up to 36 MHz which is achieved with a system clock of 72 MHz. It has an integrated sample and hold circuit with channel-independent programmable hold time, and an input voltage dynamic that spans from ground to the analog supply voltage. The ADC conversion is started by a an external trigger signal, coming from the TRIGGER OUT channel of the ASIC, conveyed each time a signal is detected [17].

Microcontroller Firmware

The microcontroller firmware has been designed to operate on the digitalized data, to manage the data transmission, to program via SPI the ASIC, to set delay values and to start acquisition cycles. A block diagram of the main task implemented in the firmware is shown in figure 3.20.

The code for ASIC programming and data processing has already been implemented for the Gamma Spectroscopy project [17]. Taking advantage of this basis, we just add a new section in the finite state machine defined previously in Gamma code to program the delays and to start the acquisition cycles. As reported in figure 3.20, new programming and starting states are named **SET DELAY**, **SET NUMBER OF CYCLES** and **START CYCLES** respectively.

To set the delay, the DS1023 device is equipped with a serial input or 8 parallel inputs for programming. In the SERIAL programming mode, the output of the DS1023 will reproduce the logic state of the input after a delay time determined by an 8-bit value clocked into the serial port. While

observing data setup (t_{DSC}) and data hold (t_{DHC}) requirements, timing data is loaded in MSB-to-LSB order by the rising edge of the serial clock (CLK). The latch enable pin (LE) must be at a logic 1 to load or read the internal 8-bit input register, during which time the delay is determined by the last value activated. Data transfer ends and the new delay value is activated when latch enable (LE) returns to a logic 0 (figure 3.21).

Here a brief description of the new commands:

SET DELAY state: when the command "SETDELA0...0!" is received, the microcontroller copies the data from the command string into 8-bit arrays corresponding to each delay. Subsequently a timer is activated to synchronize bits acquisition according to the serial mode described above. At the end of the acquisition the timer is stopped.

SET NUMBER OF CYCLE state: when the command "CYCLE0...0!" is received, the microcontroller copies the data from the command string and transforms char values in a integer number. The number of cycles consists of the number of times the SiPM is switched on and off.

START CYCLES state: when this state is reached, using FOR function, instructions are executed and repeated for the selected number of cycles. These instructions consist in SET and RESET commands for the PINs connected to the SiPM and LED driving circuits.

Particular attention should be paid to the last state where the order in which SET and RESET commands are written affects the synchronization. As we have already said, every instruction is executed by the microcontroller at each clock cycle: this means that it is not possible to set all PINs to 1 (pull-up) or 0 (pull-down) simultaneously and to start all the signals at the same instant, but every signal will be delayed by 100 ns (execution time between one instruction and another dictated by the microcontroller) compared to the previous one. Therefore, an optimal order of execution must be established and combined with the delays in order to obtain signals in the desired positions.

In figure 3.22, on the right, there is an explanatory representation of the pull up commands (the pull down phase is not represented): the order of execution (from RED A to GREEN B) is the one indicated in the firmware. We can see, on bottom left, that signals marked with the letter "A" are those that go directly from the microcontroller to the logic gates, instead signals with the letter "B" are those that pass through the programmable delay before reaching logic gates. LED signal is just one because delay and PWM are generated on the same line. Each signal is delayed by a fixed time dictated by the microcontroller during instructions execution but, at the end, we need to program DELAYS to shift signals and reach the configuration represented on top left. By choosing delay values appropriately, it is possible to change time windows and to position the rising or falling edges of the signals in the desired point.

3.5 Power management

PCB voltages range from 40 V to -3 V. The reason of the presence of negative voltages is due to a voltage reference shift of the ASIC. Normally the ASIC has a high voltage bias of 5 V, while the low voltage bias is ground. With this supply range input channels as a reference voltage of 3 V. However, in LINUS project the ASIC input is at the output of a branch of the current steering. On one side, the NMOS source is connected directly to ground, so in order for everything to work correctly we must also have 0V at the NMOS source connected to the ASIC. For this reason the input reference voltage must be shifted from 3 V to 0 V, therefore the supply range must be changed from 0 V / 5 V to -3 V / 2 V.

In order for the microntroller to communicate correctly with the ASIC, we must also shift its bias voltages from 0 V / 3.3 V (typically) to -3 V and 0.3 V. In this way all signals coming from the microcontroller have a voltage range between -3 V and 0.3 V, thus CR networks are needed to perform AC couplings and move signals to match the input ranges of the various devices. In figure 3.23 there is a schematic and simplistic representations of the main devices in SiPM voltage bias modulation circuit. Let's

first consider NMOS branches: a signal coming from the microcontroller passes through a CR network that shift it from -3 V / 0.3 V to 0 V / 3.3 V; subsequently it cross the delay, powered between 0 and 5 V, but at the output it still have a range of 0V/3.3V because delays have not hysteresis. Then there is the logic gate, also powered between 0 and 5 V, and the output signal is amplified from 0 / 3.3 V to 0 V / 5V thanks to hysteresis. Finally, the last block chain is the PMIC driving the NMOS gate capacitance as described in section 3.2.2 and figure 3.7.

Regarding SiPM driving chain, blocks are the same as NMOS but with different voltages: CR network shift microcontroller signal from -3 V / 0.3 V to 33 V / 36.3 V (in delay branch there is a CR shift to 0 V / 3.3 V before the delay, that works between 0 V and 5 V, and then the CR shift to 33 V / 36.3 V); then signal arrives at the logic gate powered between 32 V and 37 V, thus the output signal entering PMIC satisfies its hysteresis margins. As we saw in section 3.2.2 and figure 3.8, PMIC amplifies the signal range from 32 V / 37 V to 29 V / 40 V to drive SiPM switching on and off.

Needing high voltages and currents to drive the SiPM as fast as possible, we decided, for this first LINUS prototype, to use a bench generator to supply the main voltages. "RIGOL DP831A" is a power supply with two outputs from 0 V to 30 V (with one terminal in common) and one output between 0 V and 8 V. From this generator we take the voltages of 40 V, 29 V and -3 V, while we generate all the others with linear regulators.

Voltages of 32 V, 33 V and 37 V are obtained with the devices "LT3065" of Linear Technology that presents input voltage range from 1.6 V to 45 V, adjustable output voltage range from 0.6 V to 40 V and maximum output current of 500 mA. Since this voltages are needed only to supply the logic gate and CR networks, the power dissipated by the regulators is minimal.

The other voltages (5 V, 2 V and 0.3 V) are the critical ones to generate because they supply almost all components of the circuit. The total current required, considering the power consumption of all devices, is in the order of hundreds of mA. The linear regulator chosen is "LT3088" de-

vice of Linear Technology with input voltage range from 1.2 V to 36 V, adjustable output voltage to any level between zero and 34.5 V and maximum output current of 800 mA. We have to evaluate the power dissipation in order to calculate the junction temperature that must not exceed 150°C for a correct functioning of the device (from datasheet [23]).

The equation $P_{TOTAL} = (V_{IN} - V_{OUT}) \cdot (I_{OUT})$ on power dissipation, where V_{IN} and V_{OUT} are respectively the input and output voltages of the regulator and I_{OUT} is the output current, and the equation $T_J = T_A + P_{TOTAL} \cdot \theta_{JA}$ on junction temperature, where T_A is the ambient temperature and θ_{JA} is the thermal resistance (values are listed in a table on datasheet), are used for the calculation. If we suppose a maximum junction temperature of 100 °C, we obtain a maximum power dissipation of 2 W. For a DC current consumption around 300 mA, we can estimate a maximum input-output voltage drop of 4 V/ 5 V. The lowest voltage available from the bench power supply is 29 V. If we use only one linear regulator (for example to generate 5 V from 29 V) or few of them, the power dissipated is too high (3 W /4 W) to be supported by the device. The best solution is a linear regulator chain of nine devices where the starting voltage is 29 V and the last one 0.3 V, making only voltage drops of 3 V / 4 V per device. Thus the power dissipated is distributed over all of them and the single linear regulator consumes less then 0.5 W.

3.6 Microfluidic channel design

Usually, in spectrofluorimetry experiments, diluted fluorophore samples are contained in a test tube made of a material totally transmitting at the excitation and emission wavelengths of the analyte and the detector. In our project the wavelengths of interest are in the UV spectrum, so a typical vessel that may be suitable is a quartz cuvette. Quartz is certainly the best material to use in UV measurements because it has a transmittance of 90% throughout all the ultraviolet spectrum [24]. However, the cost and fragility of this type of cuvette led us to think of a more economical and also more efficient solution.

In figure 3.24 there are other types of material with good UV transmittance.

We designed a microfluidic channel prototype that can be simply printed in an available and inexpensive material with a 3D printer, such as resin. This device is used for static measurement, but the perspective is to draw a channel for moving fluids, with the aim of increasing the throughput. The channel has insertion slots for thin sheets (1 mm thick) of transparent UV material, to be chosen for example among those indicated in the figure 3.24. In this way we have two advantages: first, costs are reduced and the channel is robust, manageable and easily reproducible. Slides can also be removed and cleaned after each test. Secondly, we can change the material of the slide to find which one best meets our specifications.

In figure 3.25 it is represented a 3D model of the microfluidic channel prototype. There are insertion slots on all four sides in order to use two LEDs and two SiPMs. SiPMs will be positioned on the longer sides, while LEDs on the shorter ones, so that they are at 90 ° with respect to each other. At the top there are holes for the insertion of supports with the task of lifting the structure from the PCB. Finally the channel will be sealed with a stopper of the same material as the channel.

For our starting test we decided to use PVC windows. As shown in figure 3.24 on the right, PVC has excellent transmittance (at least 80 %) starting from wavelengths of 300 nm. In the previous chapters we said that the LED was chosen with emission peak at 275 nm, while the wavelengths that maximize the NUV-HD SiPM PDE are those in the range from 350 nm to 450 nm (in fact the Pyrene has emission peaks between 370 nm and 400 nm). Therefore the PVC slide cannot be placed in front of the LED because the light transmission would be null. However, the transmittance spectrum of PVC perfectly matches the detection region of the SiPM. We can therefore use the PVC slide only in front of the SiPM to have a double advantage: the fluorescent light passes through the PVC with low attenuation, while the LED light is shielded. This solution allows to relax the constraints on the switching timing between LED and SiPM.

Finally, the LED has already a thin quartz glass integrated into the

case covering the diode. Thus we just need to create a hole in the PVC slide where to fit the LED avoiding the PVC shielding on light emission.

Here there is a picture (figure 3.26) of the 3D printed channel:

3.7 PCB implementation

A 4-layer PCB was designed to accommodate the driving networks of LEDs and SiPMs, the voltage regulators and the reading electronics. As shown in figure 3.27, on the top layer we can find the electronics readout circuit with ASIC and microcontroller (RED circles), the USB slot to communicate from and to PC with the microcontroller (GREEN rectangle), a linear regulators chain that supply power to microcontroller and ASIC (YELLOW polygon) and finally the channel site (BLUE rectangle) composed by holes where to place connectors for SiPMs and LEDs and the channel.

In figure 3.28 is shown the bottom layer: in the GREEN rectangle there is the USB communication chain, in the RED circle we can find the LED pulsing circuit with the two delays clearly visible, in BLUE the bottom of the channel site, in the YELLOW rectangle we can see an another regulators chain that supply power to the delays and all the other devices on the bottom layer. Finally in the centre (ORANGE circle) there is the SiPM voltage bias modulation circuit composed by delays, logic gates and MOSFET.

Below are shown the pictures (figure 3.29 and 3.30) of the real LINUS PCB.

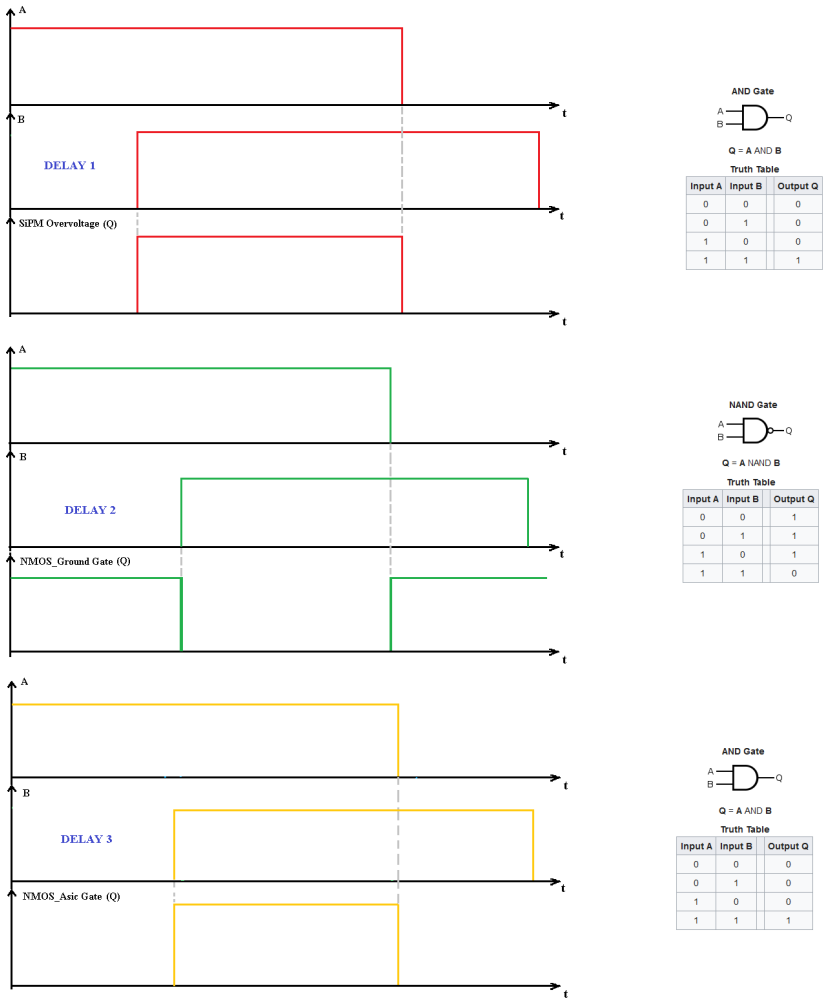

Figure 3.11: *AND-NAND gate signals waveform for SiPM and NMOS driving.*

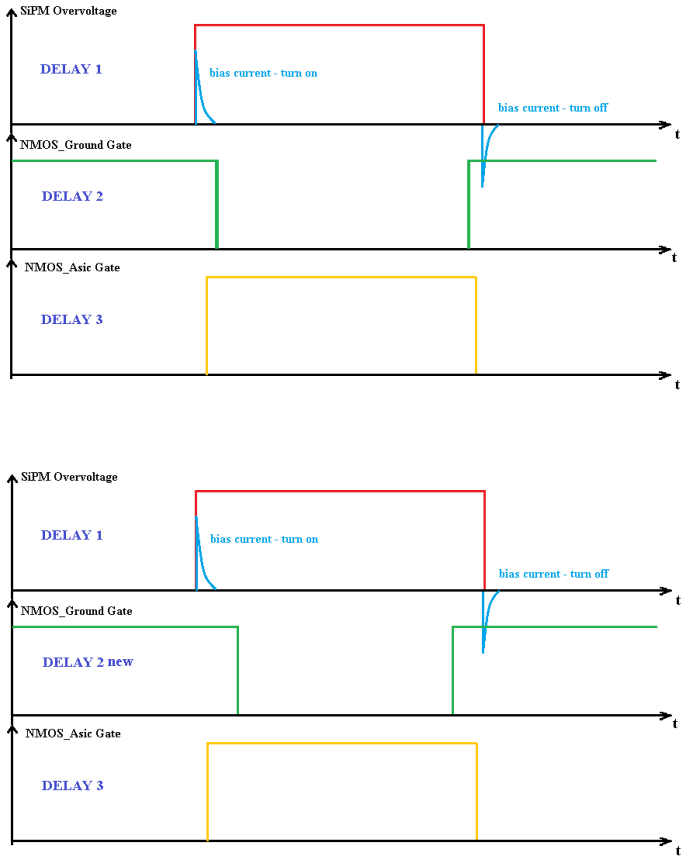

Figure 3.12: *SiPM and NMOS signals waveform with delays.*

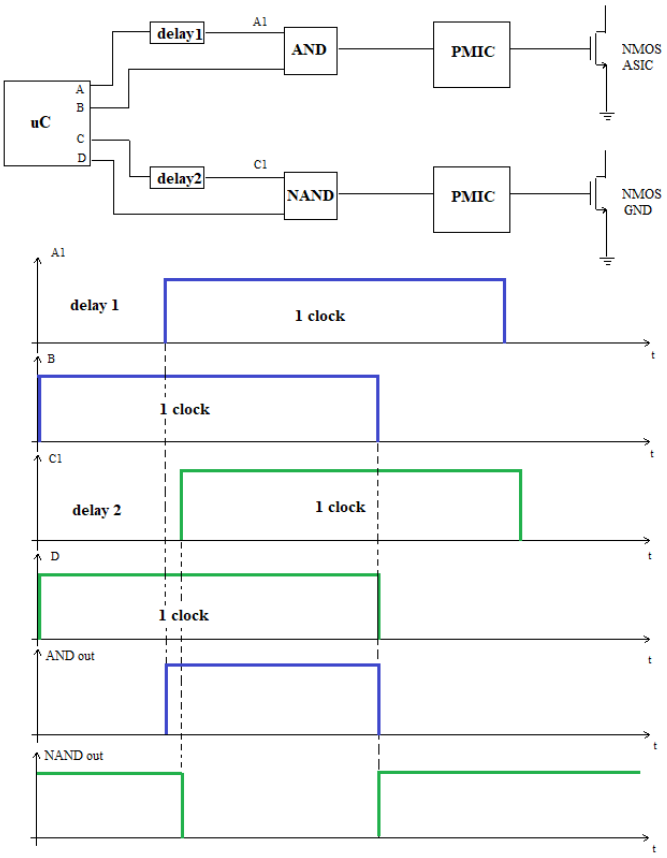

Figure 3.13: *EXAMPLE: microcontroller signals generation and delay settings.*

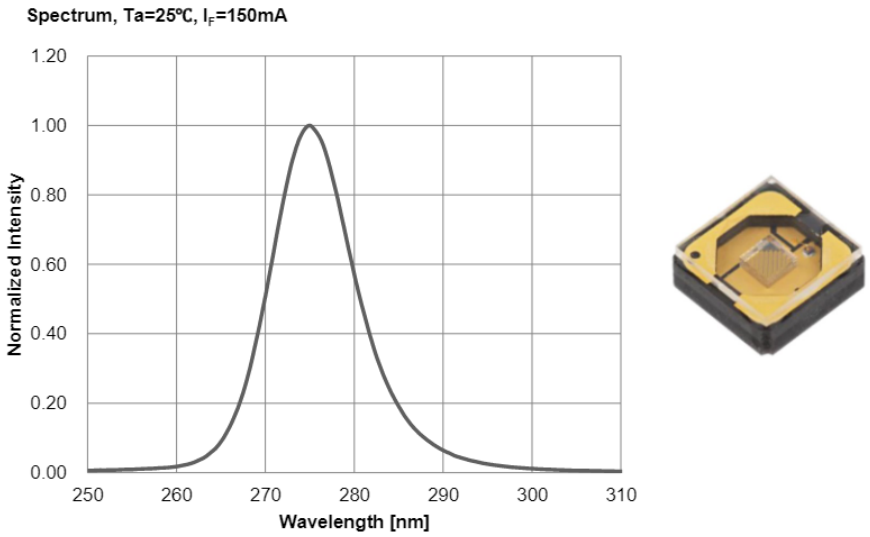

Figure 3.14: *LED spectrum.*

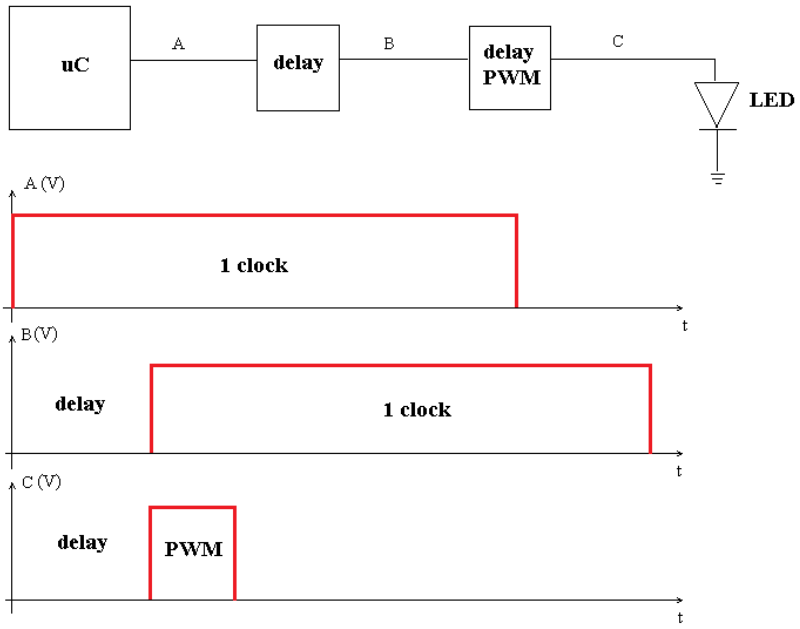

Figure 3.15: *LED chain control.*

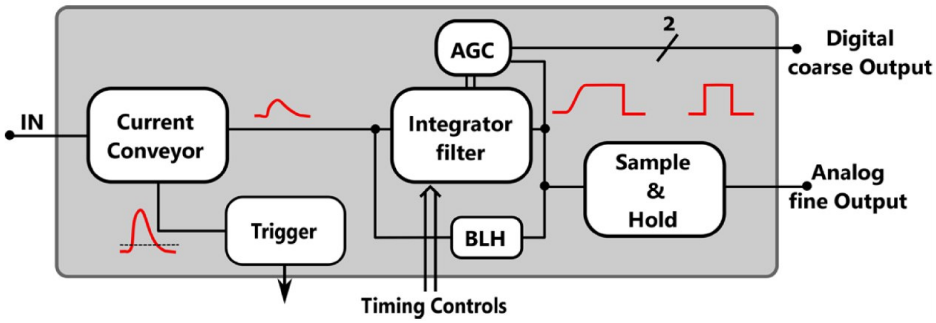

Figure 3.16: *Structure of GAMMA ASIC with 8 parallel channels.*

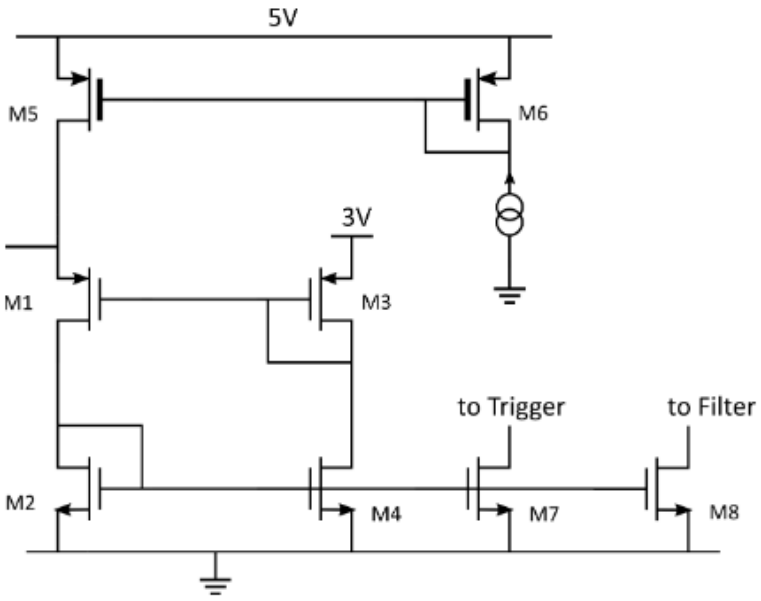

Figure 3.17: *GAMMA ASIC current conveyor.*

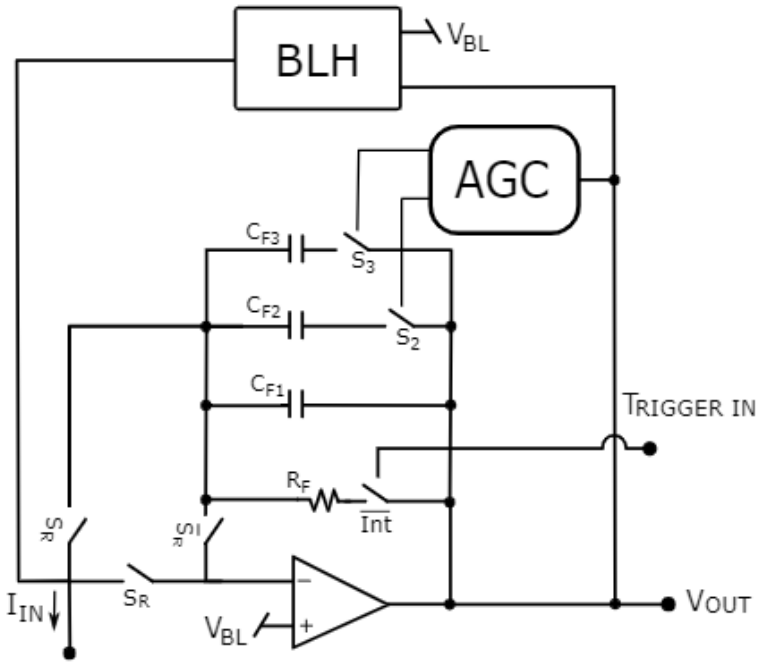

Figure 3.18: *Scheme of the GAMMA ASIC gated integrator filter with Adaptive GainControl. The baseline holder fixes the filter output baseline voltage by means of a negativefeedback loop subtracting the DC bias current at the filter input.*

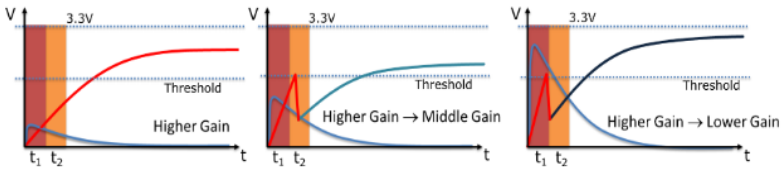

Figure 3.19: *Graphical representation of the time-based automatic gain control logic.*

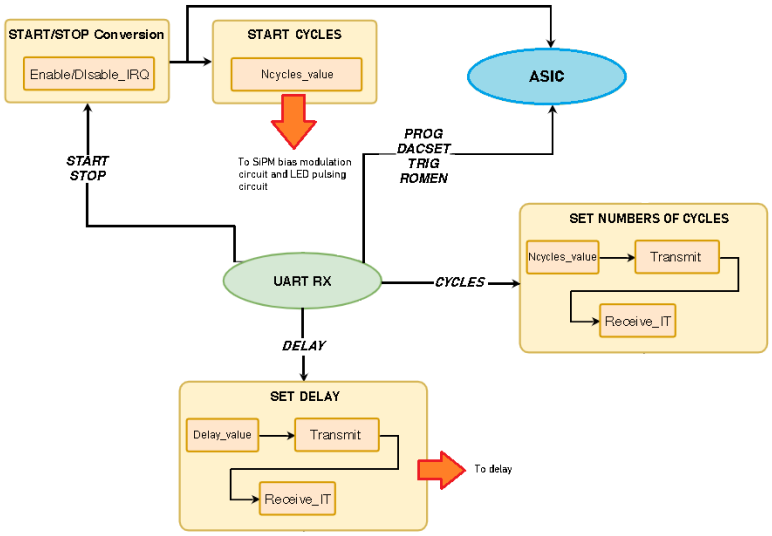

Figure 3.20: *Block diagram of the firmware implemented into the microcontroller: the main tasks are depicted.*

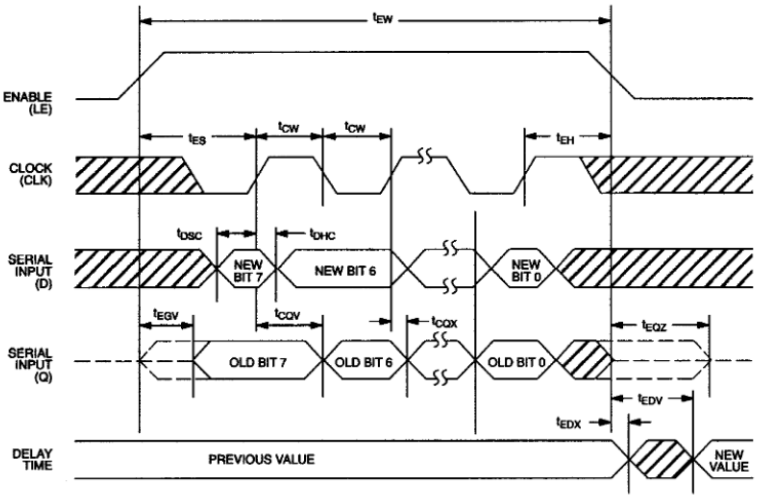

Figure 3.21: *Time diagram: SERIAL MODE delay programming.*

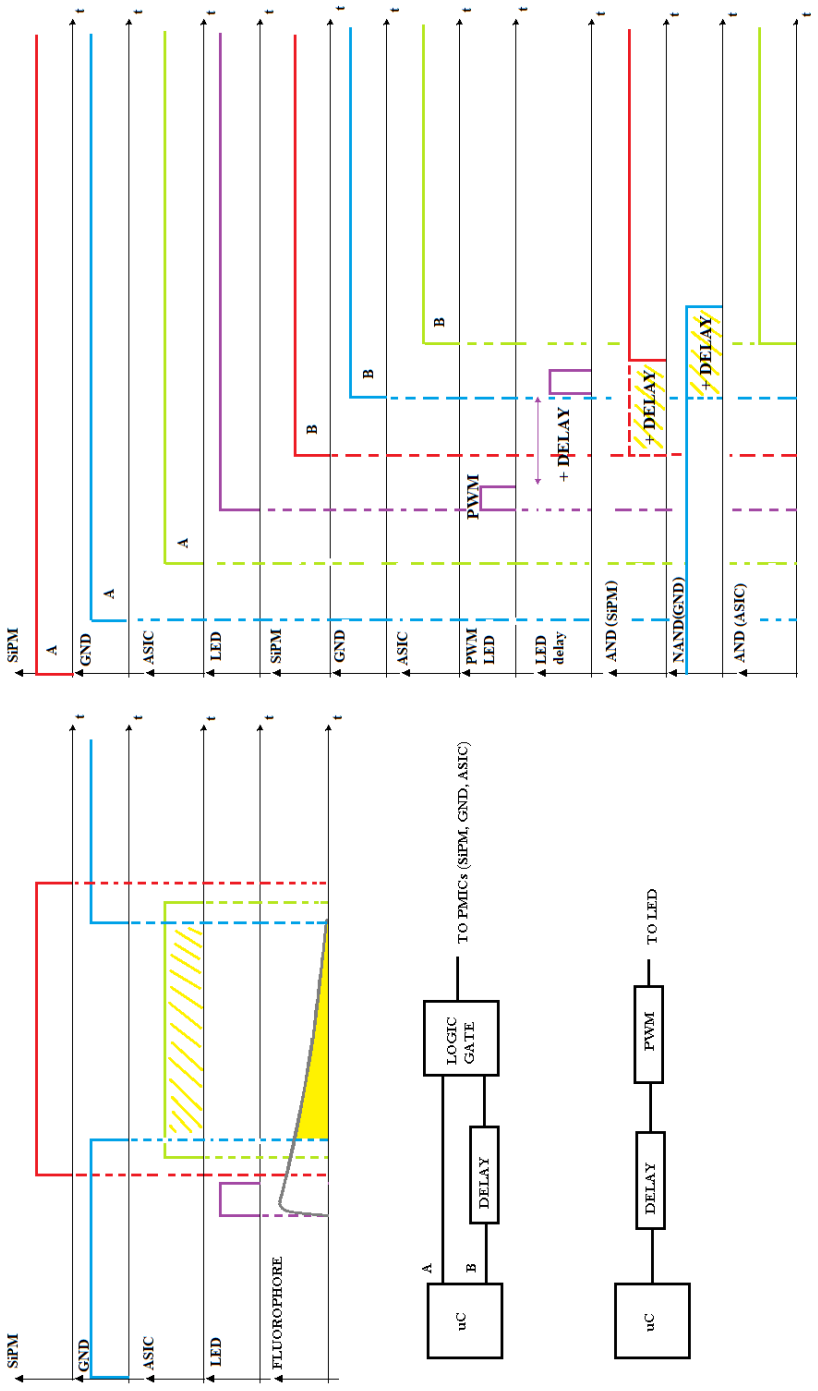

Figure 3.22: *Signals pull-up following microcontroller instructions.*

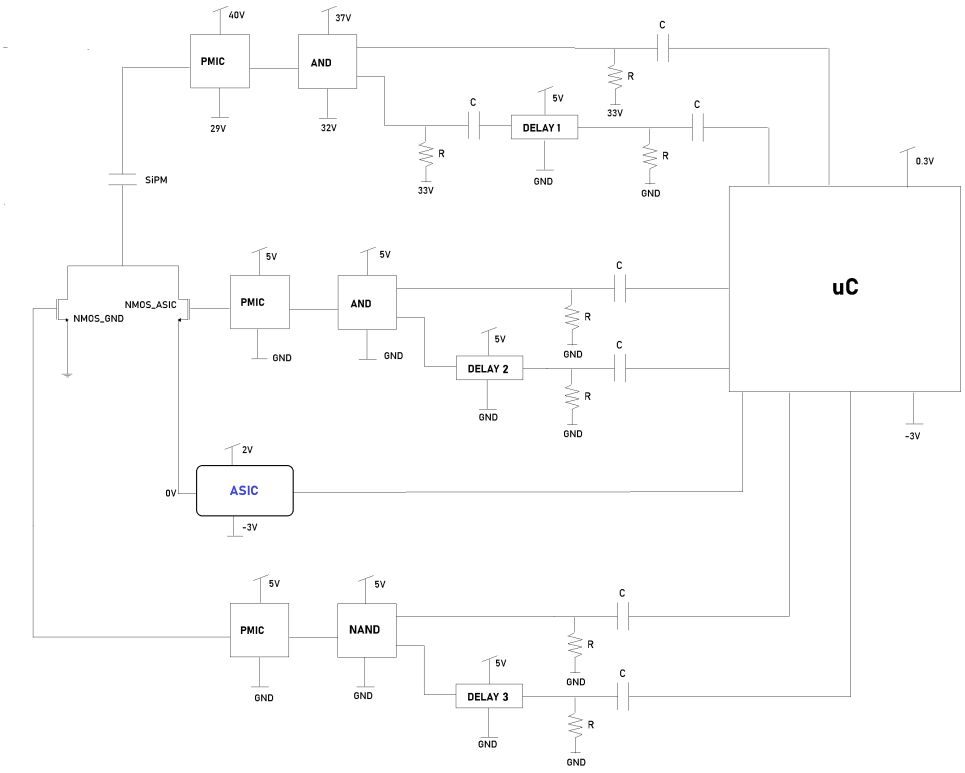

Figure 3.23: *Block chain of SiPM driving circuit with all voltage supplies.*

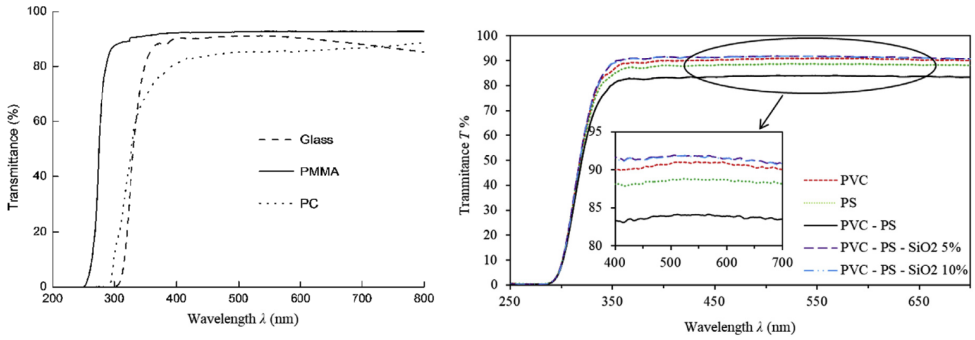

Figure 3.24: *PMMA, PC, PS, PVC and other materials transmittance graph [25], [26].*

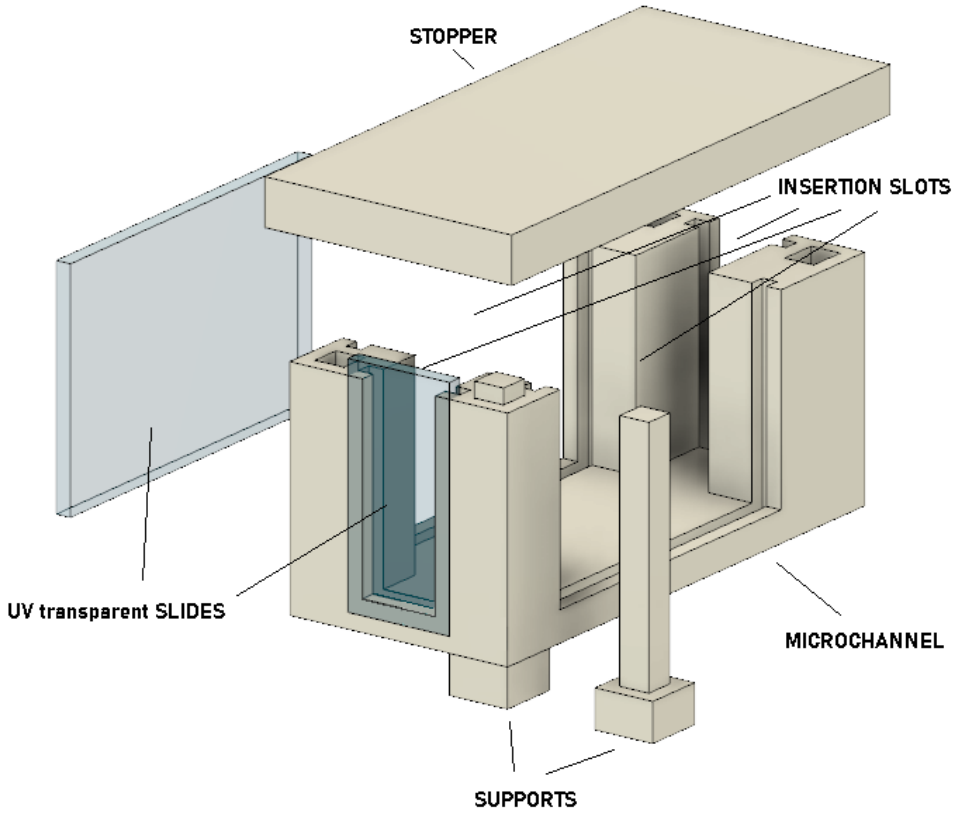

Figure 3.25: *3D model of the microfluidic channel prototype designed with Fusion 360.*

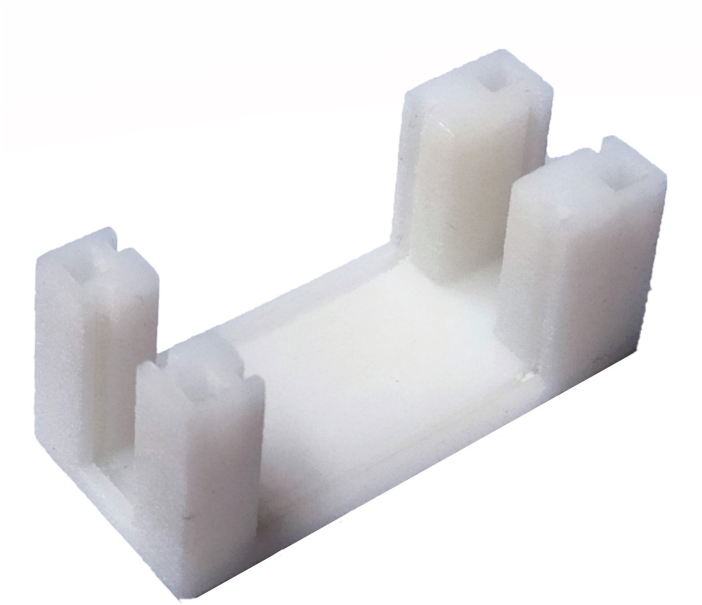

Figure 3.26: *3D printed channel.*

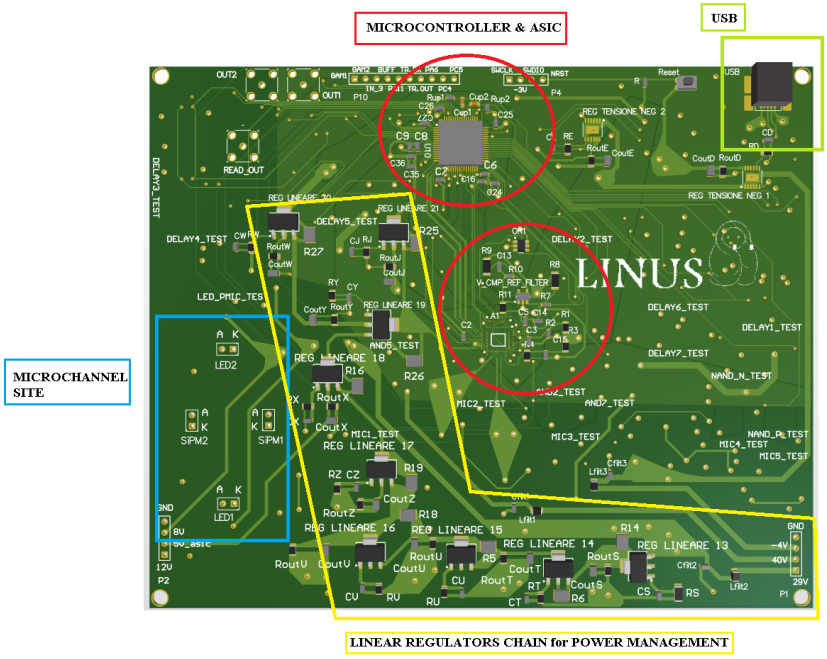

Figure 3.27: *3D model of the PCB, top view.*

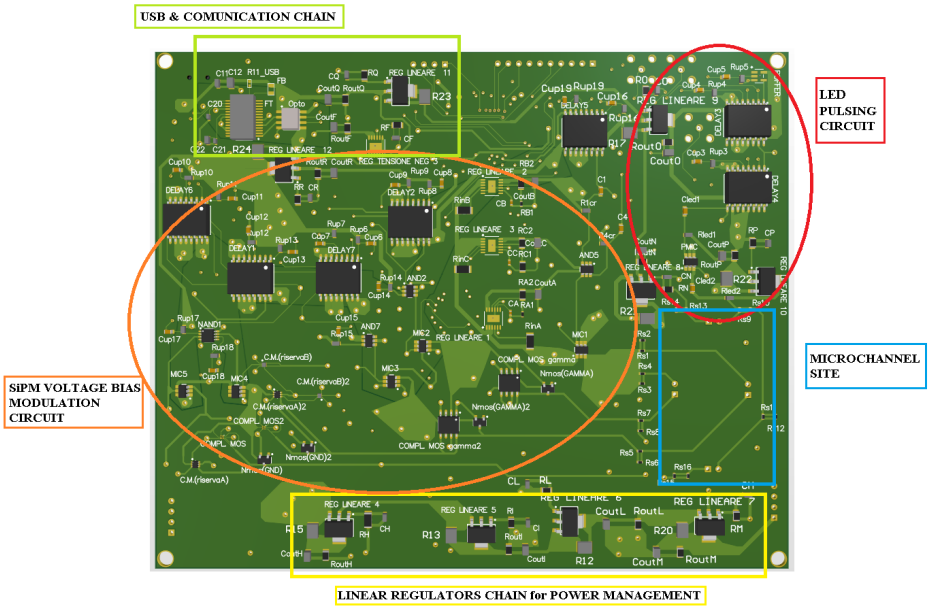

Figure 3.28: *3D model of the PCB, bottom view.*

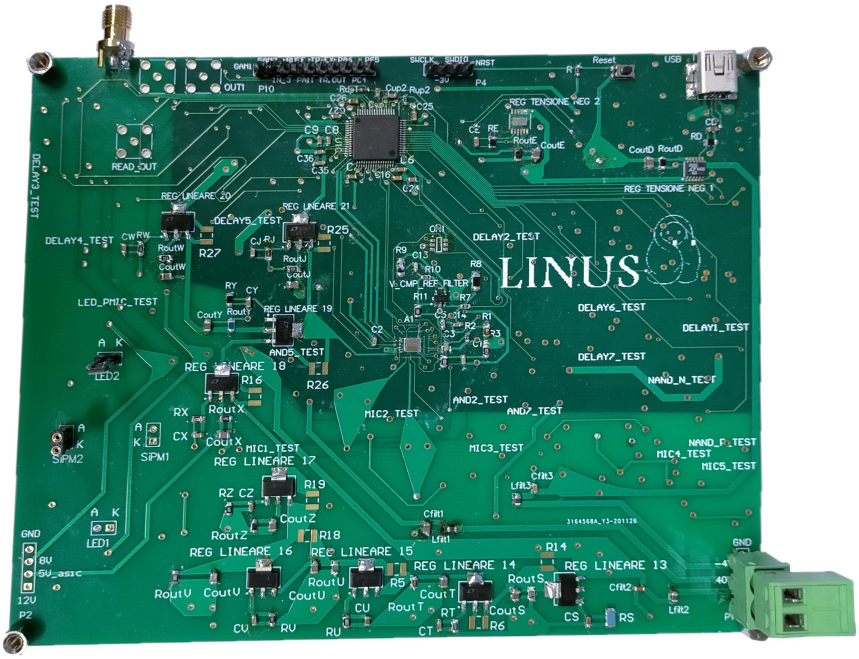

Figure 3.29: *LINUS PCB, top view.*

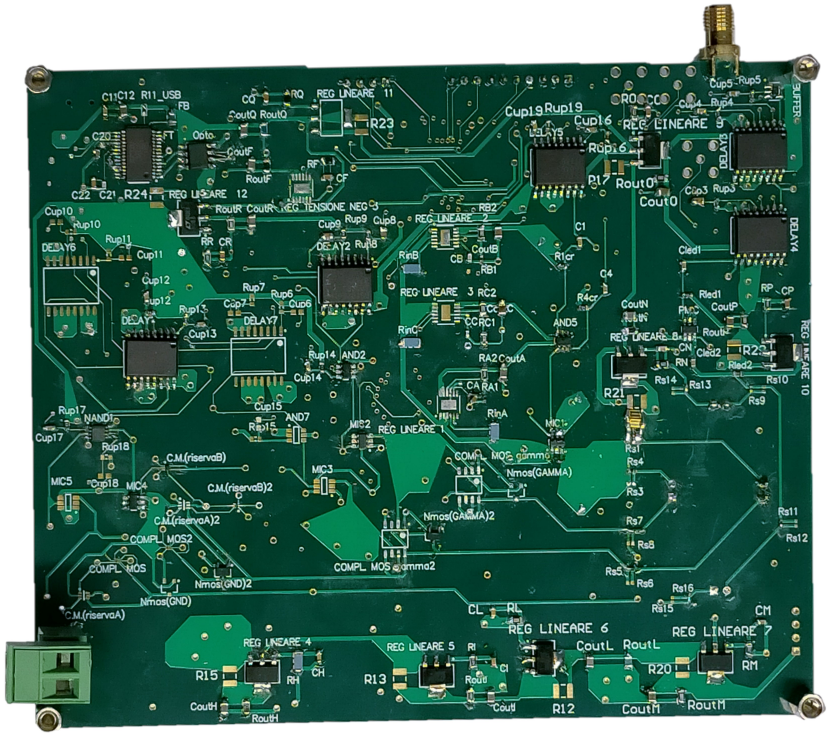

Figure 3.30: *LINUS PCB, bottom view.*

Chapter 4

Circuit Simulations and Experimental Measurement

This chapter presents a first part in which circuit simulations with LTSpice are described. The second part deals about real experiment measurements.

4.1 Circuit simulations

Both driving circuits were tested with a circuit simulator (LTSpice) before the real implementation on PCB. In particular, the simulations are used to choose the two Mosfets of the current steering, to set an ideal starting value for the delays and to evaluate the influence of parasitism.

As we said in chapter 3, the fundamental issue with the SiPM voltage modulator is the bias current which charges the photodetector. To divert this current away from the ASIC, we have implemented a current steering where two NMOS act in anti-phase between two channels, one towards ground and one towards the ASIC. The NMOS of the ground channel must be active on the bias current to discharge it to ground, while the NMOS of the ASIC channel must be turned on subsequently to acquire the signal current. Specifically, the NMOS of the ground channel has to support currents in the order of dozens or hundreds of mA, while the NMOS of the ASIC channel has to sustain much smaller currents due to

fluorescence light (in the order of a few mA). Therefore it is reasonable to choose a more powerful NMOS for the ground channel and a weaker NMOS for the ASIC one.

After this first discrimination, two other factors must be taken into account:

- MOSFETs present injection currents through parasitic capacitances during the turn on and turn off. These currents are inevitable and they increase as the gate capacitance increase (bigger MOSFET implies bigger capacitance).

- The bias current charging and discharging the SiPM is not a spike, but it has an exponential decay with a time constant in the order of dozens of nanoseconds depending on the SiPM size. When the ground channel NMOS is switched off, the exponential residual current flows in the ASIC channel.

We can conclude that it is impossible to have a totally free current channel on the ASIC side, therefore aim of simulations is to find an optimal solution to guarantee the lowest "spurious current" or "offset current" in the ASIC channel without loose current signal.

In next sections some simulations are presented: the circuit used is the one shown in figure 4.1.

The SiPM is represented by the equivalent electric cell that replicates its behavior: a capacitance of 0.6 nF is the model for a 1 mm x 1 mm SiPM with 30 μm of cell size. For PMICs and logic gates, the software is able to create realistic models according to the specifications provided by the manufacturer, while for delays and the microcontroller it is not possible to create a reliable model as the information needed by the program are not available. Therefore, to simulate the operations of these devices, we insert into the circuit some rectangular signal generators with a time size that can be adjusted by the user. For the sake of simplicity the ASIC is represented as a 20 Ω resistor. Finally, inductors are added before and after the SiPM to mimic wires inductance in the connection between

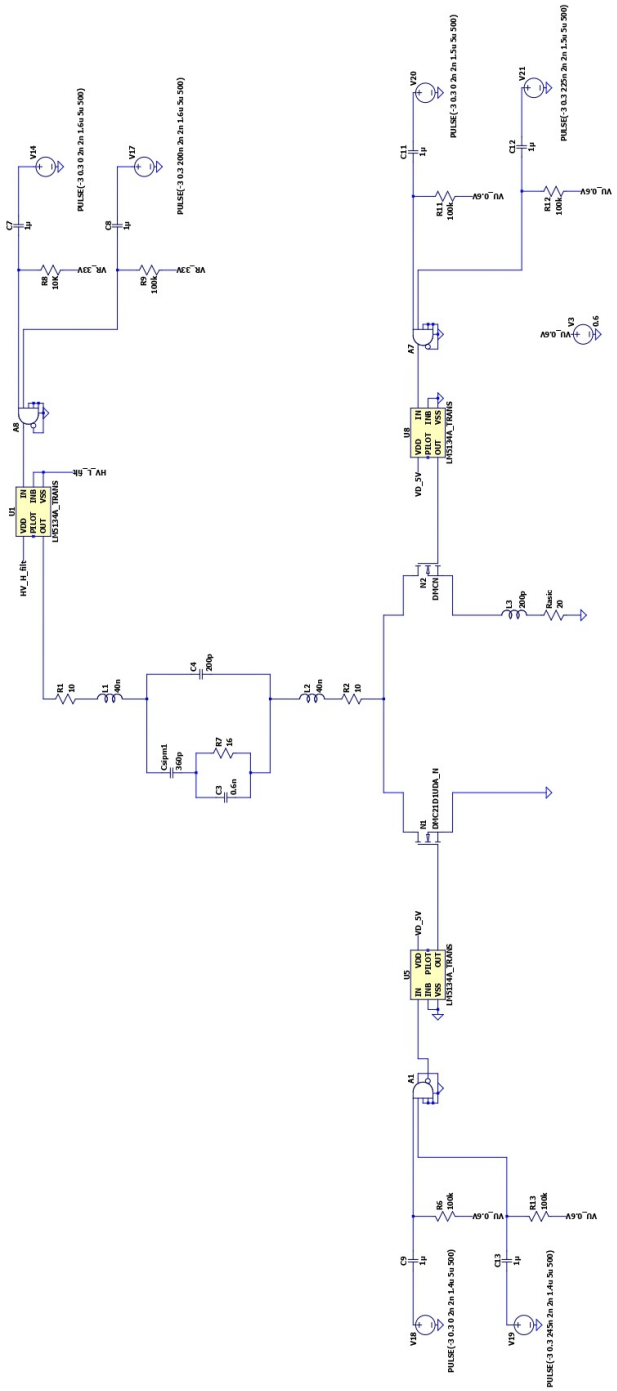

Figure 4.1: *Circuit model for simulation.*

photodetector and PCB. For this reason there are placed also resistors to mitigate inductance effects.

Simulation 1 will report an evaluation of some devices performance for Mosfet selection. In simulation 2 we will treat about delay settings and how the offset current changes with respect to delay selection. Finally the choice of resistors value in function of inductance variation will be discuss in simulation 3. In conclusion, simulation 4 deals about LED pulsing circuit parasitism.

4.1.1 Simulation 1: choice of the most efficient NMOS pair

Initial specifications

In this test we conduct a first simulation using two NMOS with similar characteristics and subsequently we will show two more simulations with better results due to an optimized choice of NMOS pairs.

Let's start setting the switching delay of the two channels. We suppose for example that the NMOS of the ASIC channel turns on 30 ns after the SiPM switching on and the NMOS of the ground channel turns off 60 ns after the SiPM switching on (i.e. 30 ns after the turn on of the ASIC channel NMOS). This overlapping region of the two NMOS (both switched on) is necessary to ensure that part of the injection current due to the switching on of the ASIC NMOS is directed towards ground. With these settled specifications, we can interchange the NMOS pairs to evaluate their behavior under the same conditions. In figure 4.2 are reported the waveforms of SiPM voltage modulating circuit obtained by the simulation circuit showed above in figure 4.1.

Results and consideration

Next figures are the result of three different simulations. In GREEN there is the voltage signal driving ground NMOS gate, in RED the voltage signal driving ASIC NMOS gate and in LIGHT BLUE is shown the current in

Figure 4.2: *Signal waveforms of simulated SiPM voltage modulation circuit: in BLUE the SiPM equivalent cell voltage bias switching from 29 V to 40 V; in LIGHT BLUE the bias current current charging and discharging the equivalent cell; in GREEN the voltage signal driving NMOS ground gate; in RED the voltage signal driving NMOS ASIC gate.*

the ASIC modeling resistor. In particular:

- Both NMOS are devices "2SK2009" from Toshiba, with a DC maximum current of 200 mA and gate capacitance of 70 pF [Figure 4.3].

- Ground channel NMOS is "2SK2009", ASIC channel NMOS is the component "2SK1828" from Toshiba, with a DC maximum current of 50 mA and gate capacitance of 5.5 pF [Figure 4.4].

- Ground channel NMOS is "DMC2400UV, COMPLEMENTARY PAIR ENHANCEMENT MODE MOSFET" by Diodes Incorporated, with a DC maximum current of 800 mA and gate capacitance of 37 pF, ASIC channel NMOS is "2SK1828" [Figure 4.5].

Considering the first transition (ASIC channel activation, ground channel deactivation), that is crucial because signal current is also flowing in the ASIC channel, we can draw two conclusions from this results:

- Even if we choose a small NMOS for the ASIC channel, some spurious current due to the injection still flows in the channel.

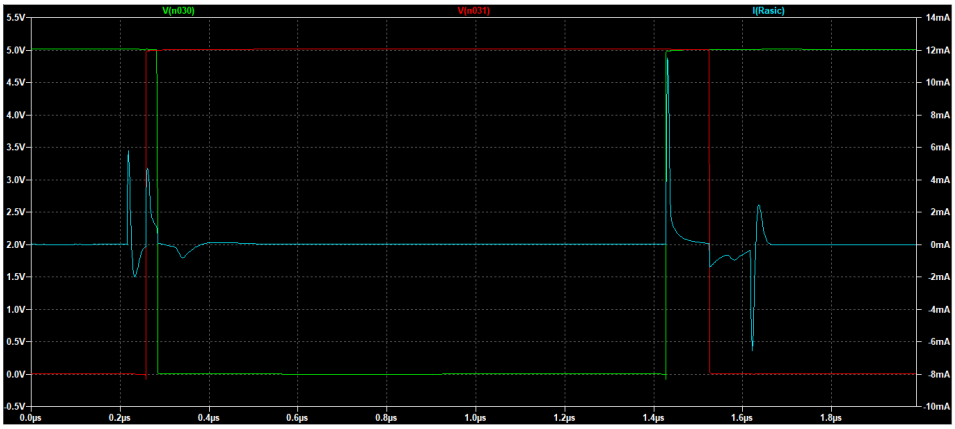

Figure 4.3: *Result of the simulation where both NMOS are "2SK2009" device.*

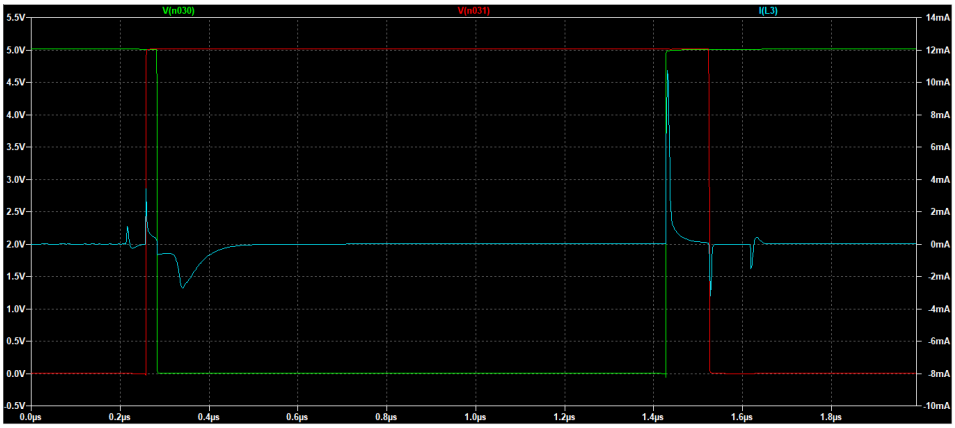

Figure 4.4: *Result of the simulation where ground NMOS is "2SK2009" device and ASIC NMOS is "2SK1828" device.*

- Better results are obtained with a ground channel NMOS with small gate capacitance dimension. However this Mosfet has to support the bias current coming from the SiPM. Hence there is a trade off between a Power Mosfet capable of high current but with a big gate capacitance and a more performing Mosfet carrying lower current.

In the end, for the ground channel NMOS the best choice we can find on the market is the "COMPLEMENTARY PAIR" (like DMC2400UV or DMC21D1UDA from Toshiba, that have similar characteristic) that is capable of high current but presents a gate capacitance value lower than the usual Power Mosfet. Farther, also for the ASIC channel NMOS we discover

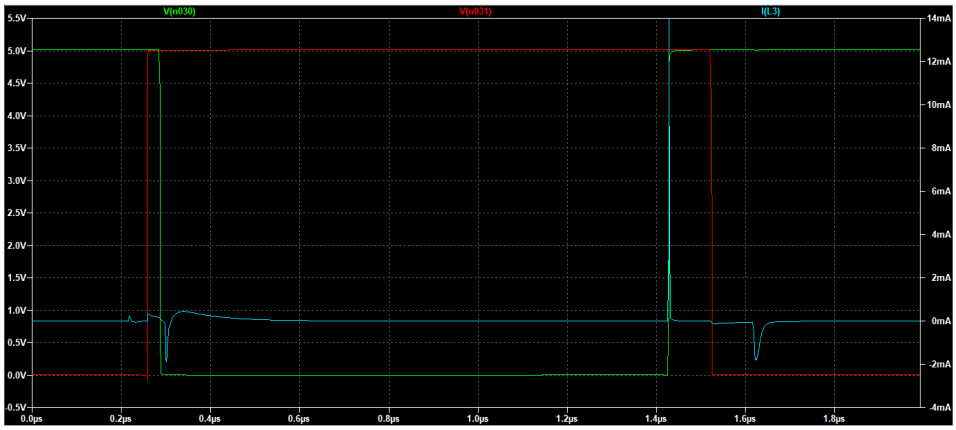

Figure 4.5: *Result of the simulation where ground NMOS is "DMC2400UV" device and ASIC NMOS is "2SK1828" device.*

a better solution in a complementary pair Mosfet with low current and very low gate capacitance value, like "ALD1115, COMPLEMENTARY N-CHANNEL AND P-CHANNEL MOSFET" by ADVANCED LINEAR DEVICES, with DC drain current of 5 mA and gate capacitance of 3 pF.

4.1.2 Simulation 2: delays setting

Initial specifications

The purpose of the test is to find the optimal temporal width of the superposition region where the two NMOS are both switched on. As we have already mentioned, overlap is necessary for two reasons:

- The ground channel must be active as much as possible to discharge the bias current to ground, but the ASIC channel must be immediately ready to receive the signal current as soon as the ground NMOS turns off. To avoid wasting further nanoseconds waiting for the ASIC NMOS to switching on, we can anticipate the turn on while the other channel is active yet. The bias current tail, that may not be extinguished at the moment of the ASIC NMOS switching on, does not represent an issue, as we have chosen two very different NMOS. The biggest one (ground NMOS) has a lower channel resis-

tance in respect to the smaller NMOS (NMOS ASIC). So when both are turned on, the current will flow mainly in the ground channel.

- Thanks to overlap, the injection currents of ASIC NMOS turn on are partially deviated towards ground, because the resistance of the other channel is lower.

The trade off in this configuration lies in the fact that, as long as the ground channel remains active, the fluorescence signal superimposed on the bias current will also flow into it. However, when the ASIC channel is activated and the ground one is deactivated, all the current will flow into the ASIC, both the signal one and the residual of the exponential tail of the bias current. Thus, we have to find the right moment to turn the MOSFETs on and off to have less bias current and more signal in the ASIC channel.

In this simulations we choose the device "DMC21D1UDA" as ground channel NMOS and "2SK1828" as ASIC channel NMOS. ASIC NMOS turn on is fixed 20 ns after the SiPM bias voltage switching, while ground NMOS turn off is tested at different delays. In figure 4.6 there are represented voltage signals driving MOSFET gates: in RED there is ASIC NMOS gate voltage, in GREEN there is ground NMOS gate voltage sweep at 7 different delays. In next simulations we will evaluate how the current in the ASIC channel changes as the ground NMOS shutdown delay varies.

Results and consideration

Next figures are the result of three different simulations. In the first two, ASIC NMOS turn on is fixed while ground NMOS turn off is tested at several delays. Instead, the last simulation is a demonstration that delaying ASIC NMOS turn on (while ground NMOS is fixed) does not change the current absorbed by the ASIC channel, confirming that to optimize the performance it is necessary to act on the delay of the ground NMOS. In particular:

- Current in ASIC modeling resistor is shown. ASIC NMOS turn

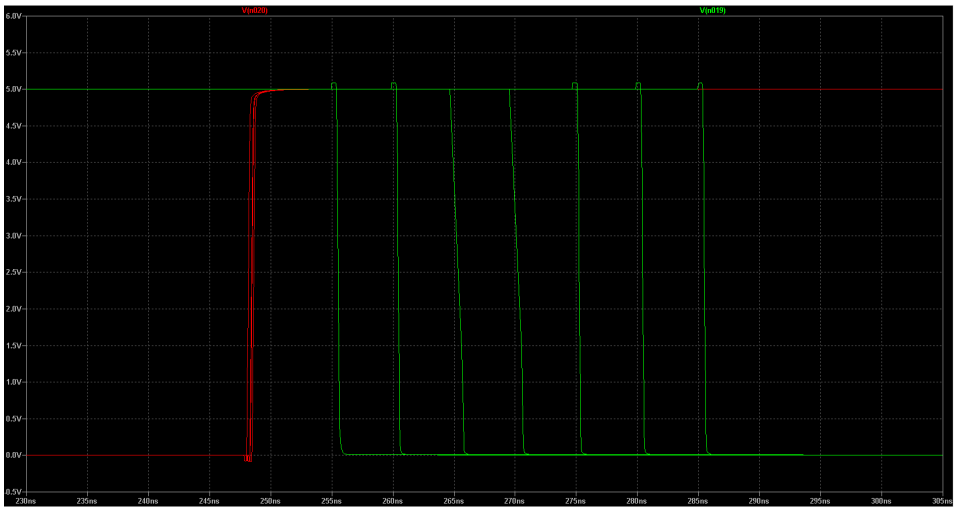

Figure 4.6: *NMOS gates sweep: RED signal fixed, GREEN signal delayed from 10 ns to 40 ns with 5 ns steps.*

on is fixed at 15 ns after the SiPM voltage bias switching. Ground NMOS turns off with steps from 0 ns (compared to the ASIC NMOS switching on) to 50 ns. We can see a current decreasing on the second peak as delay increases (from YELLOW, smallest delay, to DARK GREEN, biggest delay) [Figure 4.7].

- Current in ASIC modeling resistor is shown. ASIC NMOS turn on is fixed at 20 ns after the SiPM voltage bias switching. Ground NMOS turns off with steps from 5 ns (compared to the ASIC NMOS switching on) to 45 ns. We can see again a current decreasing on the second peak as delay increases (from RED, smallest delay, to OCHER, biggest delay)[Figure 4.8]

- Current in ASIC modeling resistor is shown. Ground NMOS turn off is fixed at 50 ns after the SiPM voltage bias switching. ASIC NMOS turns on with steps from 15 ns (compared to the SiPM voltage bias switching) to 35 ns. We can see main current peak shift as delay increases, but no increase or decrease (from RED, smallest delay, to DARK GREEN, biggest delay) [Figure 4.9].

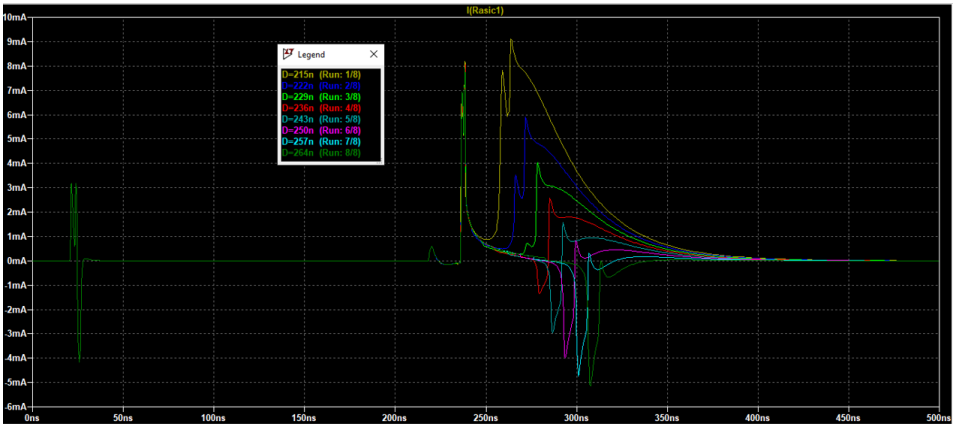

Figure 4.7: *Simulation result where in different colors the ASIC current is shown by switching off the ground NMOS with sweep from 0 ns (compared to the ASIC NMOS switching on) to 50 ns.*

Figure 4.8: *Simulation result where in different colors the ASIC current is shown by switching off the ground NMOS with sweep from 5 ns (compared to the ASIC NMOS switching on) to 45 ns.*

In the first two figures (4.7 and 4.8) it can be visible that the current peak around 240 ns (on the time scale of the figures, abscissa axis) does not change during the sweep, while the second one (larger, between 270 ns and 300 ns) is moving and reducing every time the delay increases. The first peak in fact is due to the current injection during the switching on of ASIC channel NMOS and it is inevitable: the only way to reduce it is to use a NMOS with a very small gate capacitance (less injection) and at the same time also a ground NMOS with lower channel resistance so that current

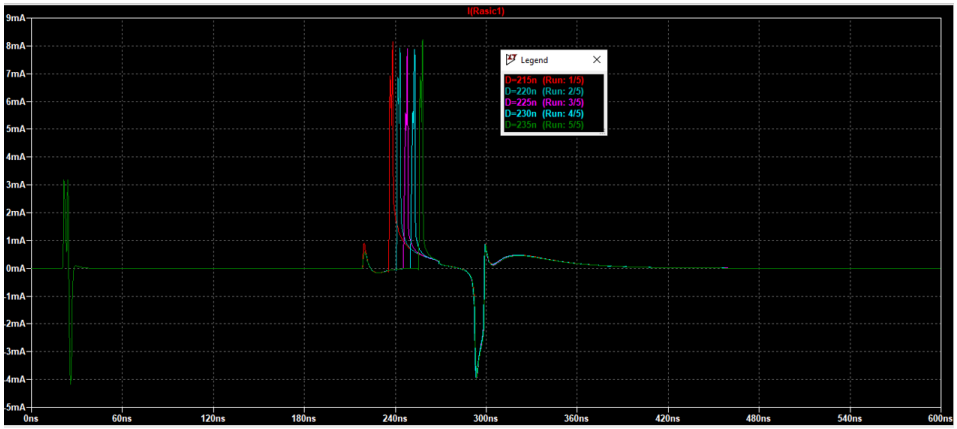

Figure 4.9: *Simulation result where in different colors the ASIC current is shown by switching off the ASIC NMOS with sweep from 15 ns (compared to the SiPM voltage bias switching) to 35 ns. Ground NMOS turn on is fixed to 50 ns after SiPM voltage bias switching.*

will flow partially into it while it is still active. The second peak is the residual current of the SiPM voltage bias switching, that flows in the ASIC channel after the ground NMOS switched off. Delaying ground channel deactivation the peak decreases because, as we said before, when both channel are active current still flows in the channel with less resistance.

From these results we can draw two conclusions:

- Delaying the switching on of the ASIC NMOS does not involve benefits on the current accumulated in the ASIC channel.
- Delaying the switching off of the ground NMOS reduces the current in the ASIC channel but leads to signal lost, thus also this current flows in the ground channel till it is active.

Considering that Pyrene has a lifetime of 200 ns, a good compromise is to choose a NMOS ground channel turn off delay between 40 ns and 60 ns in respect to SiPM voltage bias switching and a NMOS ASIC channel turn on in the middle, i.e. 30 ns after the SIPM turn on and 20 ns / 30 ns before the ground NMOS turn off.

In this evaluation it is also important to check signal linearity. In next simulations, amplitude current variations in ASIC modeling resistor

are represented as the signal current coming from the SiPM (modeled as a exponential pulse generator place inside the equivalent electric cell) increases. ASIC channel NMOS turn on is fixed at 35 ns after the SiPM voltage bias switching, while the ground channel NMOS turn off is set to 55 ns after the SiPM voltage bias switching (i.e 20 ns after ASIC NMOS turn on). Exponential signal is changed from 0 μA (BLUE in figures) to 200 μA (OCHER in figures). Figures 4.10, 4.11 and 4.12 are the simulation results.

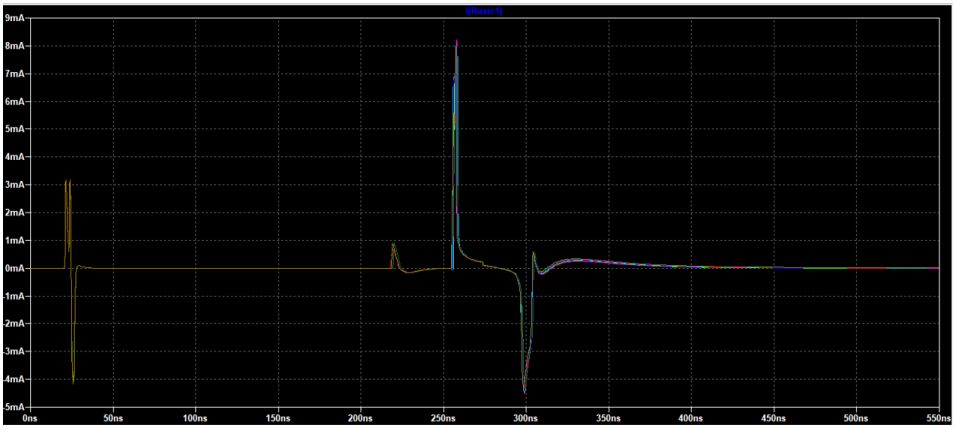

Figure 4.10: *Simulation result where in different colors the ASIC current is shown by changing current signal value.*

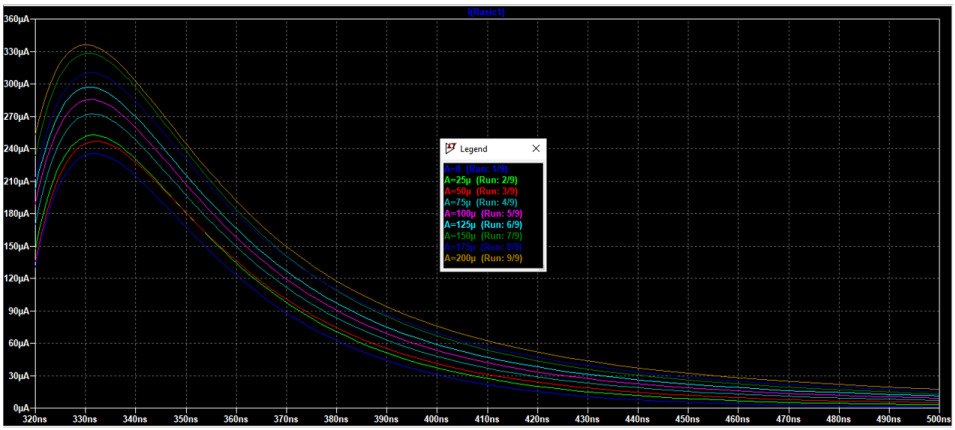

Figure 4.11: *A detail of the picture 4.10.*

The last figure (4.12) is a graph obtained with a function in Matlab

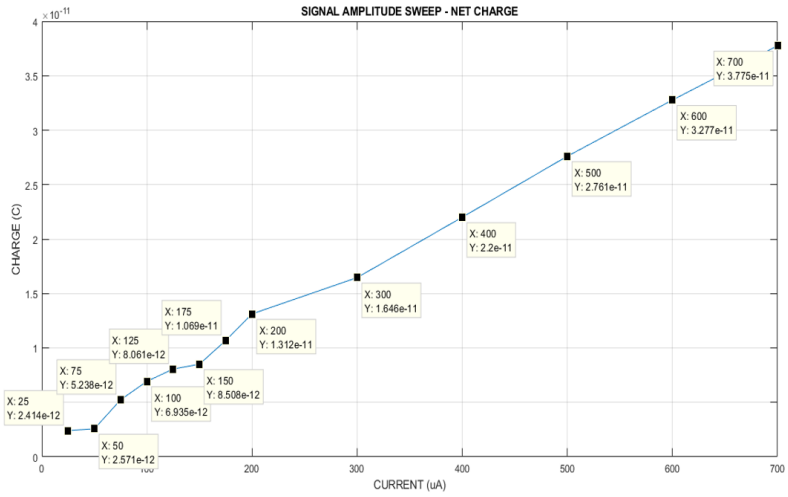

Figure 4.12: *Graph of net charge vs signal current.*

in which the current signal waveform file from LTSpice is acquired and then data current are transformed in data charge by an integral over the all time period saved in the file. In this way we get an approximation of the integrated current by the ASIC. The NET CHARGE (i.e the charge only due to the signal) is elaborated by subtracting from the total charge (signal + bias) the charge due to the bias current (acquisition with no signal). The graph shows that as the signal increases, also the net charge increases demonstrating the linearity.

Obviously a simple subtraction cannot give a true result since we have not considered the statistical component that affects the real measurements, but we can use this data as starting point for the experimental phase.

4.1.3 Simulation 3: parasitism

Initial specifications

In this test we evaluate the effect of parasitism, specially inductance due to wires connecting the photodetector to the PCB. In figure 4.13 is shown a detail of the circuit 4.1: in the center of the image we can see the SiPM

equivalent cell and inside the exponential pulse generator modelling the signal. At the ends of the equivalent cell there are two inductors with as many resistances. The values of the inductors are calculated taking into account the possible dimensions of the wires connecting the SiPM. As highlighted in the box on the left of the circuit, it is estimated that for a 3 cm long and 1 mm thick wire there is an inductance of about 30 nH.

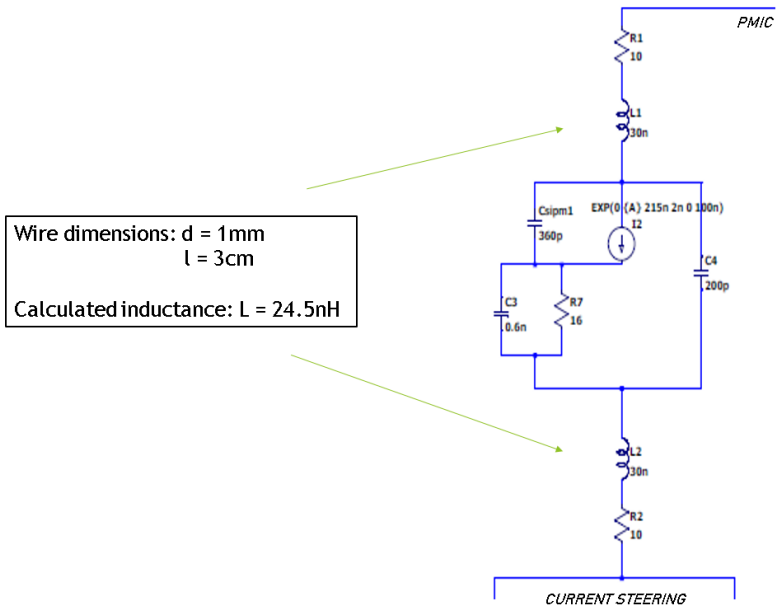

Figure 4.13: *Detail of the simulated circuit: SiPM equivalent cell, inductors and resistors are represented.*

Inductances introduce ripples on the SiPM over voltage step. To smooth out these oscillations it is necessary to place resistors: the choice of the resistance value is quite critical because a resistance that is too low may not attenuate the ripples, but a value that is too high slows down the rising edge of the signal before reaching steady-state. Therefore we use the simulations to get a basic idea of the optimal resistances required to balance the inductances.

Since we do not know for sure how much the real inductance value introduced by the wire is, we run some simulations by changing the values of the inductors starting from 1 nH (about 1 cm of wire) up to

100 nH (about 10 cm of wire) and consequently we look for an optimal value for resistances. The devices used for the current steering are again "DMC21D1UDA" as ground channel NMOS and "2SK1828" as ASIC channel NMOS. ASIC NMOS turn on is fixed 30ns after the SiPM bias voltage switching, while ground NMOS turn off is fixed 60 ns after the SiPM bias voltage switching (i.e. 30ns after ASIC NMOS turn on).

Results and consideration

Next four figures are the result of two different simulations. In the first two, resistances are fixed at 10 Ω while inductances grow from 1 nH to 100 nH with 10 nH steps. Instead in the other two simulations, inductances are fixed at 100 nH (worst case) and resistances vary from 5 Ω to 30 Ω. Here a brief description of the images:

- Inductance effect on the SiPM equivalent cell over voltage. Resistors are fixed at 10 Ω, inductors vary from 1 nH to 100 nH with 10 nH steps. It is visible a growing overshoot as the inductance value increases (from BLUE, smallest inductance, to BORDEAUX, biggest inductance) [Figure 4.14].

- Inductance effect on the current of ASIC modeling resistor. Resistors are fixed at 10 Ω, inductors vary from 1 nH to 100 nH with 10 nH steps. No increase in current is evident [Figure 4.15].

- Resistance effect on the SiPM equivalent cell over voltage. Inductors are fixed at 100 nH, resistors vary from 5 Ω to 30 Ω. It is visible a growing overshoot as the resistance value decreases (from BLUE, smallest resistance, to VIOLET , biggest resistance)[Figure 4.16].

- Resistance effect on the SiPM equivalent cell over voltage. Inductors are fixed at 100 nH, resistors vary from 5 Ω to 30 Ω It is visible a current increase as the resistance value increases (from RED, smallest resistance, to BORDEAUX , biggest resistance). In GREEN, resistance value is too small and does not affect inductance: the current

signal that is seen is due to a strong overshoot on the voltage. [Figure 4.17].

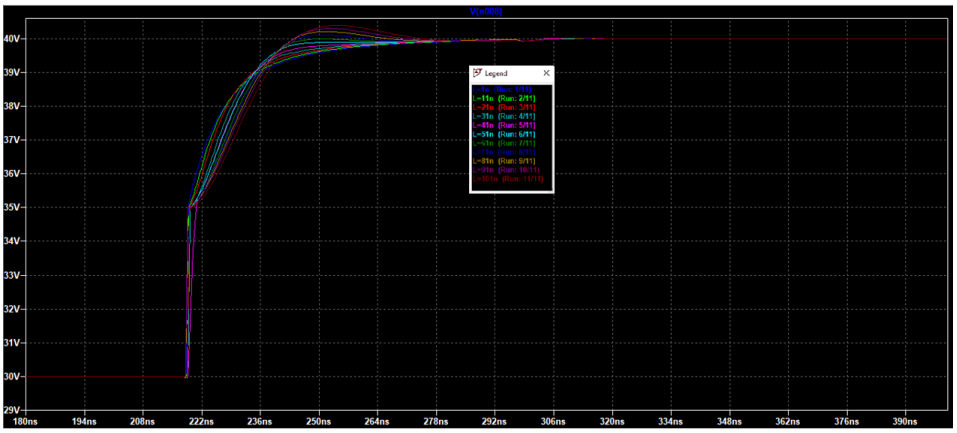

Figure 4.14: *Simulation result where in different colors the SiPM voltage is shown by changing inductance value.*

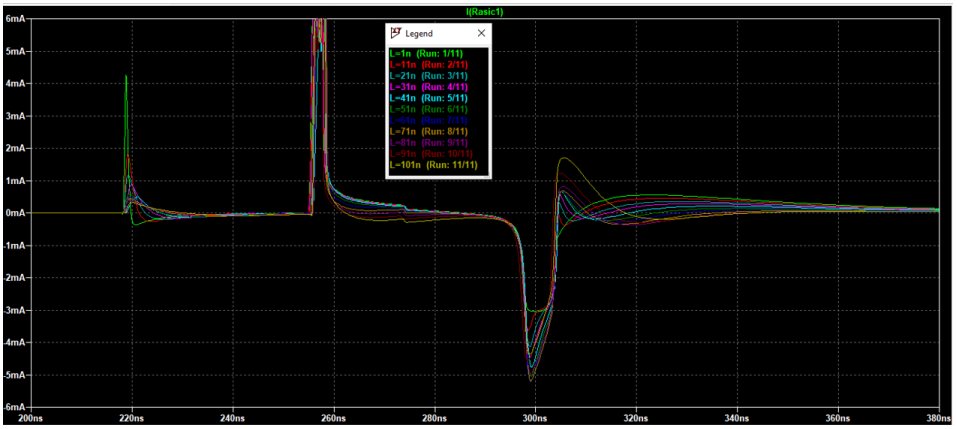

Figure 4.15: *Simulation result where in different colors the ASIC current is shown by changing inductance value.*

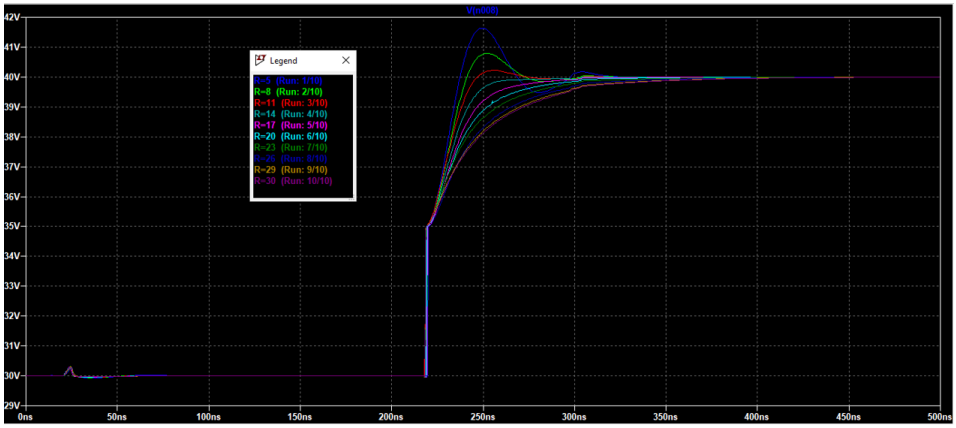

Figure 4.16: *Simulation result where in different colors the SiPM voltage is shown by changing resistance value.*

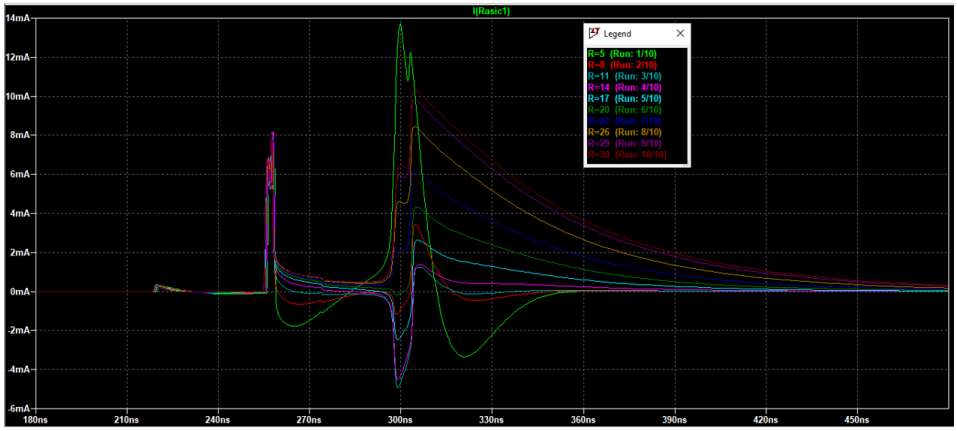

Figure 4.17: *Simulation result where in different colors the ASIC current is shown by changing resistance value.*

From these results we can draw two conclusions:

- Resistance is needed to mitigate the inductance ringing.

- An oversizing of the resistance causes a spurious current increase in the ASIC channel: since the over voltage signal has a slower rising edge, consequently the bias current has a slower exponential drop. When the ground channel is deactivated, the current tail diverted towards the ASIC channel is greater.

4.1.4 Final consideration on SiPM voltage bias modulation circuit based on simulated data

Simulations results indicate that the offset current that ends up in the ASIC channel due to switching can be reduced by delaying the shutdown of the ground channel. However, the signal current is also lost in this way. Thus, the major trade off lies in understanding whether it is convenient to acquire more spurious current but in the meantime also more signal or if it is better to minimize the offset and also lose a good part of the signal. Surely the first step in the experimental phase will be to evaluate the variability of the offset in order to understand which choice is the optimal one. For now it can be concluded that, assuming a more or less constant and stable offset, the best choice is an intermediate delay that guarantees the acquisition of at least 70 % of the signal but reduces the spurious current acquired to a few milliAmperes.

4.1.5 Simulation 4: LED pulsing circuit - parasitism

Initial specifications

In figure 4.18 , LED pulsing simulated circuit is shown. As for the simulated SiPM circuit, it was not possible to reproduce the model of all the components as the specifics for the simulation are not available from the manufacturer. Delay and PWM functions are modelled using a voltage pulse generator, with settings decided by the user, and a logic gate XOR. Then there is a CR to pull up the signal to exploit hysteresis of the PMIC and finally, after one other CR, we can see a diode between two inductors and two resistors.

Again, inductances simulate wires that connect the LED to the PCB and consequently resistors are inserted to mitigate effects on the signal. However, resistances also decrease the current flowing into the LED. Referring to figure 4.19 on right, a current of 200 mA is required to reach the maximum power: if we set the PMIC between the maximum supply (0 and 12 V), due to the resistances the voltage drop on the LED and the current

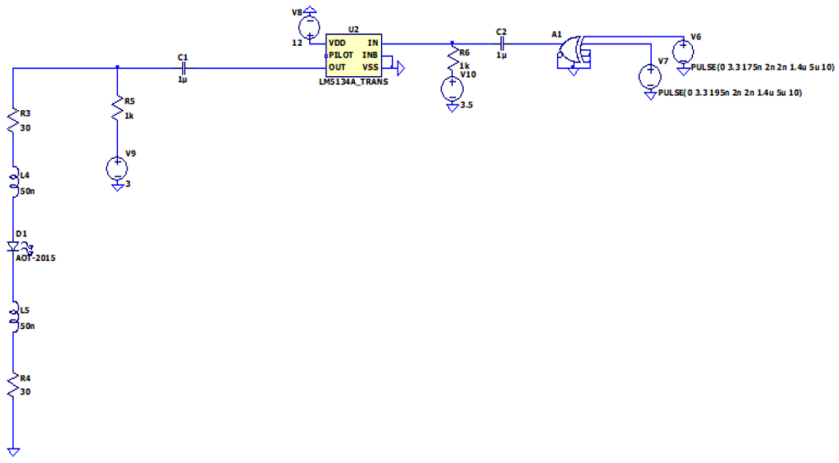

Figure 4.18: *LED simulated circuit.*

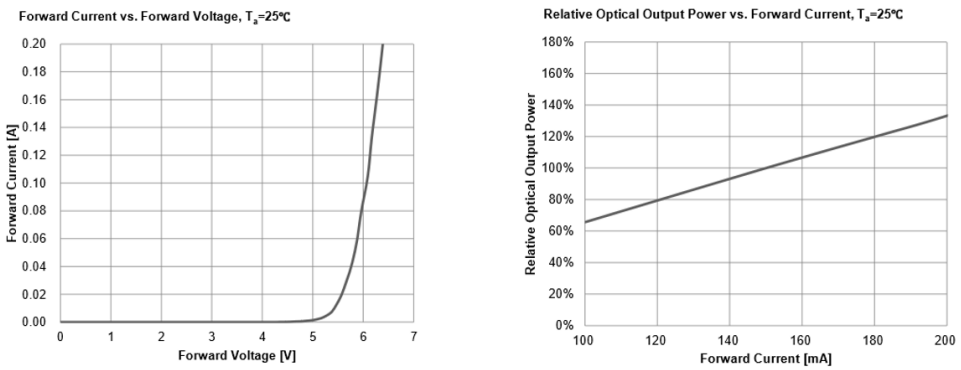

Figure 4.19: *LED forward current (left) and Output Power (right).*

will certainly be lower, but sufficient to achieve 200 mA. The second CR is used to shift the low level of the signal at 3 V: in this way (referring to figure4.19 on left), the LED is still off but closer to the threshold voltage so that the voltage drop can catch higher values.

Next simulations evaluate the influence of the inductances and the resistance values suitable to mitigate their effects and at the same time to guarantee sufficient current to the LED.

Results and consideration

Two simulations were made. In the first one (figure 4.20) inductance is fixed at 50 nH (reasonable value considering a wire of maximum 5 cm length) and resistances vary from 5 Ω to 105 Ω with 10 Ω steps. It is clear that a big resistance value (from PINK, resistance of 35 Ω, to YELLOW, resistance of 105 Ω) provides a signal with almost rectangular shape, but reduces the current. In the second one (figure 4.21) resistance is fixed at 30 Ω and inductances vary from 10 nH to 100 nH with 10 nH steps. It is visible that low inductance (BLUE) provides a rectangular shape signal, while high value (PURPLE) gives distorted signal.

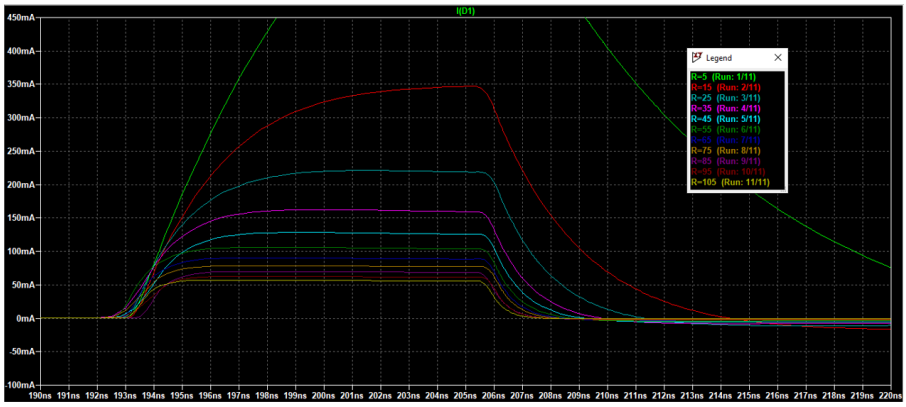

Figure 4.20: *Simulation result where in different colors the LED current is shown by changing inductance value.*

In conclusion, we can estimate that a resistance value between 20 Ω and 30 Ω can be a good compromise for an optimal operation of the circuit.

4.1.6 Experimental measurement

In this section we conduct some experiments with the real LINUS prototype in the order to demonstrate the system operation. First tests will evaluate the correct functioning of the SiPM modulator and the LED pulsing circuit. Subsequently, the real measurements on the offset current will be presented to understand the impact on the detection efficiency.

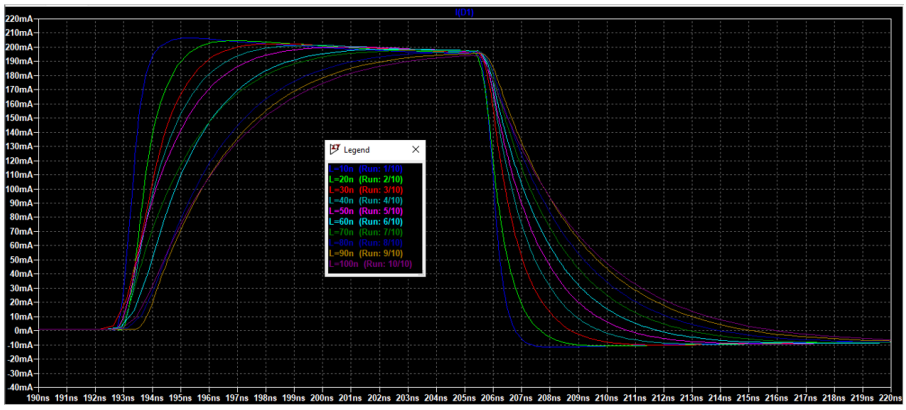

Figure 4.21: *Simulation result where in different colors the LED current is shown by changing inductance value.*

Signals Waveform

Aim of this first test is to evaluate the correct functioning of the system. A capacitance of 670 pF is used instead of the SiPM. As in simulation 1, we set the delay of the ASIC channel NMOS so that it turns on 30 ns after the voltage bias switching on the capacitance and the delay of the ground channel NMOS so that it turns off 60 ns after the voltage bias switching (i.e. 30 ns after the turn on of the ASIC channel NMOS). In this way we expect to obtain the same signals waveform show previously in figure 4.2. Ground NMOS is "2SK2009" device and ASIC NMOS is "2SK1828" device.

In this context we also check ASIC output signal and LED operation. LED delay and PWM are set to have a 60 ns of pulse width and its falling edge 20 ns before the rising edge of the SiPM voltage bias. Instead ASIC output signal is the integration result of the offset current due to the switching circuit. In figure 4.22 there are shown the main waveforms mentioned so far measured with an oscilloscope.

It can be noted that the rising and falling edges of the waveforms exactly respect the timings set by the firmware and by the programmable delays, confirming the correct design and operation of the driving circuits. Furthermore, we can see that the amplitude of the integration rectangle is about 1 V, i.e. the spurious current due to the switching of the bias on

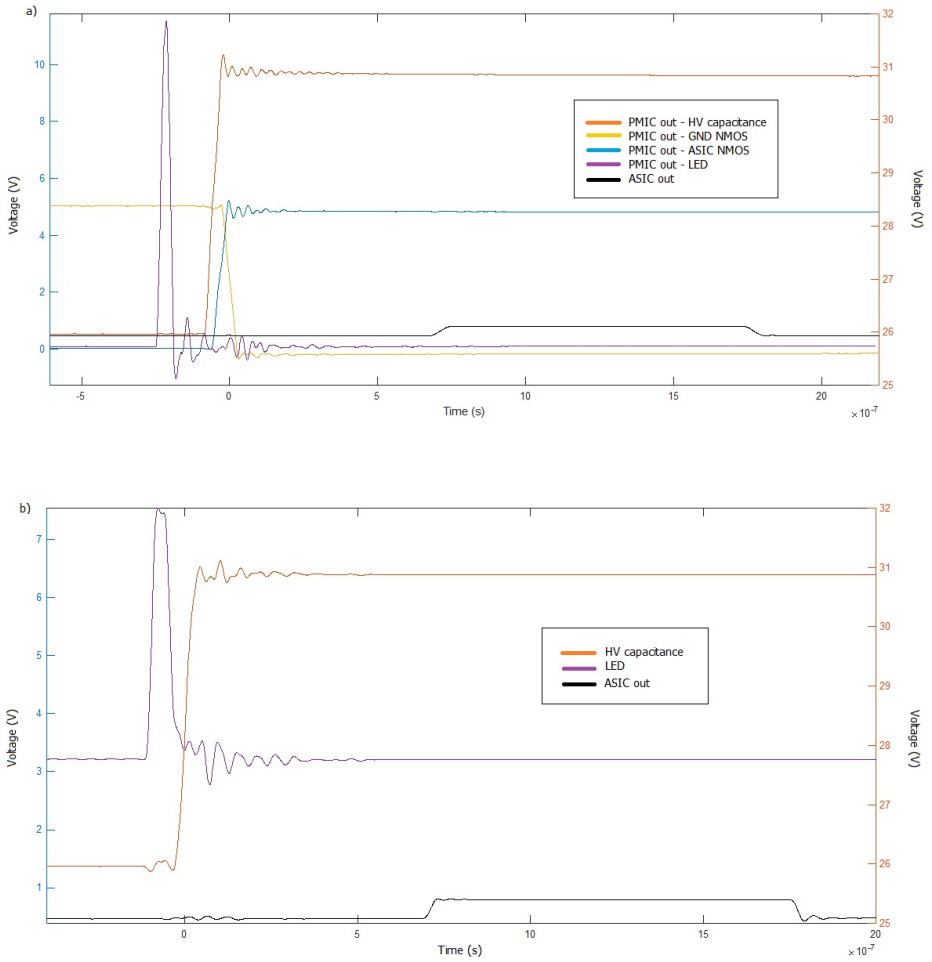

Figure 4.22: *Test result where all signals waveforms are shown: in figure a (top) there are all PMIC output and ASIC output, in figure b (bottom) a detail of LED voltage pulse and the bias switching on the capacitance of 670 pF.*

the capacitance and the injection of the two NMOS introduce an offset of about 500 mV.

Noise evaluation

This test is conducted is stationary condition, i.e. without SiPM voltage bias modulation and current steering. Aim of the measurement is to evaluate SiPM noise introduced by physical process and its effect on ASIC output. SiPM high voltage value is set to 31 V (4 V of over voltage) and

ASIC channel is kept always active: no spurious current flows in ASIC channel.

In figure 4.23 is represented ON Semiconductor SiPM 3 mm x 3 mm (BLUE cross) response when exposed to different light pulse generated by an optical laser: as the optical power increases, the ASIC voltage output level increases and the resolution is worse. Resolution is calculated starting from the output spectrum, considering the centroid and standard deviation of each spectral line.

SiPM ASIC output response (BLUE cross) can be compared to the ASIC response to an electrical pulser directly impulsing ASIC input (RED cross): we can notice that the first one fits perfectly the statistical noise function (BLUE dash line), while the second one follows the electronic noise function (RED dash line).

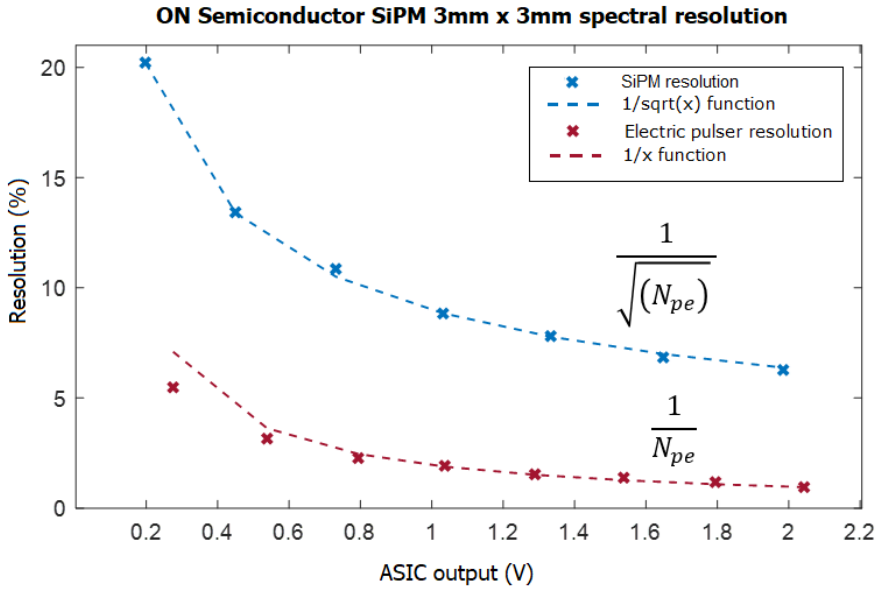

Figure 4.23: *ON Semiconductor SiPM spectral resolution (BLUE cross) is compared to electric pulser spectral resolution (RED cross), N_{pe} are the number of photo-electrons.*

Considering a rms noise of 8 mV at the ASIC output due to electronics (calculated from figure 4.23), we can asses an approximated value of the lowest fluorophore concentration that it is possible to detect. We can

write the rms output noise as equivalent photo-electrons at the input: a single photon current pulse produce an output voltage signal of 3.5 mV [20], thus 8 mV of noise are equivalent to 2.3 photo-electrons. From the Lambert-Beer low for low concentration, it is possible to extract the following equation:

$$c_{min} = \frac{N_{ph} \cdot E_{ph,\lambda_1}}{P_{LED} \cdot \Delta t \cdot \epsilon \cdot l \cdot Q \cdot EG \cdot PDE} \tag{4.1}$$

where N_{ph} is the number of photons absorbed, E_{ph,λ_1} is the energy of each photon at the wavelength of the fluorophore excitation, P_{LED} is the LED optical power, Δt is the LED pulse time width, ϵ is the extinction coefficient of the fluorophore, l the length of the light optical path, Q the quantum yield of the fluorophore, EG the geometric efficiency and PDE the SiPM photon detection efficiency.

Using the values listed in table 2.3 in chapter 2 for Pyrene, a LED optical power of 100 mW, a LED pulse duration of 10 ns, a PDE of 50 % of the SiPM, an optical light path l = 3 mm as the SiPM size, a geometric efficiency around 1/6 and a number of absorbed photons equal to the number of equivalent noise photons (to have SNR = 1), we can finally estimate a minimum concentration of 5 pM.

Offset evaluation

In this test, offset introduced only by MOSFET current injection is measured: no source light is used and no SiPM voltage bias switching occurs, thus SiPM is always turn on with high voltage fixed to 31 V (4V of over voltage). The SiPM used is ON Semiconductor 3 mm x 3 mm.

ASIC voltage output level is measured at different ground channel NMOS turn off delays. Six different delays are tested: from 30 ns (after ASIC channel activation) to 80 ns with 10 ns steps. In figure 4.24, centroid (left) and standard deviation (right) are shown with respect to the number of delays (1 corresponds to 30 ns delay, 2 corresponds to 40 ns delay and so on till 6 which corresponds to 80 ns delay). It is clear that as the delay increase by 10 ns, the offset increase linearly by 10mV, while the standard

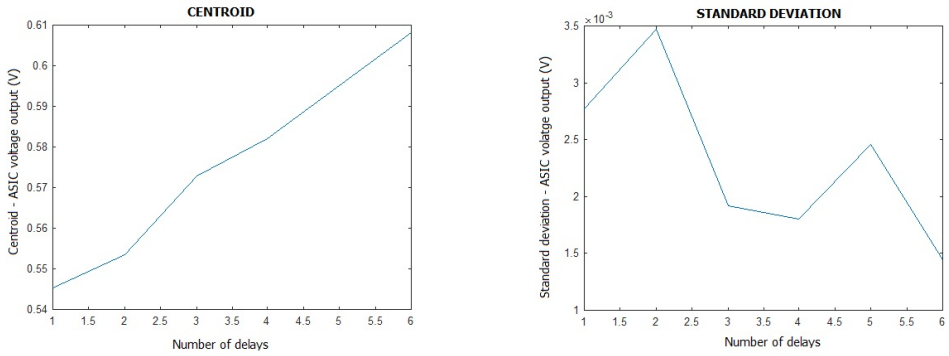

Figure 4.24: *Centroid and Standard Deviation at different delays.*

deviation seems to be almost constant for each delay around the value of 2.5 mV.

Choosing a delay value of 30 ns, the offset is about 550 mV with a standard deviation of 2.7 mV.

A second offset evaluation is performed adding the SiPM voltage bias switching from 26 V to 31 V. ASIC channel NMOS turns on 30 ns after the bias switching, while ground channel NMOS turns off 60 ns after the bias switching. In this condition the voltage offset measured at the ASIC output is around 1.2 V.

SiPM shielding effect evaluation

In this test two SiPM are tested at the same conditions to evaluate shielding effect of the bias switching and the ASIC correct functioning when exposed to laser light. An optical laser is used as light source and its pulse of 100 ns width is shifted in time with respect to SiPMs voltage bias switching. The current steering is active and synchronized, so that ASIC channel NMOS turns on 30 ns after the SiPM voltage bias switching and ground channel NMOS turns off 60 ns after the SiPM voltage bias switching.

Referring to figure 4.25: when the laser pulse shuts down before SiPM turning on, no signal current flows in the ASIC channel and at the ASIC output only spurious current is integrated. Instead, when the laser pulse

is shifted and starts to overlap SiPM bias switching, some current due to SiPM light response flows in to the ASIC, thus at the output we can see an higher signal as the result of integration.

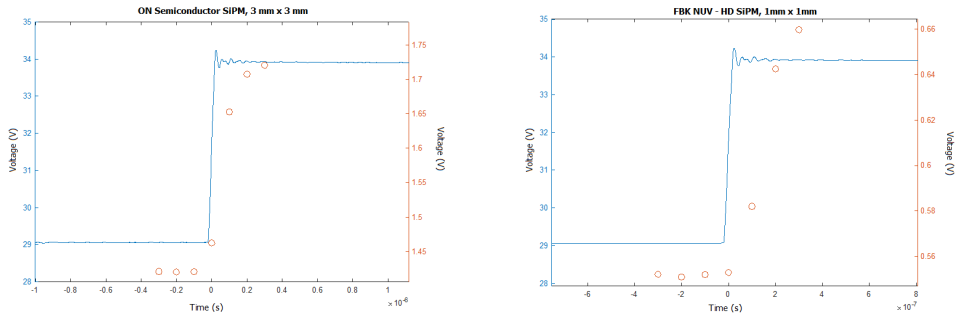

Figure 4.25: *ON Semiconductor SiPM (left) and FBK NUV-HD SiPM (right) response to laser light: in BLUE SiPM voltage bias switching, in RED circles ASIC voltage output levels.*

In figure 4.25, on the left there is the response of ON Semiconductor SiPM 3 mm x 3 mm, while on the right is reported the response of FBK NUV-HD SiPM 1 mm x 1 mm. The time reference is the SiPM voltage bias switching, set to 0 ns (BLUE line in figure), while in RED circles there are represented ASIC output level every 100 ns pulse shift. Referring to the ON Semiconductor SiPM (on left): first three RED circles before 0 ns are aligned. These represent the ASIC voltage output level when no signal current is integrated. In this case, the voltage output value is about 1.4 V, meaning that there is an offset of 1.4 V due to spurious current coming from SiPM voltage bias switching and NMOS injection currents.

The other RED circles, after 0 ns, are at higher voltages because at every pulse shift more signal current is integrated. We can conclude that the shielding effect performed by the SiPM itself on the source light is working.

Looking at FBK NUV-HD SiPM (on right), we can draw same conclusions: before the SiPM voltage bias switching, the ASIC output is almost constant, while after SiPM turn on, ASIC voltage output grows as the laser light impinging on the SiPM increases.

However it can be notice that in this case the ASIC voltage output due only to spurious current is about 550 mV, i.e. 1 V less then the other SiPM. This result comes from the use of a smaller SiPM that needs a lower bias current to turn on. The offset value is almost the same obtained in the offset evaluation test without bias modulation: this means that for better results and minimal offset it is convenient to use smaller SiPMs.

Chapter 5

Conclusion and Future Developments

In this chapter will be presented a wrap-up of the developed system, concluding with the challenges and future perspectives for the project.

5.1 Conclusions

With this thesis work we have demonstrated the design and operation of a driving circuit for the SiPM bias voltage with the aim of avoiding the classic filters used in spectrofluorometers. The use of the delay lines has allowed the perfect synchronization between the signals of the modulator itself and with the LED pulses, thus implementing the desired shielding effect. LED pulses of 10 ns time width are generated and shifted so that their falling edge can be positioned exactly 20 ns or less before the SiPM voltage bias rising edge. The current steering performed by the two NMOS can be changed in time only acting on the programmable delay lines, thus it is possible to turn on and off MOSFET with 1 ns delay with respect to each other. Thanks to the simulations carried out in detail, we were able to evaluate all the possible problems that we could have encountered in the real implementation, allowing the realization of a functioning system.

Experimental measurements have highlighted that the main limits for

a single photon detection efficiency are due to the residual readout noise in the setup around 8 mV rms and to the offset injected by the MOSFETs in the current steering circuit. Offset causes voltage output values between 500 mV and 1.4 V depending on SiPM size, but the standard deviation can be consider constant around 3 mV for all values. SiPM with small dimensions are preferable because they need less current to turn on, therefore there is less offset and more dynamics available at the output.

The ambitious goal of being able to detect a quantity of fluorescence with a sensitivity equal to or greater than the instruments already in use has not been demonstrated yet, but the prospects for success are positive for the next experiments. Surely the prototype is momentarily bound to the choice of the fluorophore and other aspects that do not make it usable on a large scale or for different purposes, however the idea that we have introduced with the modulation of the photodetector and the synchronization of the signals is a good starting point for future developments.

5.2 Future developments

The next step of the project will be the quantification of the detection limit with the current prototype. Tests will be conducted with the analyte molecule to measure the minimum detectable concentration. Subsequently, optimization operations will be made to try to improve performances.

In particular, action will be taken on two fronts: the improvement of the electronic design with an accurate evaluation of the noise and a more careful choice of the SiPM, which could help achieve single photon detection.

From the electronic point of view it is important to act first on the power management in order to make the module autonomous and transportable. Then it is also necessary to reduce the spurious current, using more performing discrete devices. As for the SiPM, it has been shown that a small area photodetector generates a negligible bias current, but

a more in-depth study will be carried out to define its impact and to be able to detect even single photons emitted by the fluorophore.

Finally, the last step will be to conduct dynamic measurements, with fluorophore and solvent flowing through a tube, set in motion by a peristaltic pump.

Bibliography

[1] Myer Kutz and Myer Kutz. *Handbook of measurement in science and engineering*. Wiley Online Library, 2013 (cit. on p. 2).

[2] M.E. Díaz-García and R. Badía-Laíño. "FLUORESCENCE | Overview". In: *Encyclopedia of Analytical Science (Second Edition)*. Ed. by Paul Worsfold, Alan Townshend, and Colin Poole. Second Edition. Oxford: Elsevier, 2005, pp. 97–106. ISBN: 978-0-12-369397-6. DOI: https://doi.org/10.1016/B0-12-369397-7/00161-8. URL: https://www.sciencedirect.com/science/article/pii/B0123693977001618 (cit. on p. 2).

[3] Joseph Lakowicz. *Principles of Fluorescence Spectroscopy*. Vol. 1. Jan. 2006. ISBN: 978-0-387-31278-1. DOI: 10.1007/978-0-387-46312-4 (cit. on pp. 2, 30, 33–46).

[4] AZoM. *Applications of Advanced Fluorescence Spectroscopy*. URL: https://www.azom.com/article.aspx?ArticleID=13958 (visited on Jan. 2021) (cit. on p. 3).

[5] *Unit-5 Fluorimetry and Phosphorimetry*. URL: http://egyankosh.ac.in//handle/123456789/43279 (visited on Jan. 2021) (cit. on p. 3).

[6] Hulie Zeng. "Laser-Induced Fluorescence". In: *Encyclopedia of Microfluidics and Nanofluidics*. Ed. by Dongqing Li. Boston, MA: Springer US, 2013, pp. 1–7. ISBN: 978-3-642-27758-0. DOI: 10.1007/978-3-642-27758-0_793-6. URL: https://doi.org/10.1007/978-3-642-27758-0_793-6 (cit. on p. 5).

[7] Han Yen Tan, Tuck Wah Ng, and Oi Wah Liew. “Filterless fluorometry with enhanced sensitivity”. In: *Journal of fluorescence* 19.2 (2009), pp. 375–379 (cit. on p. 7).

[8] P Dorosz et al. “Silicon photomultipliers applied to the fluorescence detection of biomarkers”. In: *Nuclear Instruments and Methods in Physics Research Section A: Accelerators, Spectrometers, Detectors and Associated Equipment* 936 (2019), pp. 70–72 (cit. on p. 7).

[9] Maria Francesca Santangelo et al. “Si photomultipliers for bio-sensing applications”. In: *IEEE Journal of Selected Topics in Quantum Electronics* 22.3 (2015), pp. 335–341 (cit. on p. 7).

[10] Hongtao Wang et al. “A portable time-domain LED fluorimeter for nanosecond fluorescence lifetime measurements”. In: *Review of Scientific Instruments* 85.5 (2014), p. 055003 (cit. on p. 8).

[11] Brian Herman. *Basic Concepts in Fluorescence*. URL: https://www.olympus-lifescience.com/ (visited on Jan. 2021) (cit. on pp. 9–12, 14–16, 18, 19, 21–23, 25, 27, 30, 31, 33).

[12] Gursharan Bains, Arti B Patel, and Vasanthy Narayanaswami. “Pyrene: a probe to study protein conformation and conformational changes”. In: *Molecules* 16.9 (2011), pp. 7909–7935 (cit. on p. 47).

[13] Baagi T Mmereki and DJ Donaldson. “Laser induced fluorescence of pyrene at an organic coated air–water interface”. In: *Physical Chemistry Chemical Physics* 4.17 (2002), pp. 4186–4191 (cit. on pp. 48, 50).

[14] Gargi Ray, Indranil Chakraborty, and Satya Moulik. “Pyrene absorption can be a convenient method for probing critical micellar concentration (cmc) and indexing micellar polarity”. In: *Journal of colloid and interface science* 294 (Mar. 2006), pp. 248–54. DOI: 10.1016/j.jcis.2005.07.006 (cit. on pp. 48, 49).

[15] Frederick P Schwarz and Stanley P Wasik. “Fluorescence measurements of benzene, naphthalene, anthracene, pyrene, fluoranthene, and benzo [e] pyrene in water”. In: *Analytical chemistry* 48.3 (1976), pp. 524–528 (cit. on pp. 50, 51).

[16] AV Akindinov et al. “New results on MRS APDs”. In: *Nuclear Instruments and Methods in Physics Research Section A: Accelerators, Spectrometers, Detectors and Associated Equipment* 387.1-2 (1997), pp. 231–234 (cit. on p. 50).

[17] Davide Di Vita. “Development of a 3” LaBr3 SiPM-Based Detection Module for High Resolution Gamma Ray Spectroscopy and Imaging”. unpublished thesis. 2019 (cit. on pp. 52, 55, 57, 58, 61, 62, 66, 79–82).

[18] Alberto Gola et al. “NUV-sensitive silicon photomultiplier technologies developed at Fondazione Bruno Kessler”. In: *Sensors* 19.2 (2019), p. 308 (cit. on pp. 54, 61, 68, 70).

[19] Claudio Piemonte et al. “Performance of NUV-HD silicon photomultiplier technology”. In: *IEEE Transactions on Electron Devices* 63.3 (2016), pp. 1111–1116 (cit. on pp. 54, 68).

[20] Matteo Grandi. “Development of GAMMA: a 16-channels high dynamic range readout ASIC for SiPMs”. unpublished thesis. 2017 (cit. on pp. 66, 79, 126).

[21] *Single 7.6-A Peak Current Low-Side Gate Driver With a PILOT Output"*. LM5134AMF. Texas Instrument. 2015. URL: https://www.ti.com/product/LM5134 (cit. on p. 72).

[22] *8-Bit Programmable Timing Element*. DS1023. Maxim Integrated. 2005. URL: https://www.maximintegrated.com/en/products/analog/clock-generation-distribution/DS1023 (cit. on p. 77).

[23] *Single 7.6-A Peak Current Low-Side Gate Driver With a PILOT Output"*. LT3088. Linear Technolog. 2015. URL: https://www.analog.com/en/products/lt3088 (cit. on p. 86).

[24] THORLABS. *UV Fused Quartz Cuvettes*. URL: https://www.thorlabs.com/newgrouppage9.cfm?objectgroup_id=5943&gclid=EAIaIQobChMIhafi4JXa7wIVEnYYCh1A4giiEAAYASAAEgKMP_D_BwE (visited on Feb. 2021) (cit. on p. 86).

[25] Tsung-Ting Shih et al. "Development of chip-based photocatalyst assisted reduction device to couple high performance liquid chromatography and inductively coupled plasma-mass spectrometry for determination of inorganic selenium species". In: *Journal of Chromatography A* 1304 (Aug. 2013), pp. 101–108. DOI: 10.1016/j.chroma.2013.06.067 (cit. on p. 97).

[26] Qais M. Al-Bataineh et al. "A novel optical model of the experimental transmission spectra of nanocomposite PVC-PS hybrid thin films doped with silica nanoparticles". In: *Heliyon* 6.6 (2020), e04177. ISSN: 2405-8440. DOI: https://doi.org/10.1016/j.heliyon.2020.e04177. URL: https://www.sciencedirect.com/science/article/pii/S2405844020310215 (cit. on p. 97).

Ringraziamenti

Un ringraziamento speciale a Luca, Davide e Marco per l'aiuto pratico e indispensabile per portare a termine il progetto.

Ringrazio calorosamente anche la mia famiglia, i miei amici e tutto il team RadLab per il supporto morale.